

## Cooperative Control Mechanism for Platoon Formation of Connected and Autonomous Vehicles

---

Srinivas Peeta  
Jian Wang  
Yu Wang  
Chaojie Wang  
Anye Zhou



**CENTER FOR CONNECTED  
AND AUTOMATED  
TRANSPORTATION**

Report No. 25  
Project Start Date: 1/1/2018  
Project End Date: 04/14/2021

June 2022

# **Cooperative Control Mechanism for Platoon Formation of Connected and Autonomous Vehicles**

## **Anye Zhou**

Graduate Researcher  
Georgia Institute of Technology

## **Chaojie Wang**

Graduate Researcher  
Georgia Institute of Technology

## **Jian Wang**

Associate Professor  
Southeast University

## **Yu Wang**

Postdoctoral Fellow  
Georgia Institute of Technology

## **Srinivas Peeta**

Frederick R. Dickerson Chair & Professor  
Georgia Institute of Technology





## **ACKNOWLEDGEMENTS AND DISCLAIMER**

Funding for this research was provided by the Center for Connected and Automated Transportation under Grant No. 69A3551747105 of the U.S. Department of Transportation, Office of the Assistant Secretary for Research and Technology (OST-R), University Transportation Centers Program. The contents of this report reflect the views of the authors, who are responsible for the facts and the accuracy of the information presented herein. This document is disseminated under the sponsorship of the Department of Transportation, University Transportation Centers Program, in the interest of information exchange. The U.S. Government assumes no liability for the contents or use thereof.

Suggested APA Format Citation:

Zhou, A., Wang, C., Wang, J., Wang, Y., Peeta, S. (2022). Cooperative Control Mechanism for Platoon Formation of Connected and Autonomous Vehicles, CCAT Report #25, Center for Connected and Automated Transportation, Purdue University, West Lafayette, IN.

### **Contact Information**

Samuel Labi  
3000 Kent Ave, West Lafayette, IN  
Phone: 7654945926  
Email: [labi@purdue.edu](mailto:labi@purdue.edu)

Srinivas Peeta  
788 Atlantic Dr, Atlanta, GA  
Phone: 4048942243  
Email: [peeta@gatech.edu](mailto:peeta@gatech.edu)

**CCAT**  
University of Michigan Transportation  
Research Institute  
2901 Baxter Road  
Ann Arbor, MI 48152

[uumtri-ccat@umich.edu](mailto:uumtri-ccat@umich.edu)  
(734) 763-2498  
[www.ccat.umtri.umich.edu](http://www.ccat.umtri.umich.edu)





**Technical Report Documentation Page**

<b>1. Report No.</b> 25	<b>2. Government Accession No.</b>	<b>3. Recipient's Catalog No.</b>	
<b>4. Title and Subtitle</b> Cooperative Control Mechanism for Platoon Formation of Connected and Autonomous Vehicles		<b>5. Report Date</b> June 2022	
		<b>6. Performing Organization Code</b> N/A	
<b>7. Author(s)</b> Anye Zhou, Chaojie Wang, Jian Wang, Yu Wang, Srinivas Peeta		<b>8. Performing Organization Report No.</b> N/A	
<b>9. Performing Organization Name and Address</b> Center for Connected and Automated Transportation Purdue University, 550 Stadium Mall Drive, W. Lafayette, IN 47907; and University of Michigan Ann Arbor, 2901 Baxter Road, Ann Arbor, MI 48109		<b>10. Work Unit No.</b> N/A	
		<b>11. Contract or Grant No.</b> Contract No. 69A3551747105	
<b>12. Sponsoring Agency Name and Address</b> U.S. Department of Transportation Office of the Assistant Secretary for Research and Technology 1200 New Jersey Avenue, SE Washington, DC 20590		<b>13. Type of Report and Period Covered</b> Final Report, 1/1/2018 to 04/14/2021	
		<b>14. Sponsoring Agency Code</b> OST-R	
<b>15. Supplementary Notes</b> Conducted under the U.S. DOT Office of the Assistant Secretary for Research and Technology's (OST-R) University Transportation Centers (UTC) program.			
<b>16. Abstract</b> Connected and autonomous vehicles (CAVs) can potentially improve traffic safety and mobility significantly through platoon formation wherein vehicles follow each other closely. Such platoons also may reduce energy consumption of individual CAVs by reducing air drag. While control mechanisms have been previously proposed to control vehicles in a platoon, for example, through adaptive cruise control, they mainly focus on seeking a better situation for an individual vehicle by controlling its driving behavior. This study focused on CAV-based control mechanisms to holistically determine the acceleration/deceleration rate of each CAV in a platoon to maximize platoon performance. It designs several robust control mechanisms to coordinate the behaviors of CAVs in a platoon to ensure safe and efficient maneuver of CAV platoon by addressing several realistic challenges such as the unreliable vehicle-to-vehicle communication (i.e., packet loss) and uncertainty of the leading vehicle's future behavior. The impact of information delay and topology of information that is exchanged among vehicles on platoon dynamics are analyzed. The optimal time headway and platoon size to maximize fuel efficiency of the CAVs in the platoon are determined. Furthermore, this study developed control mechanisms for a platoon of connected and autonomous vehicles to coordinate the behavior of all the following vehicles in the platoon to improve safety, mobility, and energy consumption.			
<b>17. Key Words</b> Connected autonomous vehicles, Cooperative control, Platoon		<b>18. Distribution Statement</b> No restrictions.	
<b>19. Security Classif. (of this report)</b> Unclassified	<b>20. Security Classif. (of this page)</b> Unclassified	<b>21. No. of Pages</b> 110 pages	<b>22. Price</b> N/A

Form DOT F 1700.7 (8-72)

Reproduction of completed page authorized





## **Table of Contents**

<b>1. INTRODUCTION.....</b>	<b>2</b>
<b>2. COOPERATIVE ADAPTIVE CRUISE CONTROL FOR CONNECTED AUTONOMOUS VEHICLES BY FACTORING COMMUNICATION-RELATED CONSTRAINTS.....</b>	<b>4</b>
2.1 Introduction.....	4
2.2 IFT and degeneration scenarios.....	8
2.3 Formulation of optimization model for IFT.....	10
2.3.1 Speed oscillation energy of a degeneration scenario for an IFT and its linkage to string stability.....	12
2.3.2 Probabilities of degeneration scenarios and expected string stability for an IFT.....	13
2.4 Formulation of adaptive controller for degeneration scenarios of IFT.....	15
2.4.1 Control structure.....	16
2.4.2 Stability analysis and parameter determination.....	19
2.5 Algorithm to solve OPT-II.....	23
2.5.1 Activation status of “send” functionalities of the leading and last vehicles in the platoon...24	
2.5.2 Two- step algorithm for solving OPT-II.....	28
2.6 Numerical experiments.....	29
2.6.1 Experiment design and parameter setting.....	29
2.6.2 Performance of V2V communications, optimization result and computation efficiency.....30	
2.6.3 Control performance evaluation.....	32
<b>3. SMOOTH SWITCHING CONTROL BASED CACC CONSIDERING DYNAMIC INFORMATION FLOW TOPOLOGY.....</b>	<b>38</b>
3.1 Introduction.....	38
3.2 Formulation of platoon control.....	40
3.2.1 IFT degeneration and receiver status.....	41
3.2.2 Controller structure.....	42
3.2.3 Stability analysis.....	43
3.3 IFT optimization.....	46
3.3.1 Probability of IFT degeneration.....	46
3.3.2 Performance metric.....	47
3.4 Controller parameter optimization.....	49
3.5 State estimation and Kalman predictor.....	50
3.5.1 Kalman filter structure.....	50
3.5.2 Kalman predictor and CACC reconstruction.....	52
3.6 Numerical experiments.....	53
3.6.1 Experiment setup.....	53
3.6.2 Experiment results.....	54
<b>4. A REAL-TIME DEPLOYABLE MODEL PREDICTIVE CONTROL-BASED COOPERATIVE PLATOONING APPROACH FOR CONNECTED AND AUTONOMOUS VEHICLES.....</b>	<b>58</b>



<b>4.1 Introduction .....</b>	<b>58</b>
<b>4.2 MPC approaches for longitudinal control of CAV platoon.....</b>	<b>61</b>
4.2.1 An idealized MPC cooperative control strategy for a CAV platoon .....	61
4.2.2 DMPC approach framework .....	66
4.2.3 DMPC-FOA approach framework .....	68
<b>4.3 Solution algorithm for optimal control problem (4.5).....</b>	<b>70</b>
<b>4.4 Sensitivity analysis of the optimal control problem.....</b>	<b>77</b>
<b>4.5 Stability analysis of the idealized MPC strategy with no inequality constraints .....</b>	<b>81</b>
<b>4.6 Numerical experiments .....</b>	<b>85</b>
4.6.1 Computational time for solving optimal control problem (4.5).....	85
4.6.2 Sensitivity analysis of optimal control problem (4.5) .....	88
4.6.3 Control performance of the DMPC and DMPC-FOA approaches .....	91
4.6.4 Scenario where the DMPC approach fails to control the CAV platoon .....	95
4.6.5 Two other scenarios to test the control performances of DMPC-FOA approach.....	97
<b>5. FINDINGS AND CONCLUSIONS .....</b>	<b>100</b>
<b>6. RECOMMENDATIONS .....</b>	<b>102</b>
<b>7. SYNOPSIS OF PERFORMANCE INDICATORS .....</b>	<b>103</b>
<b>8. OUTPUTS, OUTCOMES, AND IMPACTS.....</b>	<b>103</b>
8.1 List of research outputs (publications, conference papers, and presentations).....	103
8.2 Outcomes .....	104
8.3 Impacts .....	104
8.4 Tech Transfer .....	104
<b>9. REFERENCES .....</b>	<b>106</b>
<b>10. APPENDIX .....</b>	<b>111</b>



**List of Figures**

Figure 2.1. (a) Conceptual flowchart of CACC-OIFT; (b) Operational deployment of CACC-OIFT..... 7

Figure 2.2. CAV platoon with a two-predecessor-following VIFT scheme. .... 9

Figure 2.3. Example of an IFT and its degeneration scenarios: (a) IFT with “send” functionalities of CAVs 1, 3 and 4 deactivated; (b) Degeneration scenario with CAV 2 failing to send message; (c) Degeneration scenario with CAV 0 failing to send message; (d) Degeneration scenario with both CAVs 0 and 2 failing to send messages. .... 9

Figure 2.4. Communication statuses of: (a) CACC1; (b) CACC2; (c) CACC3; (d) ACC. .... 10

Figure 2.5. Schematic of the adaptive PD controller. .... 16

Figure 2.6. Illustration of the deactivated or activated status of the “send” functionality of CAV 0. .... 26

Figure 2.7. Experiment results for V2V communications: (a) Communication success rates under different ambient traffic conditions; (b) Comparison of calibrated contention model and simulation results for  $k=20$ . .... 31

Figure 2.8. Spacing error under different controllers: (a) CACC-OIFT; (b) CACC-DIFT; (c) CACC-FIFT. .... 34

Figure 2.9. Standard deviation of: (a) spacing error; (b) speed tracking error; (c) vehicle speed..... 34

Figure 2.10. Performance of the platoon in IFT transition period: ..... 35

Figure 2.11. Spacing error profile of: (a) Scenario 1; (b) Scenario 2; (c) Scenario 3. .... 36

Figure 2.12. Acceleration profile of: (a) Scenario 1; (b) Scenario 2; (c) Scenario 3. .... 37

Figure 3.1. Conceptual flowchart of the CACC-SOIFT ..... 39

Figure 3.2. Receiver status and controller sets..... 41

Figure 3.3. Block diagram of control schematic ..... 42

Figure 3.4. Performance of the CACC-SOIFT ..... 56

Figure 3.5. Comparisons of different CACC cases..... 56

Figure 3.6. Comparisons of different headway selections in CACC-SOIFT..... 57

Figure 4.1. A CAV platoon stream. .... 62

Figure 4.2. The idealized MPC strategy: (a) Implementation framework, and (b) Computational procedure..... 64

Figure 4.3. The DMPC approach: (a) Implementation framework, and (b) Computational procedure..... 67

Figure 4.4. Computational procedure of the DMPC-FOA approach. .... 70



**List of Tables**

Table 2.1. Weighting coefficient settings. ....	16
Table 2.2. Network parameters. ....	30
Table 2.3. Values of $\omega K, i$ in the sensitivity analysis of controller cut-off frequency.....	30
Table 2.4. Network parameters. ....	32
Table 3.1. Indicator values for controller sets.....	42
Table 3.2. Scenarios of CACC reconstruction .....	52
Table 4.1. Input parameters for optimal control problem (4.5) .....	86

## 1. INTRODUCTION

The cooperative platoon control of connected and autonomous vehicles (CAV) leverages the emerging vehicle-to-vehicle (V2V), and vehicle-to-infrastructure (V2I) communications to enhance the control performance in mitigating the propagation of traffic oscillations, increasing the road throughput, and reducing fuel consumptions. During the cooperative platoon control, CAVs will share the kinematic information with neighboring vehicles using a certain information flow topology (IFT), to reach to a consensus where all CAVs in the platoon will operate together at a harmonized speed, and maintain desired safe spacings with the preceding vehicles. However, to implement the cooperative platoon control of CAV in the real world, there are critical challenges existing in both communication and computational related issues, and this project aims at tackling with these critical issues.

Specifically, in the communication side, when the traffic density is high, and substantial amount of communication links are working simultaneously, the communication burden will be significant, and the ongoing communication links can interfere with each other. Under this circumstance, communication failure is prone to happen. To alleviate the issue of communication failure, chapter 2 of this study investigates the control mechanism involving IFT optimization, and controller switching. In the proposed control mechanism, the IFT is optimized based on an objective function which is designed to achieve optimal trade-off between string stability (i.e., performance index of traffic oscillation dissipation) and information transmitted in the platoon. The controller switching is conducted after the IFT optimization, where the controller of each CAV will be selected based on the optimized IFT. The control mechanism is then evaluated using numerical experiments to showcase the effectiveness of improving string stability under the situation of significant communication burden during the occurrence of heavy traffic. Additionally, even though the control mechanism in chapter 2 can achieve desired performance of string stability, the characteristics of controller switching and the inevitable process noise during platoon control will generate choppy control command (i.e., vehicle acceleration), which significantly deteriorate the riding comfort of platoon control. Thereby, chapter 3 further incorporates the smooth switching mechanism to the control design in chapter 2. The proposed smooth switching mechanism includes three components: (i) IFT optimization factoring string stability and riding comfort; (ii) controller parameter optimization for smooth transition between controller; and (iii) Kalman predictor which suppresses the negative effects of noise, and predicts future vehicles states for conducting smoother control input. The numerical experiments demonstrate the effectiveness of the control mechanism in terms of preserving driving comfort and string stability in the situation of heavy communication burdens. Chapter 2 and chapter 3 are collaborative works with Siyuan Gong, Chang'an University, China.

The computational issue mainly arises from the optimization-based real-time cooperative platoon control. The model predictive controller (MPC) is one of the popular approaches in the optimization-based real-time cooperative platoon control. MPC optimizes the objective function of a series of optimal control problem with certain physical and safety constraints, to achieve desired platoon control performance. However, MPC requires an instantaneous computation of control command in each time step, which can be difficult given a complex nonlinear nonconvex optimization problem. This significantly hinders the deployment of MPC-based platoon control. To counteract the influence of computational barrier, chapter 4 introduces a real-time deployable MPC mechanism with first-order approximation (label as DMPC-FOA). The DMPC-FOA reserves certain amount of time before each sampling time instant to estimate the optimal control command, which provides a sufficient time for computation and enables the execution optimal control command at each sampling instant. Numerical



experiments illustrate the effectiveness of DMPC-FOA in terms of computational efficiency, and desired performance of asymptotical stability and string stability. The chapter 4 is a collaborative work with Jian Wang, Southeast University, China, Siyuan Gong, Chang'an University, China, and Lili Lu, Ningbo University, China.

## **2. COOPERATIVE ADAPTIVE CRUISE CONTROL FOR CONNECTED AUTONOMOUS VEHICLES BY FACTORING COMMUNICATION-RELATED CONSTRAINTS**

### **2.1 Introduction**

Traffic oscillation refers to “stop and go” traffic propagation (Li et al., 2010), which can cause uncomfortable driving experience, safety problems, additional energy consumption, and negative environmental impacts. A widely-adopted method to deal with traffic oscillations is adaptive cruise control (ACC), which controls the speed in pace with the preceding vehicles. The advent of vehicle-to-vehicle (V2V) communications using dedicated short-range communication (DSRC) technologies is enabling vehicles to receive additional information from other connected vehicles and the infrastructure. This will provide more opportunities for connected autonomous vehicles (CAVs) to enhance their situational awareness and performance through the implementation of more robust system-level vehicle control strategies, especially platoon-based cooperative adaptive cruise control (CACC) (Nieuwenhuijze et al., 2012).

CACC is an extension of ACC, used to minimize speed differences among vehicles in a platoon and maintain stable and safe headways between adjacent vehicles (Zhou et al., 2017). The CACC literature, discussed hereafter, assumes a platoon with pure (100%) CAVs. Typically, a CACC framework has four components (Li et al., 2015): (i) node dynamics (ND), which describes the dynamics of each vehicle in the platoon, such as second-order models (Wang et al., 2014a), or third-order models (Guo et al., 2012); (ii) vehicle-level information flow topology (VIFT) for a CAV, which describes the configuration of V2V communication links from one CAV to one or more CAVs in the platoon, for example, predecessor-following-leader (Naus et al., 2010) and two-predecessor-following (Zheng et al., 2017) VIFT schemes; (iii) decentralized controller, which uses information from other vehicles in the platoon to implement control strategies, such as Proportional-Integral-Derivative (PID) controller (Swaroop et al., 1996), sliding mode controller (Gao et al., 2018), and model predictive controller (Wang et al., 2014a; Zhou et al., 2017); and (iv) formation geometry, which describes the desired headway between vehicles. Recent studies have modeled the four components of a CAV platoon in different ways, such as the constant distance (CD) policy (Gong et al., 2016), and the constant time headway (CTH) policy (Zhou et al., 2017).

Among the four CACC framework components, the VIFT is closely related to the status of V2V communications. Almost all existing CACC studies assume identical VIFTs for all vehicles in a platoon. As discussed hereafter, consistent with the real world, our study does not constrain the VIFTs to be identical. We label the information flow topology at the platoon level as “IFT,” which illustrates the configuration of V2V communication links of all vehicles in the platoon at any time instant. By introducing the time dimension, we consider the inherent dynamics of IFT, further enhancing modeling realism. By contrast, most studies using a CACC design assume an idealized predetermined, fixed IFT. This assumption ignores the fact that the IFT (and by implication, the VIFTs) can change dynamically due to V2V communication failures (Gao et al., 2018; Talebpour et al., 2016). A communication failure may occur due to communication interference or information congestion (Kim et al., 2017; Wang et al., 2018a), especially when the ambient (pure CAV) traffic is congested. Information congestion is the reduced quality of service when a communication network node carries more data than it can handle, which in the context of V2V communications is modeled through the potential for failure of information propagation in a V2V communications-enabled traffic network (Wang et al., 2018a). Communication interference typically refers to the

disruption of a signal as it travels between a sender and a receiver. In the CACC platoon context, though the transmission distance is close enough, interference can arise due to the ambient traffic conditions. A critical reason for interference from other vehicles is the mechanism of the DSRC protocol defined by IEEE 802.11p. In telecommunications, information is transmitted via channels. If more than one sender tries to send information via the same channel at the same time, it will cause interference for both vehicles, and the resulting information collision can cause the transmission to fail. To reduce the probability of information collision, IEEE 802.11p inherits the contention mechanism from IEEE 802.11, which requires every sender to compete for the sending chance. Thereby, the probability of information collision is decreased through this mechanism. However, for V2V communications, if a sender fails to win a sending chance before a new message is generated, the old message will be dropped, and is counted as a communication failure (Qiu et al., 2015). Other factors like the hidden node effect and capture effect can also cause communication failures. In all such cases, the distance between some senders is too large for them to sense each other or to keep transmitting signals with enough magnitude so that they can be successfully received. Hence, sender-based communication failure is addressed in this study. Receiver-related failure is not considered because the spacing between vehicles in a platoon is small enough that a message can be received as long as it is sent.

If communication failures occur, a CACC with a fixed IFT (CACC-FIFT) may execute an erroneous control action or degrade to adaptive cruise control (ACC), which diminishes platoon performance related to mobility, stability, and even safety. To mitigate the negative effects of communication failure, a few studies have proposed novel CACC strategies for a pure CAV platoon by considering dynamic IFT degeneration scenarios. Here, a degeneration scenario for a given IFT refers to any configuration with one or more link communication failures for that IFT. Gong et al. (2019) propose a CACC strategy with dynamic IFT degeneration scenarios (CACC-DIFT), in which a PD controller combined with an acceleration feedforward filter is designed to counteract the IFT dynamics in the platoon. Depending on the IFT degeneration scenario that unfolds at different time instants, the CACC will change the controller parameters to maintain string stability performance rather than degrade to ACC. Gao et al. (2018) design a distributed sliding mode controller based on a linear matrix inequality method to ensure string stability under uncertain but eigenvalue-bounded IFT degeneration scenarios. However, both these studies consider IFT dynamics passively, implying that the controller uses only the functioning links when others have V2V communication failures. While such passive approaches may improve the control performance under unreliable V2V networks, their performance is constrained by ambient traffic conditions which determine the communication failure probabilities of the various IFT links. That is, when the ambient traffic density is higher, these probabilities are higher which indicates the potential lower robustness of the IFT. Further, studies (Hafeez et al. 2013) suggest that the IFT in terms of the number of vehicles in the platoon with activated “send” functionality of V2V devices within the communication range, is another key factor that impacts communication failures. That is, these failure probabilities are higher if several CAVs within communication range have their “send” functionality activated, which inspires the key idea of this study that communication failure probabilities can be reduced (i.e., the robustness of the IFT can be improved in terms of the communication reliability) by deactivating the “send” functionality of a subset of CAVs. However, we cannot deactivate the “send” functionality of all CAVs in a platoon as it will diminish the platoon’s awareness capability. If all CAVs deactivate their “send” functionality, the IFT is at its most robust in that no communication failures will occur. Then, all CAVs will operate in the ACC

mode which leads to poor theoretical performance, implying that the expected performance will not be good. By contrast, the best string stability under perfect communication conditions is achieved when all CAVs activate their “send” functionality, though the probability of communication failure is also at its highest (i.e. low robustness of IFT), indicating poor robustness for platoon control. Then, the expected string stability performance is also not good. Hence, there is a tradeoff between the theoretical string stability of an IFT and its robustness. To account for these real-world characteristics, our study proposes the novel idea of proactively controlling in real time the number of platoon vehicles with “send” functionality activated based on the unfolding ambient traffic conditions so as to enhance communication reliability, with the objective of maximizing platoon performance in terms of string stability. We label this strategy the CACC with dynamically optimized IFT, or CACC-OIFT, which aims to achieve this tradeoff and enhance the expected platoon performance in terms of the string stability with communication constraints.

Enabling the CACC-OIFT strategy entails addressing some key challenges. First, to account for the time-varying nature of communication failures, all degeneration scenarios of an IFT and their probabilities should be determined. The probability of each degeneration scenario depends on the probability of the communication failure of each link in the IFT, which is itself dynamic and depends on the unfolding traffic conditions. Second, the platoon control performance in terms of string stability needs to be theoretically formulated in the expected sense over all degeneration scenarios for an IFT. While the existing literature uses simulation-based methods (Swaroop et al., 1996; Schakel et al., 2010; Nieuwenhuijze et al., 2012; Zhou et al., 2017) to numerically determine control performance, it is difficult to integrate such approaches in a rigorous optimization model. Third, an adaptive controller is needed to control the car-following behaviors of the vehicles in the CAV platoon based on the unfolding degeneration scenarios for the optimal IFT at different time instants. Hence, there is the need to factor IFT dynamics while ensuring string stability.

The proposed CACC-OIFT strategy for a time period seeks to determine the optimal IFT that maximizes the expected string stability performance to damp traffic oscillations by deactivating or activating the “send” functionality of the V2V communication devices of the vehicles in the platoon, and deploys it for every time instant within that period based on the unfolding degeneration scenarios for that IFT due to V2V communication failures. It includes an IFT optimization model and an adaptive Proportional-Derivative (PD) controller. Fig. 2.1 illustrates the conceptual flowchart of CACC-OIFT and its operational deployment. Fig. 2.1(a) shows the various components of CACC-OIFT and their linkages in the time dimension. Given the ambient traffic conditions and platoon size at some time instant  $\Delta\tau$  before the start of time period  $\tau$  (the period from time instant  $t_\tau$  to  $t_{\tau+1}$  (i.e.,  $[t_\tau, t_{\tau+1})$ ) in Fig. 2.1(b)), the IFT optimization model first identifies the candidate IFTs corresponding to the platoon size and their degeneration scenarios. Note that the set of all possible IFTs and their degenerations scenarios is determined offline as they are time-invariant and can be predetermined. The subset of IFTs corresponding to the current platoon size denotes the candidate IFT set. Second, the ambient traffic conditions are used to determine the probabilities of the degeneration scenarios for each candidate IFT as these traffic conditions determine the V2V (link) communication failure probabilities. Third, the string stability for each degeneration scenario for each candidate IFT is obtained from the predetermined string stabilities for all degeneration scenarios for all possible IFTs, computed offline using the transfer function in frequency domain of the given adaptive PD controller. This study uses the speed oscillation energy of the platoon as an indicator of string stability performance, which treats the speed oscillation as a signal and computes the sum of speed oscillation energies of all vehicles in

the platoon in frequency domain. A lower value for this sum implies that traffic oscillations are damped as they propagate through the platoon, implying better string stability. The optimal IFT (activations and deactivations of “send” functionalities for the platoon vehicles) for time period  $\tau$  is determined as the candidate IFT which has the maximum expected string stability across all of its degeneration scenarios.

As shown in Fig. 2.1(b), the IFT optimization model will determine the optimal IFT for time period  $\tau$  at time instant  $t_\tau - \Delta\tau$  as it takes  $\Delta\tau$  time to solve for the optimal IFT. Note that it is assumed that the ambient traffic conditions and platoon size do not vary within the time period. From Fig. 2.1(a), the operational deployment of CACC-OIFT starts by proactively deploying the optimal IFT for the first time instant  $t_\tau$  of period  $\tau$ . However, due to V2V communication failures, different time instants in period  $\tau$  can have a different degeneration scenario of the optimal IFT manifest. The adaptive PD controller continuously determines the car-following behaviors of the vehicles based on the unfolding degeneration scenario for each time instant (i.e.,  $t_\tau, t_\tau + 1, \dots, t_{\tau+1}$ ) in period  $\tau$ , thereby controlling vehicular location and dynamics. As shown in Fig. 2.1(b), at  $t_{\tau+1} - \Delta\tau$ , the IFT optimization model will update the optimal IFT for the next time period  $\tau + 1$ . This process continues for the time horizon of interest.

In CACC-OIFT implementation, after the leading vehicle receives information on ambient traffic conditions at  $t_\tau - \Delta\tau$ , it distributes computational tasks to the other platoon vehicles which perform these computations in parallel to enable computational efficiency. Then, the leading vehicle collects the results of the computations and determines the optimal IFT to deploy in the next cycle. This ensures that the computing process is completed within  $\Delta\tau$ . Note that the length of each time period  $\tau$  is flexible; however, we only update the optimal IFT when the platoon size or the ambient traffic state related to the traffic oscillations changes. According to Li et al. (2010), the time-invariant pattern of traffic oscillations usually lasts more than 10 minutes, suggesting possible values for the update frequency.

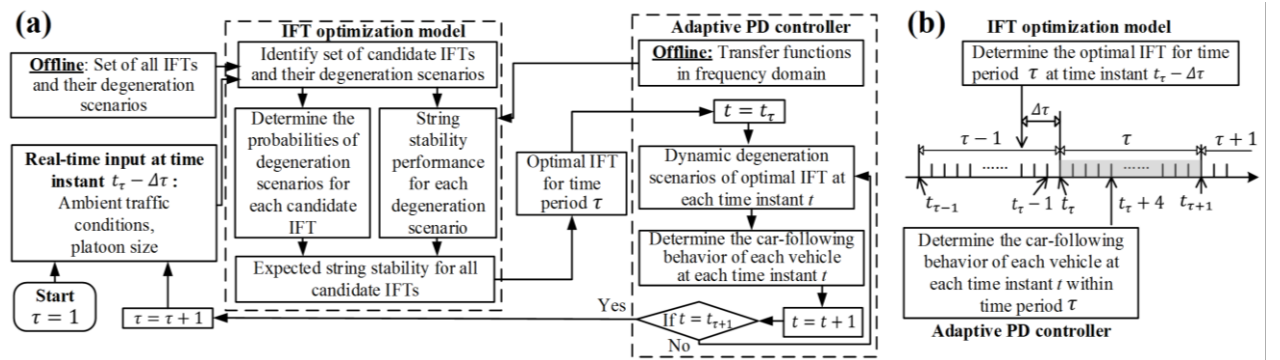


Figure 2.1. (a) Conceptual flowchart of CACC-OIFT; (b) Operational deployment of CACC-OIFT.

As the IFT optimization model optimizes the IFT for each time period  $\tau$  and the adaptive PD controller controls the car-following behaviors for each time instant  $t$ , we will formulate the IFT optimization model for one time period in Section 2.3 and the adaptive PD controller for a time instant within that time period in Section 2.4. Hence, for notational convenience, we will omit  $\tau$  and  $t$  in these sections. A two-step algorithm is developed to solve the IFT optimization problem,

and several critical properties are proved; for example, the leading vehicle in the platoon should always activate its “send” functionality. The effectiveness of the proposed CACC is validated using NGSIM field data (US DOT, 2007) in network simulator NS-3. The results reveal that the algorithm can solve the IFT optimization model for a platoon of considerable size (15 CAVs) in a practically deployable time duration (less than a minute). The proposed CACC-OIFT can significantly damp traffic oscillations and enhance string stability in an unreliable V2V communications context, outperforming CACCs with fixed IFTs or with passive adaptive schemes for IFT dynamics.

The major contributions of the paper are as follows:

We propose an IFT optimization model to explicitly factor the inherent IFT dynamics, and leverage it proactively to enhance CACC performance. Compared to passive schemes that simply acknowledge communication failures, a key innovation is to determine the optimal IFT by dynamically and proactively activating or deactivating communication devices of some CAVs in the platoon so as to mitigate negative effects of communication failures and maximize string stability while factoring communication constraints.

As another key innovation, the speed oscillation energy in frequency domain is used to evaluate the platoon control performance (i.e., string stability) for a given IFT degeneration scenario. This study treats the speed oscillation as a signal and determines the oscillation energy of each vehicle based on the transfer function of the given controller. The expected oscillation energy for an IFT is the weighted sum of the oscillation energies over all possible degeneration scenarios. Minimizing the expected speed oscillation energy implies maximizing the expected string stability.

To account for the manifestation of different degeneration scenarios of the optimal IFT at different time instants within the time period, we design an adaptive control based on PD feedback controller and acceleration feedforward filter. When the IFT degenerates, the controller determines each vehicle’s car-following behavior based on the information it receives at that time instant so that string stability is maintained.

To the best of our knowledge, this is the first study to use rigorous mathematical analysis to improve platoon performance by proactively leveraging IFT dynamics and adjusting adaptive controller parameters. It contributes to the literature in this area and informs the design of CAV platoon control in practice.

The remainder of the paper is organized as follows. Section 2.2 briefly introduces IFT and degeneration scenarios. Section 2.3 formulates the IFT optimization model. Section 2.4 formulates the adaptive controller for an IFT and its degeneration scenarios. Section 2.5 discusses several critical properties of the proposed CACC-OIFT strategy and discusses the solution algorithm for the IFT optimization problem. Section 2.6 discusses simulation-based numerical experiments and analyzes the results. Section 2.7 provides some concluding comments.

## **2.2 IFT and degeneration scenarios**

Though the one-predecessor-following VIFT is the most commonly-used scheme, the more computationally intensive<sup>1</sup> two-predecessor-following VIFT is used in this study to illustrate the CACC-OIFT strategy. It should be noted that our model can be extended to a k-predecessor-

---

<sup>1</sup> In a VIFT, if the V2V device sends information to  $c$  other devices, it has  $2^c$  communication statuses.

following VIFT without loss of generality; however, computational efficiency and communication reliability issues can arise as more predecessors are considered. Fig. 2.2 shows a CAV platoon in which a fully-activated two-predecessor-following VIFT is used in the proposed adaptive PD controller. The information of each CAV is delivered to the two vehicles immediately following it through V2V communications. CAV  $i$  obtains the state of its two predecessors ( $i - 1$  and  $i - 2$ ), such as location ( $x_{i-1}$  and  $x_{i-2}$ ), speed ( $\dot{x}_{i-1}$  and  $\dot{x}_{i-2}$ ) and acceleration ( $\ddot{x}_{i-1}$  and  $\ddot{x}_{i-2}$ ), through V2V communications. Also, vehicle  $i$  can detect the kinematic state ( $x_{i-1}$  and  $\dot{x}_{i-1}$ ) of its immediate predecessor  $i - 1$  through onboard sensors such as radar, Lidar and camera, and its own kinematic state through GPS. The ambient traffic conditions, such as average density  $\bar{k}$  and the trajectory oscillations in frequency domain  $X(j\omega)$ , can be obtained through vehicle-to-infrastructure (V2I) communications, where  $\omega$  is the angular frequency, and  $j = \sqrt{-1}$ .

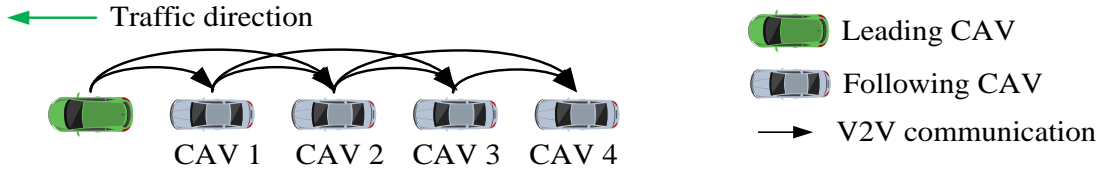


Figure 2.2. CAV platoon with a two-predecessor-following VIFT scheme.

Since CACC-OIFT involves dynamically deactivating or activating the “send” functionality of V2V communication devices for vehicles in the platoon, we introduce a vector  $\xi = [\eta_0, \eta_1, \dots, \eta_N]$ ,  $\eta_i \in \{0, 1\}$  for  $i = 0, 1, \dots, N$  to indicate the IFT of a platoon with  $N + 1$  vehicles, where  $\eta_i$  indicates the status of the V2V communication device of vehicle  $i$ :  $\eta_i = 0$ , when “send” functionality of V2V communication is deactivated; otherwise,  $\eta_i = 1$ . For example, the IFT in Fig. 2.2 has  $\xi = [1, 1, 1, 1, 1]$ . If some vehicles turn off their “send” functionality, such as vehicles 1, 3 and 4 in Fig. 2.3(a), the IFT has  $\xi = [1, 0, 1, 0, 0]$ . We denote  $\Omega$  as the set of all possible IFTs that follow the two-predecessor-following scheme.

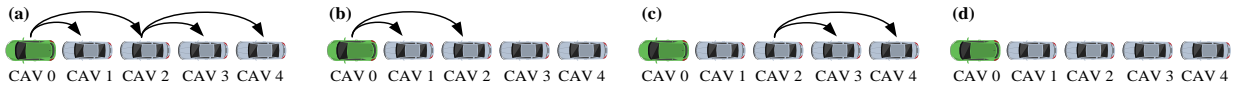


Figure 2.3. Example of an IFT and its degeneration scenarios: (a) IFT with “send” functionalities of CAVs 1, 3 and 4 deactivated; (b) Degeneration scenario with CAV 2 failing to send message; (c) Degeneration scenario with CAV 0 failing to send message; (d) Degeneration scenario with both CAVs 0 and 2 failing to send messages.

Though temporarily switching off V2V communications of some vehicles can improve the success rate of other V2V communication links, communication failures cannot be eliminated as they also depend on ambient traffic conditions. As discussed earlier, we focus on failures involving the sending process. Due to sender failure, IFT  $\xi$  has degeneration scenarios  $\xi_d$  with probabilities  $P_d(\xi_d)$ , which can be formulated in a contention model of V2V communications (Qiu et al., 2015). Here,  $d$  is the index of degeneration scenarios,  $d = 1, \dots, D(\xi)$ , where  $D(\xi) = 2^{\sum_{i=0}^N \eta_i}$ . The

<sup>2</sup> The traffic oscillation in frequency domain measures oscillation amplitudes in different frequencies, which can be obtained through Fourier Transform of the ambient vehicles’ trajectory data.

degeneration scenario satisfies  $\xi_d(\xi) = [\eta_{0,d}, \eta_{1,d}, \dots, \eta_{N,d}]$ ,  $\eta_{i,d} \in \{0, 1\}$ ,  $\eta_{i,d} \leq \eta_i$  for  $i = 0, 1, \dots, N$ , which indicates that sender failure only exists for a vehicle with an activated “send” functionality. Hence, degeneration scenario  $\xi_d$  is related to IFT  $\xi$ . For example, the IFT  $\xi = [1, 0, 1, 0, 0]$  in Fig. 2.3(a) has four degeneration scenarios:  $\xi_1(\xi) = [1, 0, 1, 0, 0]$ ,  $\xi_2(\xi) = [1, 0, 0, 0, 0]$ ,  $\xi_3(\xi) = [0, 0, 1, 0, 0]$  and  $\xi_4(\xi) = [0, 0, 0, 0, 0]$ , which are shown in Figs. 2.3 (a)-(d), respectively. We denote  $\Omega_d(\xi)$  as the set of all possible degeneration scenarios  $\xi_d(\xi)$  for IFT  $\xi$ .

To illustrate the need for controller design, we also analyze the V2V communication status from the receiver side. Based on different sender failures or deactivated “send” functionalities, a receiver (i.e., vehicle  $i$  in Fig. 2.4) has four possible communication statuses (Figs. 2.4(a)-(d)). For a following vehicle  $i$ , if both predecessors (i.e.,  $i - 1$  and  $i - 2$ ) activate communication devices and send information successfully, then the following vehicle  $i$  will be controlled by a CACC1 controller with the two-predecessor-following scheme in Fig. 2.4(a). Figs. 2.4(b) and (c) show the cases where one sender fails to broadcast its message. In these cases, CAV  $i$  can detect the kinematic state of its immediate predecessor  $i - 1$ , and obtain one predecessor vehicle’s acceleration through V2V communications. When both senders fail (Fig. 2.4(d)), CAV  $i$  detects the surrounding environment only through onboard sensors. Then, the CACC will degrade to ACC to update the acceleration command based on the relative spacing and speed between CAVs  $i$  and  $i - 1$ . Accordingly, a vector is introduced  $\zeta(\xi_d) = [\zeta_1(\xi_d(\xi)), \dots, \zeta_N(\xi_d(\xi))]$ ,  $\zeta_i \in \{1, 2, 3, 4\}$  for  $i = 0, 1, \dots, N$  in Equation (2.1) to indicate receiver status of a platoon with a degeneration scenario  $\xi_d$ , where  $\zeta_i(\xi_d(\xi)) = 1, 2, 3, 4$  indicates that vehicle  $i$  is controlled by CACC1, CACC2, CACC3, or ACC, respectively.

$$\zeta(\xi_d(\xi)) = \begin{bmatrix} \zeta_0(\xi_d(\xi)) \\ \zeta_1(\xi_d(\xi)) \\ \vdots \\ \zeta_N(\xi_d(\xi)) \end{bmatrix}^T = \begin{bmatrix} 4 \\ 4 \\ \vdots \\ 4 \end{bmatrix}^T - \xi_d(\xi) \begin{bmatrix} 0 & 2 & 1 & 0 & \dots & 0 \\ \vdots & 0 & 2 & \ddots & \ddots & \vdots \\ \vdots & \ddots & \ddots & \ddots & \ddots & 0 \\ \vdots & \ddots & \ddots & \ddots & 2 & 1 \\ \vdots & \ddots & \ddots & \ddots & 0 & 2 \\ 0 & \dots & \dots & \dots & \dots & 0 \end{bmatrix} \quad (2.1)$$

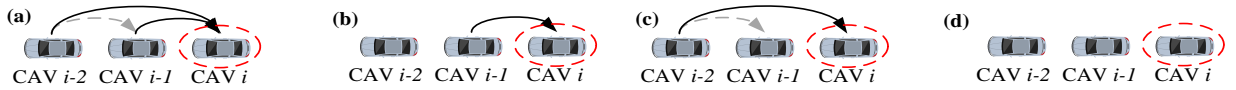


Figure 2.4. Communication statuses of: (a) CACC1; (b) CACC2; (c) CACC3; (d) ACC.

### 2.3 Formulation of optimization model for IFT

This section analytically derives the IFT optimization model for a time period. As discussed earlier, due to the dynamics of V2V communication failures, a platoon with IFT  $\xi$  may operate under different time-varying degeneration scenarios  $\xi_d(\xi)$  at different time instants with corresponding probabilities  $P_d(\xi_d(\xi))$ . The probabilities of degeneration scenarios of IFT  $\xi$  satisfy  $\sum_{\xi_d(\xi) \in \Omega_d(\xi)} P_d(\xi_d(\xi)) = 1$ . The platoon control performance is a function of the degeneration scenarios. Since degeneration scenario  $\xi_d$  is a function of IFT  $\xi$ , the control performance under it is denoted by  $E_d(\xi_d(\xi))$ . By considering all possible degeneration scenarios  $\Omega_d(\xi)$ , the expected

platoon control performance  $E(\xi)$  for IFT  $\xi$  under communication failures is:

$$E(\xi) = \sum_{\xi_d(\xi) \in \Omega_d(\xi)} P_d(\xi_d(\xi)) E_d(\xi_d(\xi)) \quad (2.2)$$

Hence, the choice of IFT  $\xi$  significantly affects the expected platoon performance, implying the need to determine the IFT that optimizes the expected performance  $E(\xi)$  under the CACC strategy. Optimizing the IFT in terms of  $E(\xi)$  aims to achieve tradeoff between the control performance under perfect communication conditions and the robustness of the IFT in terms of communication reliability. We summarize the IFT optimization model, denoted as OPT-I, as follows:

$$\begin{aligned} \text{OPT-1} \quad & \underset{\xi \in \Omega}{\text{OPT}} E(\xi) = \sum_{\xi_d(\xi) \in \Omega_d(\xi)} P_d(\xi_d(\xi)) E_d(\xi_d(\xi)) \\ \text{s.t} \quad & \xi = [\eta_0, \eta_1, \dots, \eta_N], \eta_i \in \{0, 1\} \text{ for } i = 0, 1, \dots, N \\ & \cdot \\ & \Omega = \{[\eta_0, \eta_1, \dots, \eta_N] \mid \eta_i \in \{0, 1\} \text{ for } i = 0, 1, \dots, N\} \\ & \xi \in \Omega \\ & \xi_d(\xi) = [\eta_{0,d}, \eta_{1,d}, \dots, \eta_{N,d}], \eta_{i,d} \in \{0, 1\}, \eta_{i,d} \leq \eta_i \text{ for } i = 0, 1, \dots, N \\ & \Omega_d(\xi) = \{[\eta_{0,d}, \eta_{1,d}, \dots, \eta_{N,d}] \mid \eta_{i,d} \in \{0, 1\}, \eta_{i,d} \leq \eta_i \text{ for } i = 0, 1, \dots, N\} \\ & \sum_{\xi_d(\xi) \in \Omega_d(\xi)} P_d(\xi_d) = 1, \text{ for any } \xi \in \Omega \end{aligned} \quad (2.3)$$

The first three constraints of OPT-I relate to the decision variable  $\xi$ . The first constraint states that  $\xi$  is a binary 0-1 vector. The second constraint is the set  $\Omega$  of IFTs  $\xi$  corresponding to the two-predecessor-following VIFT. The third constraint states that  $\xi$  belongs to  $\Omega$ . The remaining three constraints correspond to the degeneration scenario  $\xi_d(\xi)$ . The fourth constraint shows the relationship between degeneration scenario  $\xi_d(\xi)$  and IFT  $\xi$ . The fifth constraint indicates that the set  $\Omega_d(\xi)$  includes all possible degeneration scenarios for IFT  $\xi$ . The last constraint states that the probabilities of the degeneration scenarios for an IFT  $\xi$  should sum up to 1.

Next, in Section 2.3.1, the platoon control performance is first characterized in terms of the speed oscillation energy of the vehicles in the platoon, which is then linked to string stability. Section 2.3.2 first discusses the determination of the probabilities of the degeneration scenarios. Then, it characterizes the expected string stability for an IFT  $\xi$  in terms of the speed oscillation energies of the platoon vehicles. Finally, the IFT optimization model is formulated in terms of optimizing the expected speed oscillation energies to reflect the expected string stability. Note that other performance metrics like energy consumption and cost can be included in this model using additional weighted terms in the objective function or by adding external constraints. Further, the focus on string stability does not affect safety considerations in the sense that channels (Qiu et al., 2015) used to propagate safety-related messages are different from those used for beacon messages

(which represent the focus of this study).

### **2.3.1 Speed oscillation energy of a degeneration scenario for an IFT and its linkage to string stability**

The traffic oscillations can be measured by the speed profiles of vehicles in the traffic flow (Li et al., 2012), which can be interpreted as a signal with specific energy density propagating through a certain medium (i.e., a platoon of vehicles). Correspondingly, this study quantifies traffic oscillations by introducing speed oscillation energy  $e_i$  in frequency domain for vehicle  $i$ :

$$e_i = \int_0^{+\infty} V_i^2(j\omega) d\omega \quad (2.4)$$

where  $j = \sqrt{-1}$ .  $V_i^2(j\omega)$  is the Energy Spectral Density (ESD) of vehicle speed. Thereby, the oscillation energy of a vehicle can be calculated by integrating its speed ESD over all frequencies. The speed oscillation energy of all vehicles in a platoon under a degeneration scenario  $\xi_d(\xi)$  is given by:

$$E_d(\xi_d(\xi)) = \sum_{i=0}^N e_i = \sum_{i=0}^N \left[ \int_0^{+\infty} V_i^2(j\omega) d\omega \right] \quad (2.5)$$

Since a platoon with CACC is an interconnected system, the speed oscillation energy of each following vehicle will be determined by the speed oscillation energy of its predecessors and the characteristics of its CACC controller. The relationship between the speed oscillation energy of the leading vehicle 0 and any following vehicle  $i$  can be obtained by recursively linking the speed oscillation energy of the following vehicle and its predecessors. As discussed in Section 2.2, the trajectory oscillation information can be directly obtained through V2I communications, unlike speed oscillation information which is an indirect second-order effect. Hence, based on the CACC controller used in degeneration scenario  $\xi_d(\xi)$ , a transfer function  $SS_{X,i}(j\omega, \xi_d(\xi))$  is introduced to measure the propagation of trajectory oscillations in frequency domain from the leading vehicle 0 to any following vehicle  $i$ :

$$SS_{X,i}(j\omega, \xi_d(\xi)) = \frac{X_i(j\omega)}{X_0(j\omega)}, \quad i = 1, \dots, n \quad (2.6)$$

where  $X_i(j\omega)$  is the position frequency response of vehicle  $i$ . Next, we assume that the position frequency response of the leading vehicle  $X_0(j\omega)$  follows the ambient traffic oscillations in frequency domain  $X(j\omega)$  (i.e.,  $X_0(j\omega) = X(j\omega)$ ), since the movement of the leading vehicle is affected by the ambient traffic oscillations.

Given the degeneration scenario  $\xi_d(\xi)$ ,  $SS_{X,i}(j\omega, \xi_d(\xi))$  is a function of  $\omega$  with a set of predetermined controller parameters. Different transfer functions will be generated under different controllers and IFT degeneration scenarios. Section 2.4 provide more details on  $SS_{X,i}(j\omega, \xi_d(\xi))$ .

Next, we derive the speed frequency response  $V_i(j\omega)$  for all vehicles using the leading vehicle position frequency response  $X_0(j\omega)$  information. To do so, first, the inverse Fourier transform is performed to obtain the trajectory information of vehicle  $i$  in time domain.

$$\begin{aligned} x_i(t) &= \int_0^{+\infty} X_i(j\omega) e^{2\pi t j\omega} d\omega \\ &= \int_0^{+\infty} SS_{X,i}(j\omega, \xi_d(\xi)) X_0(j\omega) e^{2\pi t j\omega} d\omega \end{aligned} \quad (2.7)$$

Then, the derivative of the vehicle trajectory provides the speed profile of vehicle  $i$  in time domain.

$$v_i(t) = \frac{dx_i(t)}{dt} = \int_0^{+\infty} 2\pi j\omega SS_{X,i}(j\omega, \xi_d(\xi)) X_0(j\omega) e^{2\pi t j\omega} d\omega \quad (2.8)$$

Comparing Equation (2.8) with the inverse Fourier transform of speed frequency response in Equation (2.9),

$$v_i(t) = \int_0^{+\infty} V_i(j\omega) e^{2\pi t j\omega} d\omega \quad (2.9)$$

the speed frequency response is derived as follows:

$$V_i(j\omega) = 2\pi j\omega SS_{X,i}(j\omega, \xi_d(\xi)) X_0(j\omega) \quad (2.10)$$

Combining Equations (2.5) and (2.10), the speed oscillation energy of the vehicles in the platoon under a degeneration scenario  $\xi_d(\xi)$  can be formulated as:

$$\begin{aligned} E_d(\xi_d(\xi)) &= \sum_{i=0}^N \int_0^{+\infty} V_i^2(j\omega) d\omega \\ &= 4\pi^2 \sum_{i=0}^N \int_0^{+\infty} \omega^2 SS_{X,i}^2(j\omega, \xi_d(\xi)) X_0^2(j\omega) d\omega \end{aligned} \quad (2.11)$$

The transfer function  $SS_{X,i}(j\omega, \xi_d(\xi))$  is commonly used to infer string stability (Naus et al., 2010). A lower value for  $SS_{X,i}(j\omega, \xi_d(\xi))$  reflects better string stability performance as it implies smoother traffic flow. From Equation (2.11), for a given leading vehicle position frequency response  $X_0(j\omega)$ , a smaller platoon speed oscillation energy  $E_d(\xi_d(\xi))$  indicates a lower  $SS_{X,i}(j\omega, \xi_d(\xi))$ , implying better string stability performance.

### **2.3.2 Probabilities of degeneration scenarios and expected string stability for an IFT**

Since the optimal IFT implies that some vehicles have their “send” functionality activated and others have it deactivated, a communication failure implies that an activated “sender” vehicle fails to broadcast its message at a specific time instant. This is a manifestation of a degeneration scenario for this IFT. As discussed in Section 2.2.1, sender failure relates to information collision during message broadcasting in the DSRC protocol. This collision occurs when two senders within communication range send information to a receiver at the same time. During the sending process, each sender uses a contention window (CW) to compete for a sending chance. Each sender will randomly select an integer value in the range of  $[0, CW - 1]$ , to determine when in this window it will send the message. If more than one sender chooses the same integer value, a collision occurs. Note that we use the DSRC protocol here as an example of the communication protocol to illustrate our CACC-OIFT strategy because it is a mature

and proven technology that has been invested in by both the public and private sectors. However, the proposed strategy can be used with any communication protocol with capacity upper bound where the communication success rate depends on the density of vehicles with communication ability. Hence, it is always possible to improve platoon performance by optimizing IFT as in the future more information (traffic, entertainment, weather, e-commerce, etc.) will sought to be propagated or shared among vehicles, even if high-capacity protocols such as 5G are ultimately adopted.

In the MAC level protocol (i.e., IEEE 802.11), collision probability can be reduced by increasing the contention window CW size and/or implementing a retransmission scheme. However, both these methods increase time delay, reducing the timeliness of information propagation. For example, if a collision happens, the sender will choose a new contention window and attempts to retransmit the same information after the previous contention window ends (Hafeez et al. 2013). This will lead to delays in the information reaching the receiver, worsening the performance of the real-time controller. Hence, these two methods are not suitable for CACC. Further, as information is generated continuously in the CAV context, if a sender fails to win the sending chance before the next information is generated, the previous information will be dropped, and will therefore also be identified as a sender failure (Qiu et al. 2015). Therefore, a retransmission scheme is not considered here and the contention window CW size is set to a small value. Also, usually communication time delay is not large compared to the control sampling period and will not significantly impact platoon performance. Based on these assumptions, we do not consider communication delay here.

In Qiu et al. (2015), a contention model with saturated and unsaturated communication traffic is developed using a Markov chain. The success rate of sending message for vehicle  $i$  is:

$$p_{i,sat} = 2(1 - b_i)(1 - 2b_i + CW)^{-1} \quad (2.12)$$

where the channel busy rate  $b_i$  for sender vehicle  $i$  is:

$$b_i = 1 - e^{-\bar{\rho}_i(\xi)p_{i,sat}} \quad (2.13)$$

Here,  $\bar{\rho}_i(\xi)$  is the average number of vehicles with activated “send” functionalities within communication range  $R$  of vehicle  $i$ . Given the average density ( $\bar{k}$ ) of the ambient traffic flow, the average number of vehicles within the communication range  $R$  is given by  $m = \lfloor R\bar{k} \rfloor$ . Then, the vector of  $\bar{\rho}(\xi) = [\bar{\rho}_0(\xi), \bar{\rho}_1(\xi), \dots, \bar{\rho}_N(\xi)]$  is:

$$\bar{\rho}(\xi) = \xi \mathbf{M}(\bar{k}) \quad (2.14)$$

where,  $\mathbf{M}(\bar{k})$  is a N-by-N  $2m + 1$  diagonal matrix whose non-zero elements are 1 if  $m < N$ . Otherwise, M is a N-by-N matrix in which all elements have the value 1.

Combining Equations (2.12) and (2.13), the success rate of sending,  $p_{i,sat}$ , can be solved numerically based on a method by Qiu et al. (2012), and for an IFT  $\xi$ , is denoted as  $p_{i,sat}(\xi)$ . Since the V2V device bandwidth and its impact are not considered, a contention model with unsaturated communication is implemented (Qiu et al., 2015). The success rate  $p_{i,unsat}$  of a sender vehicle  $i$  in one attempt is:

$$p_{i,unsat}(\xi) = [k_1 \log(\bar{\rho}_i(\xi)) + k_2 CW + k_3] p_{i,sat}(\xi) \quad (2.15)$$

where  $k_1, k_2, k_3$  are fitting coefficients. In our numerical experiments, they are fitted using the simulation results in NS-3 through linear regression.

After obtaining the success rate of a sender vehicle, the probabilities of the degeneration scenarios of an IFT due to sender failure can be calculated. When the IFT degenerates from  $\xi$  to  $\xi_d$ , two sets  $A_d(\xi_d(\xi))$  and  $B_d(\xi_d(\xi))$  are introduced for the indices of vehicles with successful and unsuccessful broadcast status, respectively, which satisfy  $A_d(\xi_d(\xi)) = \{i | \eta_i = 1, \eta_{i,d} = 1, i = 0, \dots, N\}$  and  $B_d(\xi_d(\xi)) = \{i | \eta_i = 1, \eta_{i,d} = 0, i = 0, \dots, N\}$ . Hence, the probability of the degeneration from  $\xi$  to  $\xi_d$  is:

$$P_d(\xi_d(\xi)) = \prod_{i \in A_d(\xi)} p_{i,\text{unsat}} \prod_{i \in B_d(\xi)} (1 - p_{i,\text{unsat}}) \quad (2.16)$$

The probability of each degeneration scenario is independent of its string stability performance. By substituting Equations (2.11) and (2.16) into OPT-I, the optimization model can be reformulated as OPT-II.

$$\begin{aligned} &\text{OPT-II} \\ &\min_{\xi \in \Omega} 4\pi^2 \sum_{\xi_d(\xi) \in \Omega_d(\xi)} \left[ \prod_{i \in A_d(\xi)} p_{i,\text{unsat}} \sum_{i \in B_d(\xi)} (1 - p_{i,\text{unsat}}) \sum_{i=1}^N \int_0^{+\infty} \omega^2 SS_{X,i}^2(j\omega, \xi_d(\xi)) X_0^2(j\omega) d\omega \right] \quad (2.17) \\ &\text{s.t.} \quad \xi = [\eta_0, \eta_1, \dots, \eta_N], \eta_i \in \{0, 1\} \text{ for } i = 0, 1, \dots, N \\ &\quad \Omega = \{[\eta_0, \eta_1, \dots, \eta_N] | \eta_i \in \{0, 1\} \text{ for } i = 0, 1, \dots, N\} \\ &\quad \xi \in \Omega \\ &\quad \xi_d(\xi) = [\eta_{0,d}, \eta_{1,d}, \dots, \eta_{N,d}], \eta_{i,d} \in \{0, 1\}, \eta_{i,d} \leq \eta_i \text{ for } i = 0, 1, \dots, N \\ &\quad \Omega_d(\xi) = \{[\eta_{0,d}, \eta_{1,d}, \dots, \eta_{N,d}] | \eta_{i,d} \in \{0, 1\}, \eta_{i,d} \leq \eta_i \text{ for } i = 0, 1, \dots, N\} \\ &\quad \sum_{\xi_d(\xi) \in \Omega_d(\xi)} P_d(\xi_d) = 1, \text{ for any } \xi \in \Omega \\ &\quad A_d(\xi_d(\xi)) = \{i | \eta_i = 1, \eta_{i,d} = 1, i = 0, \dots, N\} \\ &\quad B_d(\xi_d(\xi)) = \{i | \eta_i = 1, \eta_{i,d} = 0, i = 0, \dots, N\} \end{aligned}$$

OPT-II is a mixed binary-integer optimization problem. It is almost identical to OPT-I, but has two additional constraints at the end related to the successful and unsuccessful broadcast status under the degeneration scenario  $\xi_d(\xi)$  for IFT  $\xi$ , respectively. The objective function seeks the IFT whose most likely degeneration scenarios have lower speed oscillation energies (or, higher string stability performance). Section 2.5 proposes an algorithm to solve OPT-II and discusses its characteristics.

## 2.4 Formulation of adaptive controller for degeneration scenarios of IFT

We propose an adaptive Proportional-Derivative (PD) controller based on a two-predecessor-following scheme. First, we introduce the control structure (including vehicle dynamics, spacing policy, and feedforward and feedback sub-controllers) that can adapt to any IFT and its

degeneration scenarios. Next, we determine several critical parameters to ensure the head-to-tail string stability of the platoon and improve the capability for measurement noise mitigation for individual vehicles. The transfer function  $SS_{X,i}(j\omega, \xi_d(\xi))$  is used in the IFT optimization model as the indicator of string stability performance for all degeneration scenarios  $\xi_d(\xi)$  of IFT  $\xi$ .

### 2.4.1 Control structure

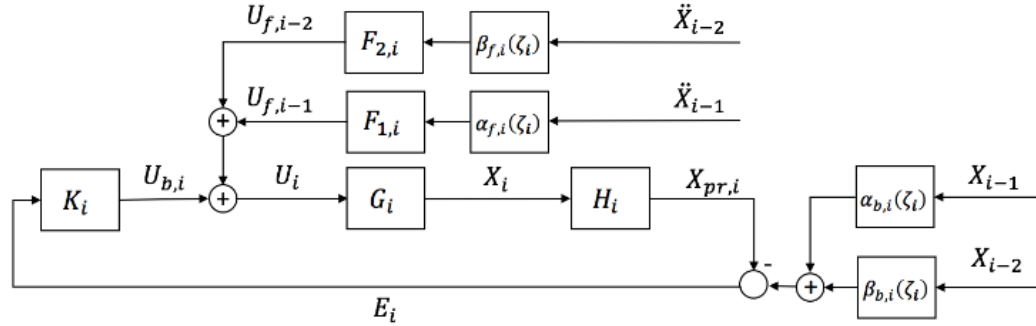


Figure 2.5. Schematic of the adaptive PD controller.

The schematic of the adaptive PD controller for vehicle  $i$  is illustrated in Fig. 2.5.  $U_i$  represents the control command, which consists of control feedback  $U_{b,i}$  from the spacing error  $E_i$  and two extra feedforward terms  $U_{f,i-1}$  and  $U_{f,i-2}$  from the acceleration rates  $\ddot{X}_{i-1}$  and  $\ddot{X}_{i-2}$ , respectively. In the case of ACC,  $U_i$  merely consists of a feedback control command.  $X_i$  is the position output of vehicle  $i$ ,  $X_{pr,i}$  is the processed position output of vehicle  $i$  after considering the spacing policy,  $X_{i-1}$  is the feedback position information from the immediate predecessor while  $X_{i-2}$  is the feedback position information from the second predecessor.  $K_i$  is the feedback controller which generates a control command to rectify the spacing error.  $G_i$  represents the ideal longitudinal vehicle dynamics.  $H_i$  denotes the spacing policy (i.e., such as CD or CTH), and  $F_{1,i}$  and  $F_{2,i}$  are feedforward filters to process the acceleration information from the corresponding predecessors.  $\alpha_{b,i}(\zeta_i)$  and  $\beta_{b,i}(\zeta_i)$  are weighting coefficients for position feedback information while  $\alpha_{f,i}(\zeta_i)$  and  $\beta_{f,i}(\zeta_i)$  are weighting coefficients for acceleration feedforward information. These coefficients are determined by the dynamic IFT; specific coefficient settings for each IFT scenario are shown in Table 2.1.

Table 2.1. Weighting coefficient settings.

	$\zeta_i$	$\alpha_{b,i}(\zeta_i)$	$\alpha_{f,i}(\zeta_i)$	$\beta_{b,i}(\zeta_i)$	$\beta_{f,i}(\zeta_i)$
CACC1	1	$\alpha$	$\alpha$	$\beta$	$\beta$
CACC2	2	1	1	0	0
CACC3	3	1	0	0	1
ACC	4	1	0	0	0

The extra constraints for CACC1 are:

$$\alpha + \beta = 1, 0 < \alpha, \beta < 1 \quad (2.18)$$

CACC1 has two predecessors with activated “send” functionality; thereby, the weighting coefficients of feedback and feedforward information are both greater than zero. The weighting coefficients  $\alpha$  and  $\beta$  represent the relative importance of the information from the immediate and second predecessors, respectively. As CACC2 only has the immediate predecessor with activated “send” functionality, the weighting coefficient of the information from the second predecessor is zero. Similarly, the weighting coefficient of the information from the immediate predecessor in CACC3 is zero, and both weighting coefficients in ACC case are zero.

#### 2.4.1.1 Vehicle dynamics

This study considers an idealized longitudinal vehicle dynamics model, ignoring air drag, rolling resistance and actuator delay (Li et al., 2015) in the model. This model is selected because the study focuses on upper-level control design (damping traffic oscillations), and assumes that the lower-level controller can address vehicle internal dynamics so that the vehicle can respond to acceleration commands without delays. Additionally, it is common to use such an idealized model for system-level platoon control design (Gong et al., 2016; Zhou et al., 2017). The linearized state-space representation of the idealized longitudinal vehicle dynamics can be represented as:

$$\dot{x}_i(t) = v_i(t), \quad \dot{v}_i(t) = u_i(t) \quad (2.19)$$

where  $x_i(t)$ ,  $v_i(t)$ , and  $u_i(t)$  are the absolute position, velocity and acceleration of vehicle  $i$  at time  $t$ , respectively.

To analyze stability performance, the modeling and analysis are performed in the Laplace domain. The idealized longitudinal vehicle dynamics model in the Laplace domain can be described by using a transfer function:

$$G_i(s) = X_i(s)U_i(s)^{-1} = s^{-2} \quad (2.20)$$

where the input  $U_i(s)$  denotes the acceleration of vehicle  $i$  and the output  $X_i(s)$  denotes the absolute position of vehicle  $i$  in the Laplace domain.

#### 2.4.1.2 Spacing policy

To achieve more efficient damping oscillations, we obtain the desired relative distances between vehicle  $i$  and its two predecessors using the CTH policy as follows:

$$d_{i,1}(t) = L + h\dot{x}_i(t), \quad d_{i,2}(t) = 2[L + h\dot{x}_i(t)] \quad (2.21)$$

where  $d_{1,i}(t)$  is the desired relative distance between vehicle  $i$  and vehicle  $i - 1$ , and  $d_{2,i}(t)$  is the desired relative distance between vehicle  $i$  and vehicle  $i - 2$ .  $L$  is the constant standstill distance (including vehicle length) between the two vehicles,  $\dot{x}_i(t)$  is the velocity of vehicle  $i$ , and  $h$  is the desired time headway.

The convex combination of spacing errors in Equation (2.22) is implemented in the feedback loop since the feedback controller processes spacing errors from both predecessors.

$$\begin{aligned} e_i(t) &= \alpha_{b,i}(\zeta_i)\{x_{i-1}(t) - x_{pr,i,1}(t)\} + \beta_{b,i}(\zeta_i)\{x_{i-2}(t) - x_{pr,i,2}(t)\} \\ &= \alpha_{b,i}(\zeta_i)\{[x_{i-1}(t) - x_i(t)] - d_{i,1}(t)\} \\ &\quad + \beta_{b,i}(\zeta_i)\{[x_{i-2}(t) - x_i(t)] - d_{i,2}(t)\} \end{aligned} \quad (2.22)$$

From Table 2.1, we note that  $\alpha_{b,i}(\zeta_i) + \beta_{b,i}(\zeta_i) = 1$  is always satisfied in the four controller statuses. Substituting Equation (2.21) into Equation (2.22), the weighted spacing error is

$$e_i(t) = \alpha_{b,i}(\zeta_i)x_{i-1}(t) + \beta_{b,i}(\zeta_i)x_{i-2}(t) - x_i(t) - (2 - \alpha_{b,i}(\zeta_i))(L + h\dot{x}_i(t)) \quad (2.23)$$

Taking the Laplace transformation of Equation (2.23), the spacing error can be expressed equivalently as:

$$E_i(s) = \alpha_{b,i}(\zeta_i)X_{i-1}(s) + \beta_{b,i}(\zeta_i)X_{i-2}(s) - H_i(s)X_i(s) \quad (2.24)$$

where  $H_i(s)$  is the CTH spacing policy in frequency domain, given by:

$$H_i(s) = 1 + (2 - \alpha_{b,i}(\zeta_i))hs \quad (2.25)$$

#### 2.4.1.3 Acceleration feedforward

From Fig. 2.5, the relationship between tracking error  $E_i(s)$  and the feedforward acceleration  $\ddot{X}_{i-1}(s) = s^2X_{i-1}(s)$  of the predecessor  $i - 1$  and feedforward acceleration  $\ddot{X}_{i-2}(s) = s^2X_{i-2}(s)$  of the predecessor  $i - 2$  in the Laplace domain is formulated as:

$$E_i(s) = \frac{\alpha_{b,i}(\zeta_i) - \alpha_{f,i}(\zeta_i)H_i(s)G_i(s)F_{1,i}(s)s^2}{1 + H_i(s)G_i(s)K_i(s)}X_{i-1}(s) + \frac{\beta_{b,i}(\zeta_i) - \beta_{f,i}(\zeta_i)H_i(s)G_i(s)F_{2,i}(s)s^2}{1 + H_i(s)G_i(s)K_i(s)}X_{i-2}(s) \quad (2.26)$$

To eliminate spacing error between adjacent vehicles, feedforward filters  $F_{1,i}(s)$  and  $F_{2,i}(s)$  are designed based on a zero-error condition (Naus et al., 2010). Hence, the numerators of the first and second terms on the right hand side in Equation (2.26) should be zero. Doing so, and substituting the  $\alpha_{b,i}(\zeta_i)$ ,  $\alpha_{f,i}(\zeta_i)$ ,  $\beta_{b,i}(\zeta_i)$  and  $\beta_{f,i}(\zeta_i)$  from Table 1 and the spacing policy  $H_i(s)$  from Equation (2.25) into it, we can derive the feedforward filters as:

$$F_{1,i}(s) = F_{2,i}(s) = (H_i(s)G_i(s)s^2)^{-1} = (H_i(s))^{-1} \quad (2.27)$$

#### 2.4.1.4 Control command

As illustrated in Fig. 2.5, our control command consists of a feedback term and two feedforward terms:

$$U_i(s) = U_{b,i}(s) + U_{f,i-1}(s) + U_{f,i-2}(s) \quad (2.28)$$

Recall that the feedback term  $U_{b,i}(s)$  uses spacing error to stabilize the closed-loop system while the feedforward terms  $U_{f,i-1}(s)$  and  $U_{f,i-2}(s)$  use acceleration rates from the two predecessors to minimize the spacing error.

The feedback term  $U_{b,i}(s)$  and the corresponding PD feedback controller are defined as:

$$U_{b,i}(s) = K_i(s)E_i(s) \quad (2.29)$$

$$K_i(s) = \omega_{K,i}(\omega_{K,i} + s) \quad (2.30)$$

where  $E_i(s)$  is the spacing error in the Laplace domain in Equation (2.24).  $\omega_{K,i}$  is the cut-off frequency of the PD controller. Cut-off frequency influences how aggressively vehicles

respond to rectify spacing errors; a larger cut-off frequency will make vehicle react faster. More importantly,  $\omega_{K,i}$  affects the value of string stability  $SS_{X,i}(j\omega, \xi_d(\xi))$  in Equation (2.6), and will be determined analytically in Section 2.4.2.

The feedforward terms  $U_{f,i-1}(s)$  and  $U_{f,i-2}(s)$  indicate that the acceleration rates of vehicles  $i - 1$  and  $i - 2$  are sent to  $i$ , respectively:

$$U_{f,i-1}(s) = \alpha_{f,i}(\zeta_i)F_{1,i}(s)s^2X_{i-1}(s) \quad (2.31)$$

$$U_{f,i-2}(s) = \beta_{f,i}(\zeta_i)F_{2,i}(s)s^2X_{i-2}(s) \quad (2.32)$$

Note that according to the two-predecessor-following scheme, the second vehicle in the platoon can receive acceleration information from only the leading vehicle, that is, the feedforward term of vehicle 1 includes only  $U_{f,0}(s)$ .

The overall control command is obtained by summing up Equations (2.29), (2.31) and (2.32). Through inverse Laplace transformation, the expression for the control command is:

$$u_i(t) = \omega_{K,i}^2 e_i(t) + \omega_{K,i} \dot{e}_i(t) + \alpha_{f,i}(\zeta_i)F_{1,i}(t)\ddot{x}_{i-1}(t) + \beta_{f,i}(\zeta_i)F_{2,i}(t)\ddot{x}_{i-2}(t) \quad (2.33)$$

The discretized version of (2.33) is used for operational deployment. We do not discuss it here due to space constraints.

## **2.4.2 Stability analysis and parameter determination**

Two parameters in the system impact platoon performance: time headway  $h$  and cut-off frequency  $\omega_{K,i}$ . We analyze these parameters to mitigate measurement noise and reduce platoon oscillations to aid string stability.

### **2.4.2.1 Measurement noise mitigation**

Measurement noise is a high-frequency noise generated from onboard sensors that produces inaccurate trajectory information, causing undesirable control inputs or platoon oscillations. Hence, mitigation of the measurement noise effect can improve control performance in terms of stability for individual vehicles in the platoon. Lemma 1 presents the characteristics of an upper bound for the product of  $h$  and  $\omega_{K,i}$  (i.e.,  $h\omega_{K,i}$ ) to mitigate measurement noise. Additionally, for measurements with greater noise contamination, the settings of weighting coefficients in CACC1 can be adjusted to lower values to improve the noise mitigation effect.

**Lemma 1:** By setting an upper bound for the product of  $h$  and  $\omega_{K,i}$  as:  $h\omega_{K,i} \leq W_{max}$ , the high-frequency measurement noise from the two predecessors is individually attenuated by at least  $W_{max}/[1 + W_{max}]$ .

**Proof:** For any following vehicle  $i$  in the platoon, the source of the measurement noise is mainly from the movement state detection of the two predecessors  $i - 1$  and  $i - 2$ . The measured position  $X_{i-1}$  ( $X_{i-2}$ ) of predecessor  $i - 1$  ( $i - 2$ ) consists of true value of position  $\bar{X}_{i-1}$  ( $\bar{X}_{i-2}$ ) and measurement noise  $N_{i-1}$  ( $N_{i-2}$ ):  $X_{i-1} = \bar{X}_{i-1} + N_{i-1}$  ( $X_{i-2} = \bar{X}_{i-2} + N_{i-2}$ ). From Fig. 2.5, the complementary sensitivity functions  $T_{1,i}$  ( $T_{2,i}$ ) can be used to describe the relationship between the processed position output  $X_{pr,i}(s)$  of vehicle  $i$  and measurement noise  $N_{i-1}$  ( $N_{i-2}$ ) included in position of predecessor  $i - 1$  ( $i - 2$ ).

$$\begin{aligned} T_{1,i}(s) &= X_{pr,i}(s)N_{i-1}(s)^{-1} \\ &= \alpha_{b,i}(\zeta_i)H_i(s)G_i(s)K_i(s)[1 \\ &\quad + H_i(s)G_i(s)K_i(s)]^{-1} \end{aligned} \quad (2.34)$$

$$\begin{aligned} T_{2,i}(s) &= X_{pr,i}(s)N_{i-2}(s)^{-1} \\ &= \beta_{b,i}(\zeta_i)H_i(s)G_i(s)K_i(s)[1 \\ &\quad + H_i(s)G_i(s)K_i(s)]^{-1} \end{aligned} \quad (2.35)$$

The magnitude of complementary sensitivity function  $T_{1,i}$  ( $T_{2,i}$ ) at a high-frequency represents the effect of measurement noise mitigation (a larger value of  $T_{1,i}$  or  $T_{2,i}$  indicates reduced mitigation of measurement noise). The key aspect of mitigating high-frequency measurement noise of  $X_{i-1}$  ( $X_{i-2}$ ) is to decrease the value of  $T_{1,i}$  ( $T_{2,i}$ ) in the high-frequency band. Substituting  $G_i(s)$ ,  $H_i(s)$ , and  $K_i(s)$  from Equations (2.20), (2.25), and (2.30) into Equations (2.34)-(2.35), we have:

$$\begin{aligned} &\lim_{s \rightarrow \infty} T_{1,i}(s) \\ &= \lim_{s \rightarrow \infty} \alpha_{b,i}(\zeta_i) \frac{h\omega_{K,i}s^2 + (h\omega_{K,i}^2 + \omega_{K,i})s + \omega_{K,i}^2}{(1 + h\omega_{K,i})s^2 + (h\omega_{K,i}^2 + \omega_{K,i})s + \omega_{K,i}^2} \\ &= \alpha_{b,i}(\zeta_i) \frac{h\omega_{K,i}}{1 + h\omega_{K,i}} \end{aligned} \quad (2.36)$$

$$\begin{aligned} &\lim_{s \rightarrow \infty} T_{2,i}(s) \\ &= \lim_{s \rightarrow \infty} \beta_{b,i}(\zeta_i) \frac{h\omega_{K,i}s^2 + (h\omega_{K,i}^2 + \omega_{K,i})s + \omega_{K,i}^2}{(1 + h\omega_{K,i})s^2 + (h\omega_{K,i}^2 + \omega_{K,i})s + \omega_{K,i}^2} \\ &= \beta_{b,i}(\zeta_i) \frac{h\omega_{K,i}}{1 + h\omega_{K,i}} \end{aligned} \quad (2.37)$$

From Table 2.1, we have  $\alpha_{b,i}(\zeta_i) \leq 1$  and  $\beta_{b,i}(\zeta_i) \leq 1$ . By setting an upper bound for the product of  $h\omega_{K,i}$  as:  $h\omega_{K,i} \leq W_{max}$ , the upper bounds of  $\lim_{s \rightarrow \infty} T_{1,i}(s)$  and  $\lim_{s \rightarrow \infty} T_{2,i}(s)$  can be determined as  $\lim_{s \rightarrow \infty} T_{1,i}(s) \leq h\omega_{K,i}/[1 + h\omega_{K,i}] \leq W_{max}/[1 + W_{max}]$  and  $\lim_{s \rightarrow \infty} T_{2,i}(s) \leq h\omega_{K,i}/[1 + h\omega_{K,i}] \leq W_{max}/[1 + W_{max}]$ , respectively, which indicates that the high-frequency measurement noise from two predecessors is individually attenuated by at least  $W_{max}/[1 + W_{max}]$ . This completes the proof for Lemma 1.

For operational deployment,  $W_{max}$  depends on the measurement noise mitigation needs of the specific system. Its value is determined through trial-and-error. In the study experiments, we aim to attenuate the measurement noise by a factor of at least 2/3. By calculating  $W_{max}/[1 + W_{max}] = 2/3$ , the upper bound of  $h_d\omega_{K,i}$  is set as  $W_{max} = 2$ .

Remark 1: In CACC1, the values of  $\alpha_{b,i}(\zeta_i)$  and  $\beta_{b,i}(\zeta_i)$  can be adjusted based on the signal-to-noise ratio (SNR)<sup>3</sup> of position measurement  $X_{i-1}$  and  $X_{i-2}$ :  $\alpha_{b,i}(\zeta_i)/\beta_{b,i}(\zeta_i) = \text{SNR2}/\text{SNR1}$ , where SNR1 corresponds to measurement of  $X_{i-1}$  and SNR2 corresponds to

<sup>3</sup>Signal-to-noise ratio (SNR) is defined as the ratio of the power of a signal divided by the power of measurement noise, which can also be expressed as the ratio between variance of measured signal and measurement noise:  $\text{SNR} = P_{signal}/P_{noise} = \sigma_{signal}^2/\sigma_{noise}^2$ ; a larger SNR indicates a weaker noise effect on the measurement information.

measurement of  $X_{i-2}$ . The adjustment of weighting coefficients can improve the effect of noise mitigation by putting lesser weight on measurements with smaller SNR.

#### 2.4.2.2 String stability analysis

The string stability transfer function is specified as a measure of signal amplification. The platoon head-to-tail string stability is analyzed to ensure that traffic oscillations are effectively damped when they reach the platoon tail. A homogeneous string stability criterion is used as we assume a homogeneous vehicle platoon. The transfer function is the ratio of the trajectory oscillations in the Laplace domain of the  $i$ th vehicle to that of the leading vehicle:

$$SS_{X,i}(s) = X_i(s)/X_0(s) \quad (2.38)$$

To ensure head-to-tail string stability, with  $s = j\omega$ , we have the string stability condition:

$$\|SS_{X,i}(j\omega)\|_{\infty} = \|X_i(j\omega)/X_0(j\omega)\|_{\infty} \leq 1 \quad (2.39)$$

where  $j = \sqrt{-1}$ , and the string stability condition based on  $\infty$ -norm can be satisfied by the requirement of  $|SS_{X,i}(j\omega)| \leq 1$  for all  $\omega$ . For simplification, in the following analysis, we use  $SS_{X,i}$ ,  $X_i$ ,  $G_i$ ,  $H_i$ ,  $K_i$ ,  $F_{1,i}$ , and  $F_{2,i}$  to denote  $SS_{X,i}(s)$ ,  $X_i(s)$ ,  $G_i(s)$ ,  $H_i(s)$ ,  $K_i(s)$ ,  $F_{1,i}(s)$ , and  $F_{2,i}(s)$ , respectively.

From Equations (2.1), (2.20), and (2.25)-(2.32), the transfer functions of string stability of all vehicles in platoon are described as:

$$\overline{SS} = T(\zeta)S \quad (2.40)$$

where  $\overline{SS} = [SS_{x,0} \ SS_{x,1} \ SS_{x,2} \ SS_{x,3} \ \dots \ SS_{x,n}]^T$ ,  $S = [1 \ 0 \ 0 \ 0 \ \dots \ 0]^T$ ,  $SS_{x,0} = 1$  and  $SS_{x,i} = X_i/X_0, i \geq 1$ .

$$T(\zeta) = \begin{bmatrix} 1 & 0 & 0 & 0 & \dots & 0 \\ \mathcal{G}_{1,1} & -1 & 0 & 0 & \ddots & \vdots \\ \mathcal{G}_{2,2} & \mathcal{G}_{2,1} & -1 & 0 & \ddots & 0 \\ 0 & \mathcal{G}_{3,2} & \mathcal{G}_{3,1} & -1 & \ddots & 0 \\ \vdots & \ddots & \ddots & \ddots & \ddots & 0 \\ 0 & \dots & \dots & \mathcal{G}_{n,2} & \mathcal{G}_{n,1} & -1 \end{bmatrix}^{-1}$$

$$\mathcal{G}_{i,1} = \alpha_{f,i}(\zeta_i)\Lambda_{f,i-1} + \alpha_{b,i}(\zeta_i)\Lambda_{b,i-1} \quad (2.41)$$

$$\mathcal{G}_{i,2} = \beta_{f,i}(\zeta_i)\Lambda_{f,i-2} + \beta_{b,i}(\zeta_i)\Lambda_{b,i-2} \quad (2.42)$$

where  $\Lambda_{f,i-2} = \frac{G_i F_{2,i} s^2}{1+G_i K_i H_i}$  is the transfer function between the position of vehicles  $i-2$  and  $i$  with respect to the feedforward term  $U_{f,i-2}(s)$ ;  $\Lambda_{f,i-1} = \frac{G_i F_{1,i} s^2}{1+G_i K_i H_i}$  is the transfer function between vehicles  $i-1$  and  $i$  with respect to feedforward term  $U_{f,i-1}(s)$ ;  $\Lambda_{b,i-1} = \Lambda_{b,i-2} = \frac{G_i K_i}{1+G_i K_i H_i}$  is the transfer function between the position of vehicles  $i-1$  or  $i-2$  and  $i$  with respect to the feedback term  $U_{b,i}(s)$ .

Based on the four communication statuses described in Fig. 2.4, we analyze the corresponding feasible regions for the time headway  $h$  and cut-off frequency  $\omega_{K,i}$  to ensure string stability,

using Proposition 1 and Lemma 2.

Proposition 1: If  $\sigma \geq 0$ , a first order transfer function:  $q(j\omega) = \frac{1}{1+j\omega\sigma}$  satisfies the string stability in Equation (2.39).

Proof: Since  $|q(j\omega)| = \frac{1}{\sqrt{1+\sigma^2\omega^2}}$  and phase angle  $\angle q(j\omega) = -\arctan(\sigma\omega)$ , the magnitude of  $q(j\omega)$  will always be lesser than or equal to one. However, when  $\sigma < 0$ , the phase angle of  $q(j\omega)$  is positive, which indicates that the system corresponding to the first order transfer function is not practically deployable. Hence,  $\sigma \geq 0$  is essential and necessary to guarantee string stability. This completes the proof for Proposition 1.

Lemma 2: The proposed adaptive PD controller in Section 2.4.1 can ensure the string stability of a platoon if the time headway  $h$  and controller cut-off frequency  $\omega_{K,i}$  satisfy the following conditions:

For the CACC cases, the time headway  $h$  satisfies  $h > 0$ .

For the ACC case, a lower bound for  $h\omega_{K,i}$  satisfies  $h\omega_{K,i} \geq \sqrt{2}$ .

Proof: The string stability can be analyzed by performing an arithmetic operation on the transfer function of string stability, by checking if the ratio of trajectory oscillations in the frequency domain of the  $i$ th vehicle and the leading vehicle 0 is lesser than or equal to 1.

The CACC cases:

From Equations (2.40)-(2.42), the transfer functions of string stability for the CACC cases and the ACC case are:

$$\begin{aligned} SS_{X,i} = & (\alpha_{f,i}(\zeta_i)\Lambda_{f,i-1} + \alpha_{b,i}(\zeta_i)\Lambda_{b,i-1})\frac{X_{i-1}}{X_0} \\ & + (\beta_{f,i}(\zeta_i)\Lambda_{f,i-2} + \beta_{b,i}(\zeta_i)\Lambda_{b,i-2})\frac{X_{i-2}}{X_0} \end{aligned} \quad (2.43)$$

Note that to directly analyze string stability transfer function is complex as it is a high-order transfer function. To address this problem, we consider only the worst case in Equation (2.43) where the values of both  $X_{i-2}/X_0$  and  $X_{i-1}/X_0$  are equal to one (implying head-to-tail marginally string stability, which means the traffic oscillations is neither amplified nor damped when it propagates in the traffic flow). This enables the determination of a more conservative, feasible region of the two parameters to ensure string stability. From Table 2.1, when  $X_{i-2}/X_0 = X_{i-1}/X_0 = 1$ , Equation (2.43) becomes:

$$SS_{X,i} = \begin{cases} (\alpha G_i K_i + \beta G_i K_i + \alpha G_i F_{1,i} s^2 + \beta G_i F_{2,i} s^2)(1 + G_i K_i H_i)^{-1}, & CACC1 \\ (G_i K_i + G_i F_{1,i} s^2)(1 + G_i K_i H_i)^{-1}, & CACC2 \text{ and } CACC3 \end{cases} \quad (2.44)$$

Substituting for  $H_i$  from Equation (2.27), Equation (2.44) can be simplified to:

$$SS_{X,i} = \begin{cases} [1 + (2 - \alpha)hs]^{-1}, & CACC1 \\ (1 + hs)^{-1}, & CACC2 \text{ and } CACC3 \end{cases} \quad (2.45)$$

To guarantee the string stability condition in Equation (2.39), the magnitude of  $SS_{X,i}$  should not be greater than one. Correspondingly, for CACC1, according to proposition 1, the feasible

region is:  $h > 0$  since  $1 \leq 2 - \alpha < 2$  and time headway is positive; for CACC2 and CACC3, similarly, the feasible region is:  $h > 0$ .

The ACC Case:

Under the ACC schematic, we have  $\alpha_{f,i}(\zeta_i) = \beta_{f,i}(\zeta_i) = \beta_{b,i}(\zeta_i) = 0$ , and  $\alpha_{b,i}(\zeta_i) = 1$  from Table 2.1. The transfer function of string stability from Equation (2.43) will degrade to:

$$\begin{aligned} SS_{X,i} &= \frac{X_i}{X_0} = \Lambda_{b,i-1} \frac{X_{i-1}}{X_0} = \frac{G_i K_i}{1 + G_i K_i H_i} \\ &= \frac{\omega_{K,i} s + \omega_{K,i}^2}{(1 + h\omega_{K,i})s^2 + \omega_{K,i}(1 + h\omega_{K,i})s + \omega_{K,i}^2} \end{aligned} \quad (2.46)$$

Consequently, by substituting  $s = j\omega$  in Equation (2.49), the string stability condition becomes:

$$|SS_{X,i}| = \left| \frac{j\omega_{K,i}\omega + \omega_{K,i}^2}{(\omega_{K,i} - (1 + h\omega_{K,i})\omega^2) + j\omega_{K,i}(1 + h\omega_{K,i})\omega} \right| \leq 1 \quad (2.47)$$

Solving inequality (4.50) leads to:

$$\omega_{K,i}^2 (2 - h^2 \omega_{K,i}^2) (1 + h\omega_{K,i})^{-2} \leq \omega^2 \quad (2.48)$$

Since  $\min_{\omega \geq 0} \omega^2 = 0$ , the inequality (2.48) can be solved by letting  $\omega^2 = 0$ . Then, the string stability region of the controller cut-off frequency and headway time is:

$$h\omega_{K,i} \geq \sqrt{2} \quad (2.49)$$

Remark 2: The decision-making process can be summarized as: (i)  $h\omega_{K,i}$  has a specific upper bound for mitigating measurement noise effects;  $h\omega_{K,i} \leq W_{max} = 2$ ; (ii) string stability requires positive time headway:  $h > 0$  for the CACC1, CACC2 and CACC3 cases, and  $h\omega_{K,i} \geq \sqrt{2}$  for the ACC case; (iii) ensuring local stability (individual vehicle stability) requires positive time headway and controller cut-off frequency; and (iv) increasing either time headway or controller cut-off frequency will improve string stability performance though it deteriorates noise mitigation performance; hence, proper parameter selection is essential.

Remark 3: The additional parameter settings are: (i) the desired time headways  $h$  in all controllers should be identical to preclude traffic oscillations that are generated through controller switching; and (ii) to simplify the problem, this study considers a homogeneous platoon, implying that all the vehicles have the same adaptive PD controller.

## 2.5 Algorithm to solve OPT-II

The section describes the algorithm to solve the IFT optimization model OPT-II, formulated in Section 2.4.2. The objective function in Equation (2.17) is complex because: (i) the decision variable  $\xi$  is a binary vector, which makes it a discrete integer optimization problem; (ii) the transfer function  $SS_{X,i}^2(j\omega, \xi_d)$  depends on the controller used in the degeneration scenario  $\xi_d$ , which implies different speed oscillation energies for the platoon under different degeneration scenarios; and (iii) the objective function requires the trajectory oscillations of the ambient traffic

conditions in the frequency domain  $X(j\omega)$  in the integrand to determine the expected speed oscillation energies. Together, these factors make it difficult to obtain a closed-form solution, entailing the need for a numerical solution.

To solve OPT-II numerically, the primary concern is computational complexity arising mainly due to platoon size. For a platoon with  $N + 1$  vehicles, there are  $2^{N+1}$  candidate IFTs. For an IFT with  $b$  vehicles that activate “send” functionalities, there are  $2^b$  degeneration scenarios. For each degeneration scenario, the computation of the control performance requires the sum of the speed oscillation energies in the frequency domain for each vehicle. Hence, the computational complexity can increase significantly as the platoon size increases, leading to the need for computation efficiency. Though the optimal IFT is not updated frequently, it should be determined as quickly as possible so that the platoon can adjust the IFT to the optimal one before ambient traffic conditions change significantly. To enhance computation efficiency, we first analyze the activation statuses of the “send” functionalities of the leading and the last vehicles in the platoon as a pre-processing step, which can preclude the consideration of a subset of candidate IFTs. Then, a two-step algorithm is proposed to efficiently search for the optimal IFT among the remaining candidate IFTs.

### **2.5.1 Activation status of “send” functionalities of the leading and last vehicles in the platoon**

The “send” functionality of the communication device for the last (following) vehicle should always be deactivated as it only needs to receive information to maintain control performance. Deactivating the “send” functionality of this vehicle can decrease the probability of communication collision and improve the reliability of the V2V communication.

Next, we investigate the activation status of the “send” functionality of the leading vehicle. We first compare the control performance of CACCs 1, 2, 3 and ACC using Proposition 2, and then prove that the leading vehicle always needs to activate its “send” functionality, using Lemma 3 and Theorem 1.

From Equation (2.43), we note that the transfer function of string stability  $SS_{X,i}$  of vehicle  $i$  is a function of its communication status  $\zeta_i$ . In this subsection, we denote it more specifically as  $SS_{X,i,\zeta_i}$  to reflect the transfer function of string stability under different controllers (CACCs 1, 2, 3, and ACC, for  $\zeta_i \in \{1, 2, 3, 4\}$ , respectively).

Proposition 2: Based on the four possible communication statuses in Fig. 2.4, the magnitudes of transfer functions of string stability satisfy:  $|SS_{X,i,1}| < |SS_{X,i,2}| < |SS_{X,i,4}|$ ,  $|SS_{X,i,1}| < |SS_{X,i,3}| < |SS_{X,i,4}|$ , indicating that CACCs can damp traffic oscillations better than ACC.

Proof: To compare the magnitudes of string stability transfer functions under the CACCs and the ACC, the cut-off frequency  $\omega_{c,\zeta_i}$ ,  $\zeta_i \in \{1, 2, 3, 4\}$  is analyzed. The cut-off frequency  $\omega_{c,\zeta_i}$  is a corner frequency beyond which the logarithmic value of  $X_i/X_0$  should be smaller than  $-3.01\text{dB}$  (Palm, 2005), which indicates that the oscillation energy will be effectively damped. A smaller cut-off frequency  $\omega_{c,\zeta_i}$  implies better string stability performance. The cut-off frequency  $\omega_{c,\zeta_i}$  of transfer function  $SS_{X,i,\zeta_i}(j\omega)$  can be calculated by solving Equation (2.50) as follows:

$$20\log|SS_{X,i,\zeta_i}(j\omega_{c,\zeta_i})| = -3.01\text{dB} \quad (2.50)$$

From Equations (2.44) and (2.45), the string stability transfer function for CACC1 is:

$$\begin{aligned} SS_{X,i,1}(j\omega_{c,1}) &= (\alpha + \beta)(1 + G_i K_i H_i)[H_i(1 + G_i K_i H_i)]^{-1} = H_i^{-1} \\ &= [1 + j(2 - \alpha)h\omega_{c,1}]^{-1} \end{aligned} \quad (2.51)$$

By substituting Equation (2.51) into Equation (2.50) and solving it, we obtain the corresponding cut-off frequency in Equation (2.52), where  $C = 10^{\frac{-3.01}{10}}$ :

$$\omega_{c,1} = \sqrt{(1 - C)[(2 - \alpha)^2 C h^2]^{-1}} \quad (2.52)$$

From Equations (2.44) and (2.45), the transfer functions for CACC2 and CACC3 are:

$$\begin{aligned} SS_{X,i,2}(j\omega_{c,2}) &= SS_{X,i,3}(j\omega_{c,3}) = (G_i K_i + G_i F_{1,i} s^2)(1 + G_i K_i H_i)^{-1} \\ &= H_i^{-1} = (1 + j\omega_{c,2} h)^{-1} \end{aligned} \quad (2.53)$$

By substituting Equation (2.53) into Equation (2.50) and solving it, we obtain the corresponding cut-off frequency:

$$\omega_{c,2} = \omega_{c,3} = \sqrt{(1 - C)[C h^2]^{-1}} \quad (2.54)$$

From Table 2.1, we have  $0 < \alpha < 1$ . By comparing Equations (2.52) and (2.54), we obtain that  $\omega_{c,1} < \omega_{c,2} = \omega_{c,3}$ . Then, we only need to compare  $\omega_{c,2}$  or  $\omega_{c,3}$  with  $\omega_{c,4}$ . From Equation (2.46), the transfer function of ACC is:

$$\begin{aligned} SS_{X,i,4}(j\omega_{c,4}) &= \frac{G_i K_i}{1 + G_i K_i H_i} \\ &= \frac{j\omega_{K,i}\omega_{c,4} + \omega_{K,i}^2}{j(\omega_{K,i}^2 + h\omega_{K,i})\omega_{c,4} + \omega_{K,i}^2 - (1 + h\omega_{K,i})\omega_{c,4}^2} \end{aligned} \quad (2.55)$$

By substituting Equation (2.55) into Equation (2.50) and solving it, we obtain the corresponding cut-off frequency:

$$\omega_{c,4} = \sqrt{\left[ B + \sqrt{B^2 - 4C(1 + h\omega_{K,i})^2 (\omega_{K,i}^4 (C - 1))} \right] \left[ 2C(1 + h\omega_{K,i})^2 \right]^{-1}} \quad (2.56)$$

where  $B = C(\omega_{K,i} + h\omega_{K,i}^2)^2 - 2C\omega_{K,i}^2(1 + h\omega_{K,i}) - \omega_{K,i}^2$ .

From Remark 2, the values of  $h\omega_{K,i}$  for controller design lie within the range  $[\sqrt{2}, 2]$ . From Equations (2.54) and (2.56), the necessary condition for the inequality  $\omega_{c,4} > \omega_{c,2}$  is the lower bound of  $h\omega_{K,i}$ :  $h\omega_{K,i} > (1 + \sqrt{3})/2$ . As the range of the controller parameters is included within the lower bound that is necessary for  $\omega_{c,4} > \omega_{c,2}$ , we can conclude that ACC and CACC2 satisfy the condition  $\omega_{c,4} > \omega_{c,2}$ .

Based on the analysis above, we note that the cut-off frequencies of string stability transfer functions under the CACC cases and the ACC case satisfy  $\omega_{c,1} < \omega_{c,2} = \omega_{c,3} < \omega_{c,4}$ . Hence, the magnitudes of the string stability transfer functions satisfy:  $|SS_{X,i,1}| < |SS_{X,i,2}| < |SS_{X,i,4}|$ ,  $|SS_{X,i,1}| < |SS_{X,i,3}| < |SS_{X,i,4}|$ .

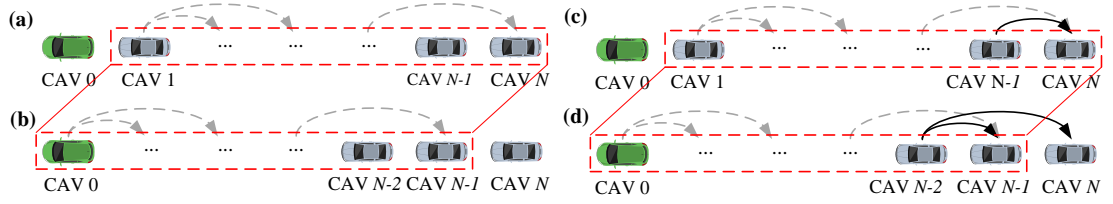


Figure 2.6. Illustration of the deactivated or activated status of the “send” functionality of CAV 0.

Next, the “send” status of the leading vehicle is analyzed. Two IFTs are illustrated in Figs. 2.6(a) and (c). In both scenarios, the “send” functionality of the leading vehicle and the last vehicle are deactivated. In Fig. 2.6(a), vehicle  $N - 1$  has its communication device deactivated, while in Fig. 2.6(c) vehicle  $N - 1$  broadcasts messages. In Fig. 2.6(b) (Fig. 2.6(d)), the “send” activation status of vehicle  $i$  (for  $i = 0, 1, \dots, N - 1$ ) is the same as for vehicle  $i + 1$  in Fig. 2.6(a) (Fig. 2.6(c)). The “send” functionality is deactivated for the last vehicles in Fig. 2.6(b) and Fig. 2.6(d). All feasible IFT candidates can be categorized into these four general cases.

Lemma 3: In Fig. 2.6, the expected platoon speed oscillation energy of the IFT in Fig. 2.6(b) is always lower than that in Fig. 2.6(a). Similarly, the speed oscillation energy of the IFT in Fig. 2.6(d) is lower than that in Fig. 2.6(c).

Proof: Denote the IFTs in Figs. 2.6(a) and 2.6(b) as  $\xi^{(a)}$  and  $\xi^{(b)}$ , and degeneration scenarios of  $\xi^{(a)}$ ,  $\xi^{(b)}$  as  $\xi_d^{(a)}$ ,  $\xi_d^{(b)}$ . For each  $\xi_d^{(a)}$ , there is a  $\xi_d^{(b)}$  whose IFT from vehicle 0 to vehicle  $N - 1$  is the same as the IFT of  $\xi_d^{(a)}$  from vehicle 1 to vehicle  $N$ . Hence, the probability of  $\xi_d^{(a)}$ ,  $P_d(\xi_d^{(a)})$ , is equal to the probability of  $\xi_d^{(b)}$ ,  $P_d(\xi_d^{(b)})$  (i.e.,  $P_d(\xi_d^{(a)}) = P_d(\xi_d^{(b)})$ ). Then, we only need to compare the control performance of  $\xi_d^{(a)}$  and  $\xi_d^{(b)}$ . Note that vehicle 1 in Fig. 2.6(a) and vehicle  $N$  in Fig. 2.6(b) operate under ACC. To simplify notation, we use  $SS_{X,i,\zeta_i}(\xi_d^{(a)})$  and  $X_0$  to denote  $SS_{X,i,\zeta_i}(j\omega, \xi_d^{(a)})$  and  $X_0(j\omega)$ , respectively. We denote  $SS'_{X,i,\zeta_i}(\xi_d^{(a)}) = X_i/X_1$ ; then, according to Equations (2.11) and (2.38), we have:

$$\begin{aligned}
 E_d(\xi_d^{(a)}) &= 4\pi^2 \int_0^{+\infty} \left( \sum_{i=0}^N SS_{X,i,\zeta_i}^2(\xi_d^{(a)}) \right) \omega^2 X_0^2 d\omega \\
 &= 4\pi^2 \int_0^{+\infty} \left( 1 \right. \\
 &\quad \left. + SS_{X,1,4}^2 \sum_{i=1}^N SS'_{X,i,\zeta_i}(\xi_d^{(a)}) \right) \omega^2 X_0^2 d\omega
 \end{aligned} \tag{2.57}$$

$$\begin{aligned}
E_d(\xi_d^{(b)}) &= 4\pi^2 \sum_{i=0}^N \int_0^{+\infty} \omega^2 SS_{X,i,\zeta_i}^2(\xi_d^{(b)}) X_0^2 d\omega \\
&= 4\pi^2 \int_0^{+\infty} \left( \sum_{i=0}^{N-1} SS_{X,i,\zeta_i}^2(\xi_d^{(b)}) \right. \\
&\quad \left. + SS_{X,n,4}^2(\xi_d^{(b)}) \right) \omega^2 X_0^2 d\omega
\end{aligned} \tag{2.58}$$

$$\begin{aligned}
\frac{E_d(\xi_d^{(b)}) - E_d(\xi_d^{(a)})}{4\pi^2} &= \int_0^{+\infty} \left( \sum_{i=0}^{N-1} SS_{X,i,\zeta_i}^2(\xi_d^{(b)}) + SS_{X,n,4}^2(\xi_d^{(b)}) - 1 \right. \\
&\quad \left. - SS_{X,1,4}^2 \sum_{i=1}^N SS'_{X,i,\zeta_i}{}^2(\xi_d^{(a)}) \right) \omega^2 X_0^2 d\omega
\end{aligned} \tag{2.59}$$

Since all vehicles have the same adaptive PD controller (Remark 2), we have  $SS_{X,1,4}^2 = \Lambda_{b,0}^2 = \Lambda_{b,i-1}^2$  for any  $i = 2, \dots, N$ , where  $\Lambda_{b,i-1}^2$  is as shown in Equation (2.46). The receiver state  $\zeta_i$  of vehicle  $i$  (for  $i = 1, 2, \dots, N$ ) in Fig. 2.6(a) is equal to the receiver state  $\zeta_{i-1}$  of vehicle  $i-1$  in Fig. 2.6(b), which indicates that  $SS'_{X,i,\zeta_i}{}^2(\xi_d^{(a)}) = SS_{X,i-1,\zeta_{i-1}}^2(\xi_d^{(b)})$ . From Proposition 2 and Equations (2.38) and (2.46), for  $i > 3$ , we have  $SS_{X,i-1,\zeta_i}^2(\xi_d^{(b)}) \leq SS_{X,i-2,\zeta_{i-2}}^2(\xi_d^{(b)}) \Lambda_{b,i-2}^2 \leq SS_{X,i-3,\zeta_{i-3}}^2(\xi_d^{(b)}) \Lambda_{b,i-2}^2 \Lambda_{b,i-3}^2 \leq \dots < SS_{X,1,\zeta_1}^2(\xi_d^{(b)}) \prod_{i'=2}^i \Lambda_{b,i'-1}^2 < \prod_{i'=1}^i \Lambda_{b,i'-1}^2 = \Lambda_{b,0}^{2i}$ . For  $i = 1, 2$ , we have  $SS_{X,i-1,\zeta_i}^2(\xi_d^{(b)}) < \prod_{i'=1}^i \Lambda_{b,i'-1}^2 = \Lambda_{b,0}^{2i}$ . These inequalities indicate that the string stability performance of vehicle  $i$  under degeneration scenario  $\xi_d^{(b)}$  is always better than the performance when all its predecessors deactivate their “send” functionalities. Accordingly, we have:

$$\begin{aligned}
&\sum_{i=0}^{N-1} SS_{X,i,\zeta_i}^2(\xi_d^{(b)}) + SS_{X,n,4}^2(\xi_d^{(b)}) - 1 - SS_{X,1,4}^2 \sum_{i=1}^N SS'_{X,i,\zeta_i}{}^2(\xi_d^{(a)}) \\
&< (1 - \Lambda_{b,0}^2) \left( \sum_{i=1}^{N-1} \Lambda_{b,0}^{2i} \right) + \Lambda_{b,0}^{2N} - 1 \\
&= (1 - \Lambda_{b,0}^2) \frac{1 - \Lambda_{b,0}^{2N}}{1 - \Lambda_{b,0}^2} + \Lambda_{b,0}^{2N} - 1 = 0
\end{aligned} \tag{2.60}$$

By substituting inequality (2.60) into Equation (2.59), we have  $E_d(\xi_d^{(b)}) < E_d(\xi_d^{(a)})$ , which indicates that each degeneration scenario  $\xi_d^{(b)}$  of IFT  $\xi^{(b)}$  has lower oscillation energy than the corresponding degeneration scenario  $\xi_d^{(a)}$  of IFT  $\xi^{(a)}$ . Since the corresponding probabilities

of each degeneration scenario pair are identical,  $\xi^{(b)}$  always outperforms  $\xi^{(a)}$ . Similarly, we can prove that the IFT in Fig. 2.6(d) outperforms that in Fig. 2.6(c).

**Theorem 1:** In the optimal IFT, the “send” functionality of the leading vehicle is always activated.

**Proof:** If the “send” functionality of leading vehicle is not activated, then from Lemma 3 we can always change the IFT from (a) to (b) or from (c) to (d) to find a better one until the leading vehicle activates the “send” functionality.

### 2.5.2 Two- step algorithm for solving OPT-II

Different IFTs may have several identical degeneration scenarios. For example, IFT  $[0, 0, 1, 0, 0]$  in Fig. 2.2(a) is a degeneration scenario of IFT  $[1, 0, 1, 0, 0]$  illustrated in Fig. 2.2(a). However, it is also a degeneration scenario of IFT  $[1, 1, 1, 0, 0]$  when both vehicles 0 and 1 fail to send messages at the same time. According to Theorem 1 in Section 2.5.1, the leading vehicle always needs to activate its “send” functionality and the last vehicle needs to deactivate it, a fully-activated IFT except for the last vehicle ( $\xi = [1, \dots, 1, 0]$ ) includes all possible degeneration scenarios for other IFTs. Therefore, we only need to investigate the string stability performance of the degeneration scenarios for that IFT. For the other IFTs, we will just use the string stability performance of the relevant degeneration scenarios calculated for the fully-activated IFT.

Motivated by above observation, we propose a two-step algorithm. The first step calculates the string stability performance of degeneration scenarios for the fully-activated IFT to construct a control performance table according to Sections 3.1 and 4. Then, in the second step, for each  $\xi \in \Omega$ , we traverse all possible degeneration scenarios  $\xi_d \in \Omega_d(\xi)$ , and add the corresponding control performances from the table generated in the first step with a weight  $P_d(\xi_d(\xi))$  formulated from the contention model in Section 2.3.2 to obtain the expected string stability of IFT  $\xi$ . The pseudo code of the two-step algorithm is shown as the following steps:

<p>Step 1</p> <p>input ambient traffic oscillations in the frequency domain <math>X(j\omega)</math>, average density <math>\bar{k}</math>, and platoon size <math>N + 1</math>;</p> <p>set <math>\xi = [1, \dots, 1, 0] \in \mathbb{R}^{N+1}</math>, update <math>\Omega_d(\xi)</math></p> <p>for any <math>\xi_d(\xi) \in \Omega_d(\xi)</math></p> <p>Determine its speed oscillation energies <math>E_d(\xi_d(\xi))</math> using Equation (2.11).</p> <p>end</p> <p>output <math>\hat{\xi}_d = \xi_d(\xi)</math> and corresponding speed oscillation energies <math>\hat{E}_d(\hat{\xi}_d) = E_d(\xi_d(\xi))</math> for any <math>\xi_d(\xi) \in \Omega_d(\xi)</math></p>
<p>Step 2</p> <p>input <math>E(x)</math></p> <p>set the set of candidate IFTs <math>\Omega = \{[1, \eta_1, \dots, \eta_{N-1}, 0]   \eta_i \in \{0, 1\} \text{ for } i = 1, \dots, N - 1\}</math></p> <p>initialize the optimal expected speed oscillation energies <math>E^* \leftarrow +\infty</math></p> <p>for any <math>\xi \in \Omega</math></p>

Update  $\Omega_d(\xi)$   
 for any  $\xi_a(\xi) \in \Omega_d(\xi)$   
 Determine the  $P_d(\xi_a(\xi))$  using Equation (2.16).  
 Find  $\hat{\xi}_d = \xi_a(\xi)$ , then  $E_d(\xi_a(\xi)) \leftarrow \hat{E}_d(\hat{\xi}_d)$ .  
 end  
 Determine the expected speed oscillation energies  $E(\xi)$  under the IFT  $\xi$  using Equation (2.2).  
 if  $E(\xi) < E^*$   
 Update  $E^* \leftarrow E(\xi)$  and the optimal IFT  $\xi^* \leftarrow \xi$   
 end  
 end  
 output  $\xi^*$

## 2.6 Numerical experiments

### 2.6.1 Experiment design and parameter setting

Numerical experiments are conducted to analyze the CACC-OIFT strategy. First, the performance of V2V communication and the computational efficiency of the algorithm are investigated. Next, the performance of CACC-OIFT is analyzed. The optimization procedure and the performance comparison simulations are conducted on a C++ platform that integrates network simulator NS-3 to emulate the V2V communication process.

The experiment setup consists of a  $N + 1$  CAV platoon with one leading vehicle ( $i = 0$ ) and  $N$  following vehicles ( $i = 1, \dots, N$ , and  $N = 11, \dots, 15$ ). The movement of the leading vehicle is predetermined according to NGSIM field data (US DOT, 2007), which contains a 240-second vehicle trajectory on eastbound I-80 in the San Francisco Bay area at Emeryville, California. The frequency domain trajectory oscillations  $X(j\omega)$  and average density of ambient traffic flow  $\bar{k}$  are provided to the optimization model. The first following vehicle ( $i = 1$ ) receives information only from one preceding vehicle ( $i = 0$ ); so, the controller will switch between CACC2 and ACC if the IFT degenerates. For the other vehicles ( $i = 2, \dots, N$ ), the controller can switch among the four controllers (i.e., CACC 1, 2, 3, and ACC). The desired time headways in all controllers are set to  $h = 1s$ . The cut-off frequency  $\omega_{K,i}$  is set as 0.8, 0.8, 0.9 and 1.45 for CACC 1, 2, 3, and ACC, respectively. The parameters  $\alpha$  and  $\beta$  are set as 0.7 and 0.3. The control time interval is set as 0.1s. The network parameters are listed in Table 2.2. In addition, since the measurement noise generated from onboard sensors and vehicle movements cannot be neglected in CACC/ACC implementation, we include the measurement noise in the measured position and speed of predecessors. The position measurement noise and speed measurement noise are both Gaussian white noise. As illustrated in (Moon et.al., 2005), the standard deviation (SD) of the speed measurement noise is set as:  $\sigma_v = 0.1m/s$ ; and according to (Kim, 2012), the SD of position measurement noise can be calculated as:

$$\sigma_x = \frac{T\sigma_v}{\sqrt{2}} = 0.1 \times \frac{0.1}{\sqrt{2}} = 0.007m.$$

Table 2.2. Network parameters.

Parameter	Value	Parameter	Value	Parameter	Value
Communication range	0.2 km	Information generation rate	10 Hz	Data rate	3 Mbps
Packet size	500 B	Contention window size	8	Slot time	16 $\mu$ s

The performance of CACC-OIFT is investigated through three numerical experiments. The first experiment compares the proposed CACC-OIFT with two other control strategies. The three strategies are: (i) CACC-OIFT, which includes the IFT optimization from Section 2.3 and the adaptive PD controller from Section 2.4, (ii) CACC-DIFT, which includes the adaptive PD controller from Section 2.4 with a fully-activated IFT, and (iii) CACC with a fixed IFT (CACC-FIFT), which includes the CACC and ACC schemes developed in Naus et.al. (2010). We also analyze another CACC controller with a fixed IFT (Schakel et.al., 2010). However, as its string stability is not guaranteed, it performs worse than the CACC in Naus et.al. (2010). Hence, hereafter, we focus on the CACC-FIFT developed by Naus et.al. (2010) for comparison purposes. In the second experiment, we provide an optimal IFT updating scenario to study the transition process of switching optimal IFT when the platoon size changes. Additionally, as the controller cut-off frequency  $\omega_{K,i}$  has a significant impact on the performance of platoon control, the third experiment performs sensitivity analysis to illustrate the impact on system performance. The scenarios for control parameters  $\omega_{K,i}$  are labeled as scenarios 1 to 3 in Table 2.3, in which we sequentially increase the value of  $\omega_{K,i}$  for the four controller sets simultaneously.

Table 2.3. Values of  $\omega_{K,i}$  in the sensitivity analysis of controller cut-off frequency.

Scenario	1	2	3
CACC1	0.8	0.96	1.152
CACC2	0.8	0.96	1.152
CACC3	0.9	1.08	1.296
ACC	1.45	1.74	2.088

### **2.6.2 Performance of V2V communications, optimization result and computation efficiency**

To illustrate the performance of V2V communications under different ambient traffic conditions, we conduct simulations with different parameters. Fig. 2.7 shows the communication success rates under different ambient traffic conditions and different IFTs from the simulations in NS-3. In Fig. 2.7(a), the x-axis denotes the average traffic density  $\bar{k}$ . This study sets the range of average density from 25 vehicles/km to 40 vehicles/km. The success rate decreases with the increase in the percentage of vehicles with activated “send” functionalities of V2V communication devices in communication range. A higher percentage of activated “send” functionalities leads to more intense contentions for the chance to broadcast. For the same proportion of activated “send” functionalities in communication range,

a higher traffic density will result in a higher failure probability. This is because there are more vehicles in the communication range of each vehicle if the average density of ambient traffic flow is higher. Hence, there are more vehicles with activated “send” functionalities when the proportions are identical. Fig. 2.7(b) compares the simulation results under  $\bar{k} = 25$  with the contention model (discussed in Section 2.3.2) that is calibrated for the IFT optimization model. The mean error is  $-0.25\%$  and the standard deviation of the error is  $0.0526$ . Similar results are observed under different average densities, implying that the model can accurately describe the success rate under different percentages of activated “send” functionalities. We do not show all results due to the page limit.

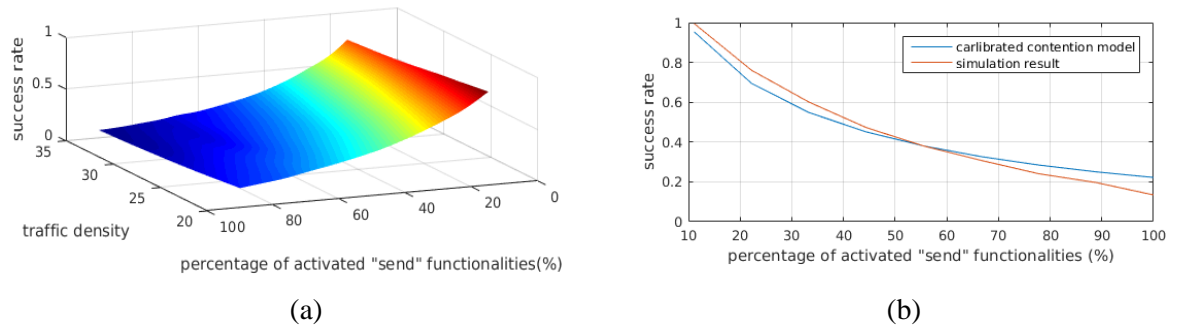


*Figure 2.7. Experiment results for V2V communications: (a) Communication success rates under different ambient traffic conditions; (b) Comparison of calibrated contention model and simulation results for  $k=20$ .*

Table 2.4 illustrates the optimal IFTs under different ambient traffic conditions and platoon sizes. It can be observed that the optimal IFTs are in accordance with Theorem 1 and Corollary 1. Consecutive vehicles with activated “send” functionalities can efficiently increase the occurrence of CACC cases, especially the CACC1 case which has much better control performance than the ACC case. However, the success rate of communication decreases since it increases the probability of information collision. Thereby, there are some consecutive vehicles with deactivated communication devices directly following those with activated ones, such as vehicles 3, 4, and 5 for the scenario with  $\bar{k}=25$  and  $N=14$ . For a given platoon size, the number of consecutive vehicles with deactivated “send” functionalities is bigger if the density  $\bar{k}$  is higher. For a given  $\bar{k}$ , there exist several activated/deactivated patterns of communication devices in the platoon. For example, the same pattern 111000 exists for the first 6 and last 6 vehicles in the scenario  $\bar{k}=25$ , and  $N=14$ , as the communication environment and control scheme are similar for a pattern.

Table 2.4. Network parameters.

N=14	Optimal IFT	$\bar{k}=25$	Optimal IFT
$\bar{k}=25$	111000111000110	N=11	111000111000
$\bar{k}=30$	111000001110000	N=12	1110001111000
$\bar{k}=35$	110000001110000	N=13	11100011110000
$\bar{k}=40$	110000000110000	N=14	111000111000110
		N=15	1110001110001100

To enable practical deployment of CACC-OIFT, computational efficiency should be verified. Though we improve the algorithmic efficiency in several parts as discussed in Section 2.5, it is a brute-force method; the computational time increases with platoon size. However, this is not an issue in our study as the platoon length cannot be too long because: (1) long platoons will block other vehicles from changing lanes (Van Arem et al., 2006), and (2) regulatory policies can limit platoon length in the real world to ensure safe travel experience for all vehicles. In our experiments, the optimization procedure for a platoon with 15 vehicles only takes 48.23 seconds on a PC with Intel E3-1505M 2.80GHz 8Gb. Further, in practice, parallel computing can be leveraged. Then, the computational time for this platoon reduces to 3.22 seconds. Since the optimal IFT is updated every time period (e.g., 5 minutes) or when ambient traffic oscillation conditions change significantly, this small computation time ensures the practical applicability of CACC-OIFT.

### 2.6.3 Control performance evaluation

The study evaluates the performance of the proposed CACC-OIFT through three numerical experiments, in which we compare the control performance to the other two controllers (CACC-FIFT and CACC-DIFT), investigate the transition process when the optimal IFT is updated, and illustrate the impact of cut-off frequency  $\omega_{K,i}$  on platoon control performance.

Comparison between controllers

Here, we first compare the performance of CACC-OIFT with those of CACC-DIFT and CACC-FIFT. The experiments analyze the three controllers in the context of unreliable V2V communications by simulating in NS-3. A 15-CAV platoon is analyzed in a traffic flow with average density 28.57 vehicle/km for 240s. The ambient traffic conditions do not change significantly. Under CACC-OIFT, the vehicle platoon will follow the IFT from the optimization model (111000111000110). Fig. 2.8 shows the spacing speed tracking error between adjacent vehicles in the platoon under these controllers, and Fig. 2.9 shows the standard deviations of the spacing and speed tracking errors, and vehicle speed.

Fig. 2.8 illustrates that the spacing error of vehicles is mitigated based on their positions in the platoon. The figure shows that CACC-OIFT outperforms the other two controllers. For example, the maximum spacing error of the second following vehicle ( $i=2$ ) under CACC-OIFT is 1.05m, compared with 1.42m for CACC-DIFT and 1.51m for CACC-FIFT. For the last

following vehicle ( $i=14$ ), the maximum spacing errors are 0.37m, 0.68m and 0.79m for CACC-OIFT, CACC-DIFT and CACC-FIFT, respectively. The standard deviations of spacing and speed tracking errors are compared for the three controllers in Fig. 2.9(a) and Fig. 2.9(b), respectively. Fig. 2.9(a) shows that the standard deviation of spacing error decreases sequentially across vehicles in the platoon for all controllers. However, CACC-OIFT performs better than the other two controllers as its spacing error reduces the quickest. Further, the profile of the spacing error standard deviation cycles from steep to flat. For example, the spacing error is reduced significantly for first 4 vehicles and then is almost constant for vehicles  $i=5$  and  $i=6$ . This is because the IFT optimization deactivates the ‘send’ functionalities of V2V communication devices for several vehicles. Thus, some vehicles will operate under the ACC case, which does not leverage V2V connectivity. However, these deactivations lead to more reliable V2V communication connections for remaining links in CACC-OIFT and the consequent significant tracking error reduction for the vehicles. A similar trend is observed in Fig. 2.9(b) which shows the standard deviation of the speed tracking error.

To further investigate the performance benefits under CACC-OIFT, the performance of the three CACC control strategies is compared when traffic oscillates (e.g., stop-and-go or slow-and-fast traffic). The standard deviations of the vehicle speed are shown in Fig. 2.9(c). It illustrates that the fluctuation in standard deviation of speed decreases under all three schemes as the tail of the platoon is approached, which implies that traffic oscillations are damped. Further, CACC-OIFT reduces the speed fluctuations significantly as it proactively leverages the dynamic nature of the IFT. In summary, we conclude that the performance of a CAV platoon controlled by the proposed CACC-OIFT is better and more robust than that of the other two controllers in a realistic V2V communications environment. Also, based on the discussion in Section 2.1, CACC-DIFT performs better than CACC-FIFT as it considers IFT dynamics, albeit passively, unlike CACC-FIFT which assumes a fixed IFT.

#### Transition process of optimal IFT

Next, we analyze the transition process of switching optimal IFT. In this experiment, a 14-CAV platoon is initially set up and controlled using CACC-OIFT with the optimal IFT from the optimization model (11100011110000). In the middle of the experiment (in time), a CAV approaches the tail of the platoon. At the 120th second, its headway becomes 1.5s, and this CAV joins the platoon (it terminates individual control mode and starts to apply the CACC-OIFT of the platoon). Then, as the platoon size changes from 14 to 15, the optimal IFT is updated to 111000111000110. Fig. 2.10 shows the spacing error, the speed, and the acceleration for all CAVs.

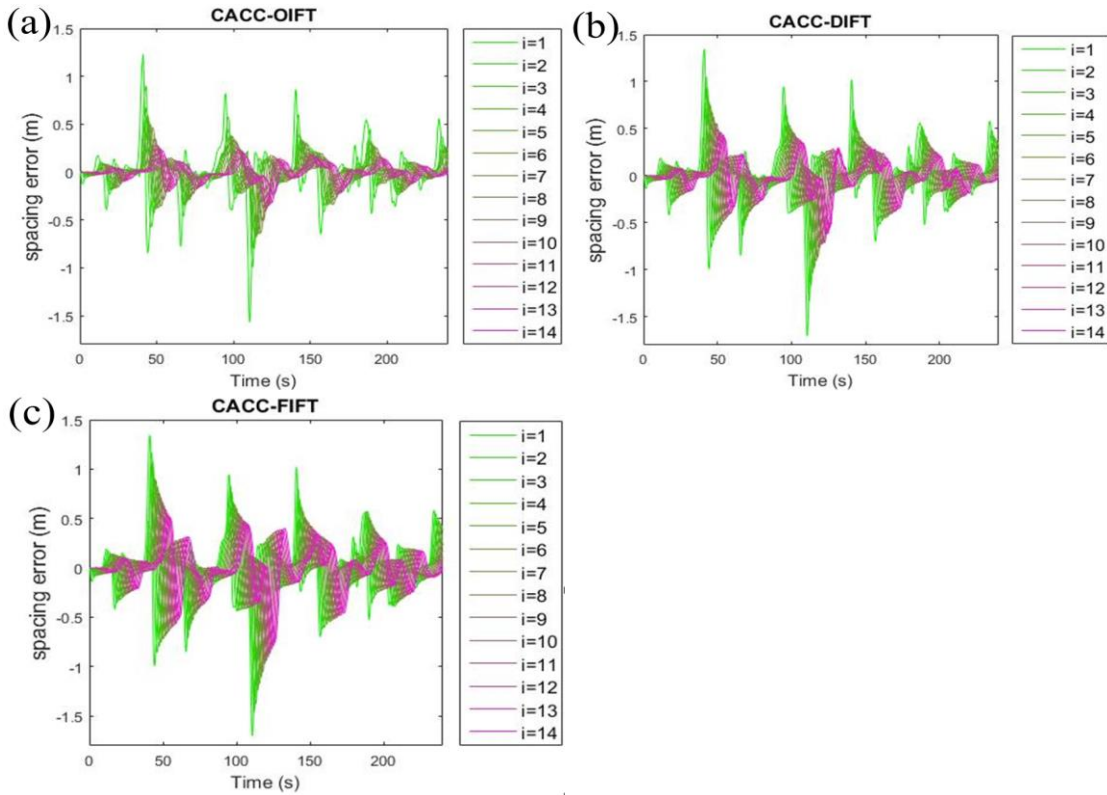


Figure 2.8. Spacing error under different controllers: (a) CACC-OIFT; (b) CACC-DIFT; (c) CACC-FIFT.

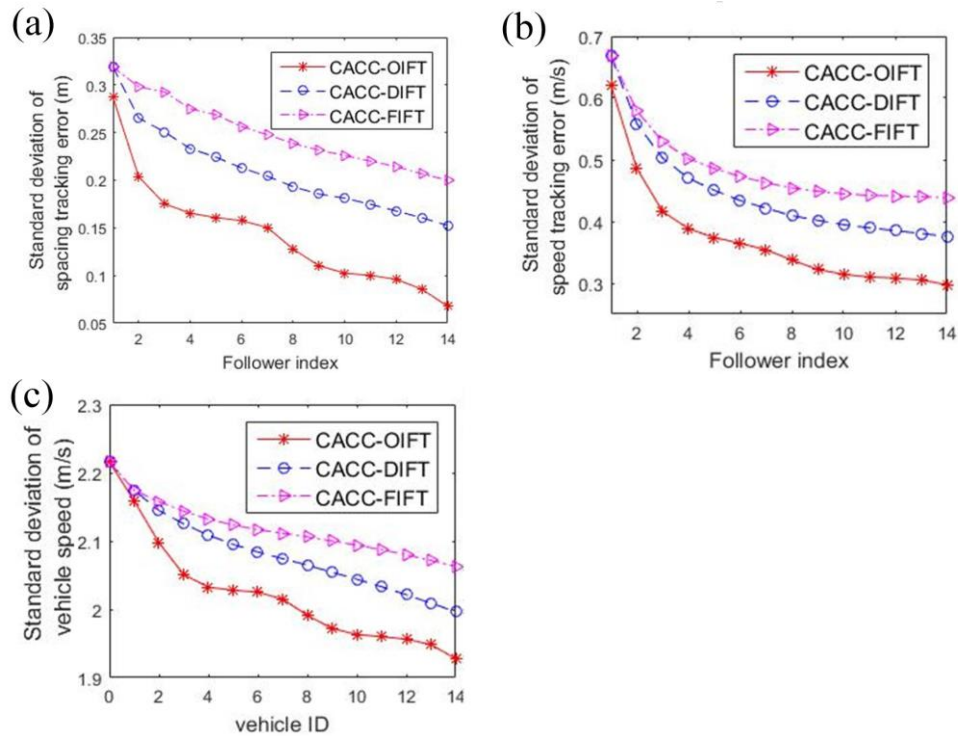
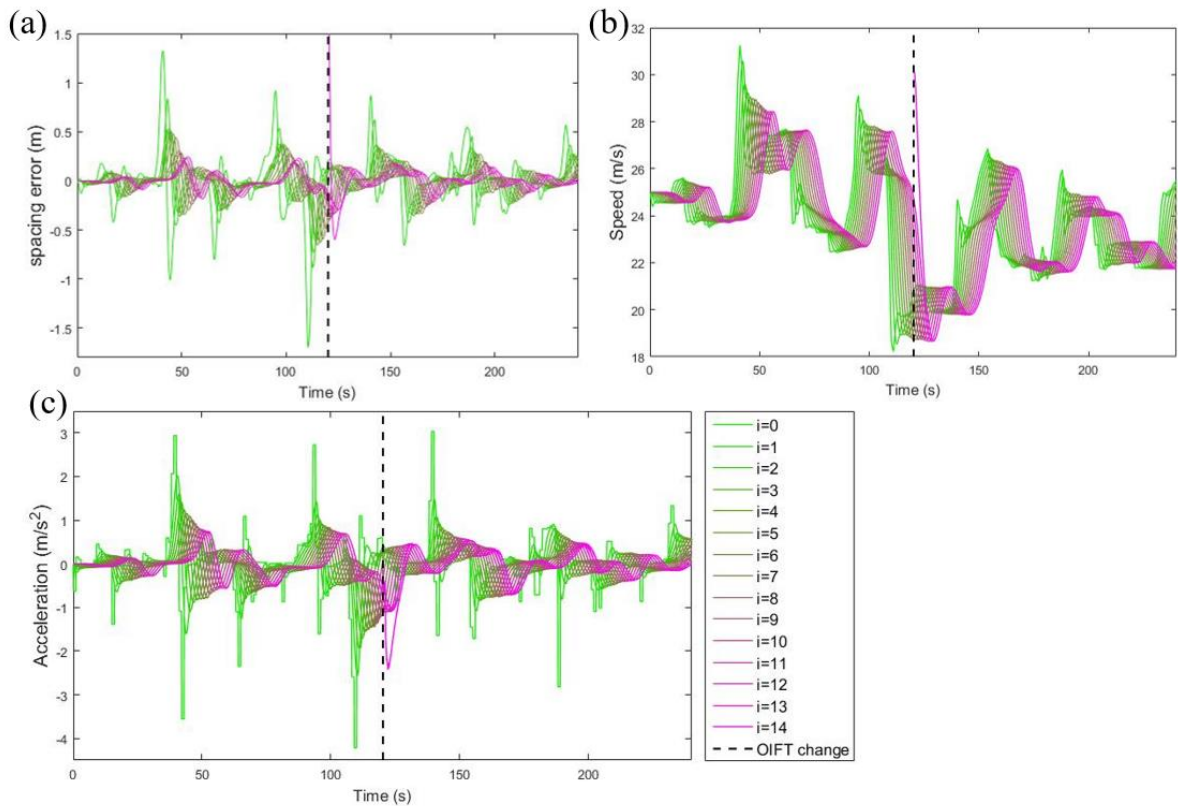


Figure 2.9. Standard deviation of: (a) spacing error; (b) speed tracking error; (c) vehicle speed.

The results illustrate that the proposed CACC-OIFT is not affected by the transition of the optimal IFT. Specifically, in Fig. 2.10(a), the preceding 13 CAVs can still follow their leading vehicles with stable spacing errors after the last following CAV ( $i=14$ ) joins in the platoon. The spacing error is also mitigated from the head to the tail of the platoon before and after the transition. The transition does not trigger any additional speed oscillations or acceleration oscillations for the platoon, as shown in Figs. 2.10(b) and 2.10(c). The last following CAV ( $i=14$ ) decelerates appropriately to join the platoon with the desired headway (i.e., 1s). In this process, the maximum spacing error is 0.51m, and the maximum acceleration rate is  $-2.58\text{m/s}^2$ . The reason for the maximum acceleration rate of the last following CAV ( $i=14$ ) being greater than that of its immediate predecessor CAV ( $i=13$ ) is because the relative speed is almost  $-5\text{m/s}$  when the last CAV joins in the platoon. Thereby, it has to decelerate abruptly. After the join-in process (i.e., after 145s), the maximum acceleration rate of the last following CAV ( $i=14$ ) becomes smaller than that of its immediate predecessor, and the string stability performance is maintained. This indicates that the transition of optimal IFT induced by a change in platoon size through the addition of another CAV does not impact the performance of CACC-OIFT.



*Figure 2.10. Performance of the platoon in IFT transition period:  
(a) spacing error; (b) speed; (c) acceleration.*

Sensitivity analysis of cut-off frequency

The sensitivity analysis of the cut-off frequency  $\omega_{K,i}$  is conducted by comparing the spacing errors and vehicle acceleration in Scenarios 1, 2 and 3, as shown in Figs. 2.11 and 12, respectively. Fig. 2.11 illustrates that spacing error will decrease as the value of  $\omega_{K,i}$  increases. For example, the maximum spacing error of the last following vehicle in Scenarios 1, 2 and 3 are 0.37m, 0.32m, and 0.24m, respectively. However, Fig. 2.12 shows that with the increase of  $\omega_{K,i}$ , the effect of high-frequency measurement noise will increase in the acceleration profile as it reaches the tail of the platoon (such as the parts marked by red circles in Fig. 2.12 (b)), which is undesirable from the perspective of passengers' comfort and vehicle operation.

Insights into the above observations can be generated by characteristics related to string stability performance and measurement noise mitigation. From the standpoint of string stability performance, the string stability transfer functions in Equations (2.45) and (2.47) imply that increasing the controller cut-off frequency  $\omega_{K,i}$  will decrease the value of string stability transfer function, improving the damping effect of traffic oscillations. However, for the noise mitigation effect, the complementary sensitivity functions in Equations (2.36) and (2.37) indicate that as the value of  $\omega_{K,i}$  becomes larger, the noise mitigation factor will increase, degrading the noise mitigation performance. Hence, increasing controller cut-off frequency will jeopardize the control performance related to noise mitigation. Hence, to enable an acceptable level of platoon control performance, a careful selection of the controller cut-off frequency  $\omega_{K,i}$  is essential for real-world application.

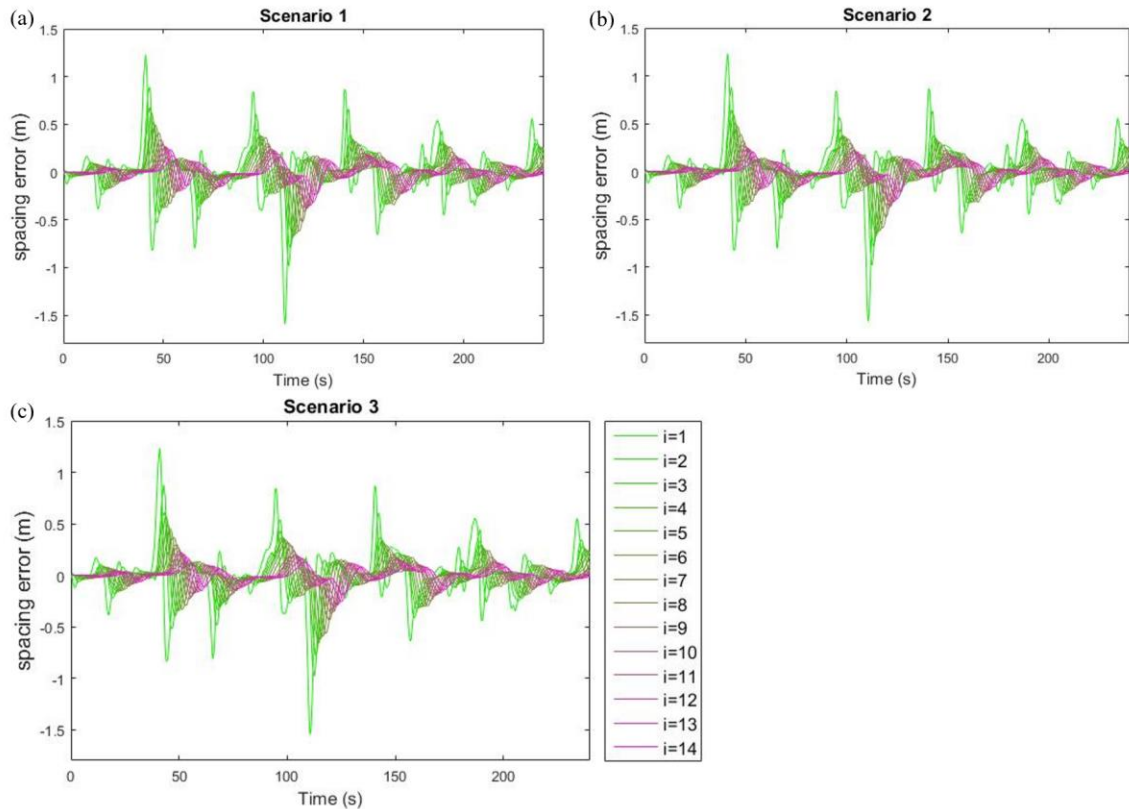


Figure 2.11. Spacing error profile of: (a) Scenario 1; (b) Scenario 2; (c) Scenario 3.

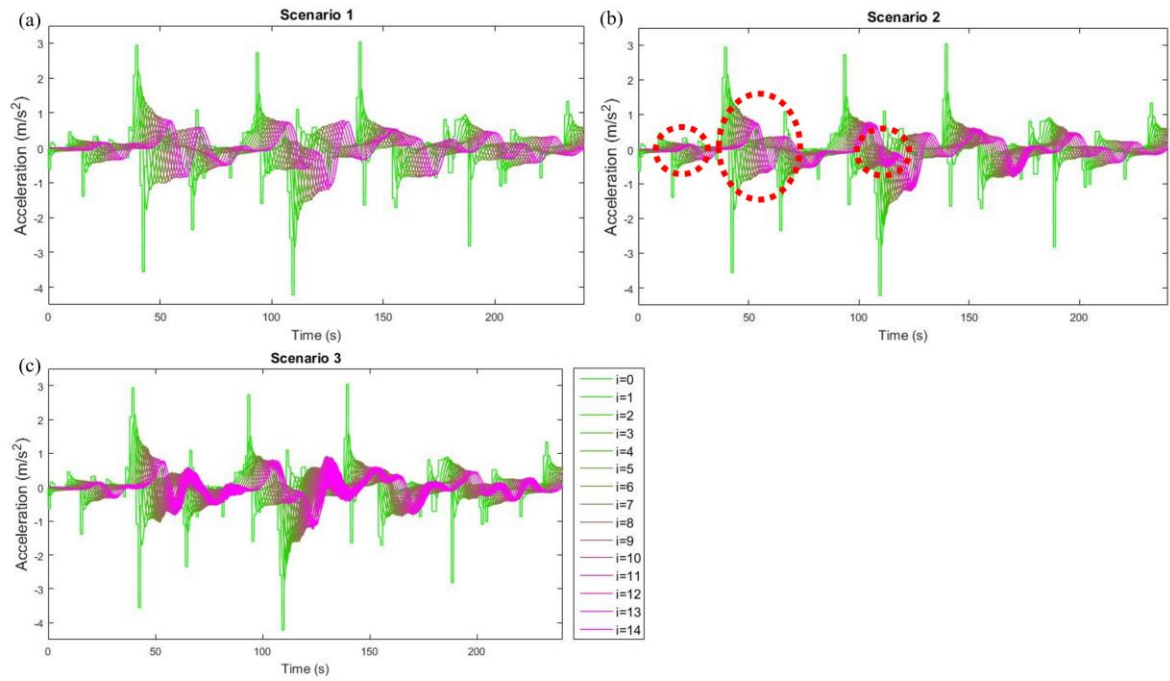


Figure 2.12. Acceleration profile of: (a) Scenario 1; (b) Scenario 2; (c) Scenario 3.

### **3. SMOOTH SWITCHING CONTROL BASED CACC CONSIDERING DYNAMIC INFORMATION FLOW TOPOLOGY**

#### **3.1 Introduction**

Connected and autonomous vehicle (CAV) related technologies provide enormous opportunities for innovation which can improve traffic safety, efficiency, and environmental sustainability (Horowitz and Varaiya, 2000), such as Adaptive Cruise Control (ACC), and Cooperative Adaptive Cruise Control (CACC) (Xiao et al., 2018). By leveraging vehicle-to-vehicle (V2V) communications in the platoon control process, the CACC controls individual CAV car-following behaviors by utilizing both onboard sensors and information exchanged between neighboring vehicles to improve traffic efficiency and safety. Since CAVs can receive more information than non-connected autonomous vehicles through V2V communications, CACC can coordinate CAV movements more flexibly and intelligently to achieve better platooning and system-level control performance, such as improved highway capacity (Horowitz and Varaiya, 2000), more effective energy saving (McAuliffe et al., 2018), and enhanced string stability performance (i.e., attenuation of shockwave propagation) (Naus et al., 2010).

However, V2V communication failures are inevitable, especially in high-density CAV (Kim et al., 2017; Wang et al., 2017) environments, as the substantial ongoing communication links will significantly contribute to the source of communication failures, such as information congestion, latency, and package loss. Correspondingly, communication failures will dynamically vary the information flow topology (IFT). Since IFT is a critical component of CACC (Li et al., 2015), the inherent variability in IFT leads to negative effects on CACC when it is designed using a fixed IFT. To deal with IFT dynamics and uncertainties in controller design, Gao et al. (Gao et al., 2018) proposed a distributed adaptive sliding mode controller to counteract the uncertainties in the information flow matrix. Remarkably, the switching control is an effective approach as well. Gong et al. (2019) proposed the CACC-DIFT method in which fixed-gain controllers can switch adaptively according to dynamic IFT so that string stability and noise mitigation are guaranteed. By leveraging the characteristics of dynamic IFT and switching control scheme, Wang et al. (2019) developed a two-step optimization algorithm to dynamically obtain an optimal IFT that deactivates the “send” functionalities of some CAVs in the platoon, which optimally trades off the probability of communication failure and string stability performance.

However, the switching control strategy may lead to bumpy control inputs due to the potential differences in the transient responses of different controller sets (Cheong and Safonov, 2008). In the case of CACC, bumpy control inputs lead to choppy vehicle acceleration profile (i.e., vehicle will jerk at the switching instance), which is uncomfortable for passengers and hazardous for vehicle powertrain. Hence, a smoothing technique for switching control is essential for CACC in a dynamic IFT environment. The solution of smooth transition is to suppress the sources of bumpy transition: (i) different transient responses between controller sets at switching instances, and (ii) contaminated vehicle states caused by the existence of sensor measurement noise and acceleration

disturbances in platoon control operation (Zhou et al., 2017).

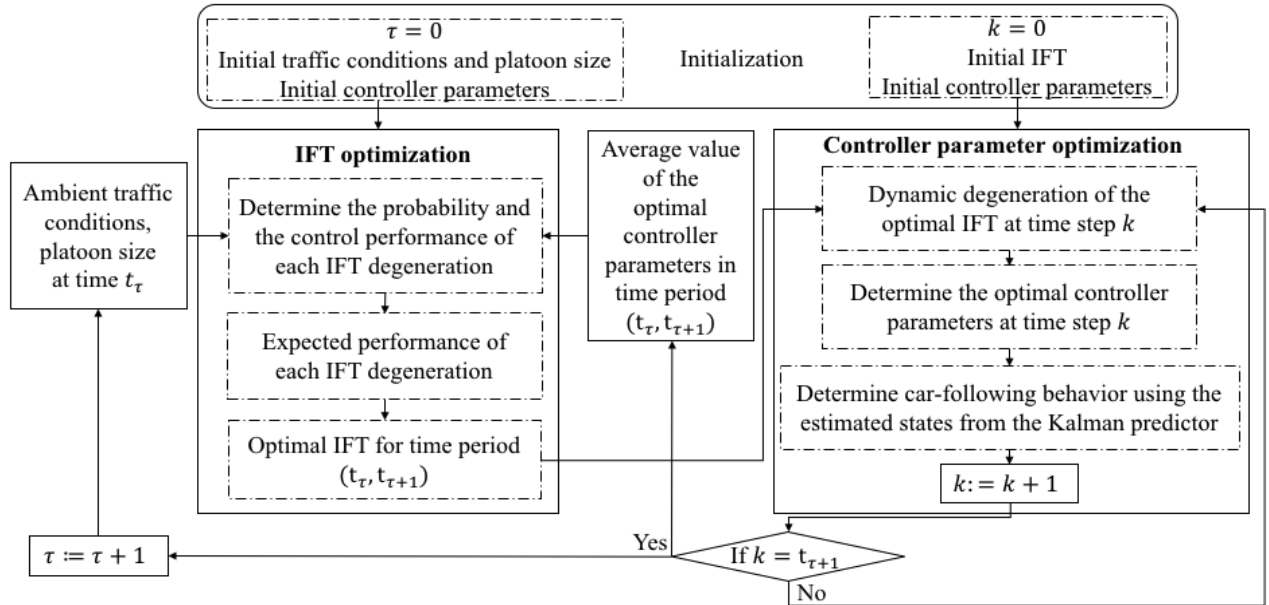


Figure 3.1. Conceptual flowchart of the CACC-SOIFT

To alleviate the problem of different transient responses, there are three underlying approaches: (i) reducing the frequency of controller switching, (ii) reducing the difference between controller transient responses, and (iii) suppress the measurement noise and acceleration disturbances during CACC/ACC operations. Correspondingly, trade-offs exist for the first two approaches. To reduce the frequency of controller switching, the first trade-off exists between the probability of communication failure and the control performance (i.e., string stability and smooth acceleration). The most robust IFT (i.e., deactivating all V2V communications) has the worst idealized control performance (i.e., the control performance without communication failures), while the IFT with all V2V communications functionalities activated has the best idealized control performance but leads to high probability of communication failure and the highest controller switching frequency. The second trade-off is between the tracking performance and riding comfort (jerk minimization) performance. Specifically, in order to achieve desired tracking performance, vehicles need to be responsive or sensitive to the speed and acceleration changes of preceding vehicles, which can induce abrupt changes in control input (i.e., acceleration command), and thereby jeopardize riding comfort.

Motivated by the aforementioned two trade-offs and the two sources of bumpy transition, we propose a smooth switching control based CACC scheme with IFT optimization, denoted as CACC based on smooth-switching optimal IFT (CACC-SOIFT) framework, with three smoothing strategies: IFT optimization, controller parameter optimization, and Kalman predictor. By deactivating the “send” functionality of some CAVs, the first-layer IFT optimization model seeks optimal trade-offs between communication reliability and control performance (i.e., damping oscillations and ensuring comfort) to generate an optimal robust IFT, such that controller switching can be minimized. The second-layer controller parameter optimization adjusts controller gains at

each time step  $k$  to minimize the difference between control inputs while maintaining string-stable tracking, so as to trade-off tracking performance and riding comfort. Both layers interact iteratively with each other to achieve the desired platoon control performance. As illustrated in Fig. 3.1, given the ambient traffic conditions and platoon size of the time period  $\tau$  (i.e., time span from  $t_\tau$  to  $t_{\tau+1}$ ), the first layer optimizes the IFT and then delivers the optimal IFT to the second layer. As the model used in the first-layer optimization is associated with controller parameters, at time instance  $t_\tau$ , the second layer provides the average values of optimal controller parameters from the previous time period  $\tau$  (i.e., time span from  $t_{\tau-1}$  to  $t_\tau$ ) to the first layer, such that the IFT can be updated based on the optimal parameter setting that corresponds to platoon operations under different ambient traffic conditions. Note that the time interval  $\tau$  is not a fixed value for real-time operations, and the optimal IFT needs to be updated when ambient traffic conditions or platoon length change. Also, in real-world operations, the platoon leader gathers information on ambient traffic conditions and platoon length from the roadside unit to perform the first-layer IFT optimization, and then distributes the optimal IFT to all of the following vehicles. Each following vehicle performs the second-layer controller parameter optimization in a distributed manner and delivers the optimal controller parameters back to the platoon leader.

Additionally, to suppress measurement noise generated from onboard sensors and the acceleration disturbances of the vehicle, a Kalman filter is applied to estimate actual states from the contaminated ones. The estimated states will be utilized in the controller to guarantee smooth response. Additionally, since CACC can achieve better control performance (i.e., string stability and faster converging rate) compared to ACC (Gong et al., 2019; Ploeg et al., 2015), the Kalman predictor is formulated using the Kalman filter to estimate vehicle acceleration as communication failures occur, so that CACC can be reconstructed from ACC in some scenarios to improve the control performance and smoothness of acceleration.

The remainder of the paper is organized as follows. The next section briefly introduces the formulation of IFT degeneration and controller structure. The first-layer IFT optimization is presented in the section thereafter. Then, the second-layer controller parameter optimization is formulated. The section thereafter articulates the methods to address measurement noise and estimation of vehicle states. Then, the proposed CACC-SOIFT is validated using numerical experiments. Finally, concluding comments and future directions are discussed.

### **3.2 Formulation of platoon control**

This study assumes a homogeneous CAV platoon. Through V2V communications, each CAV has the “send” functionality to broadcast information to other vehicles, and can receive information based on the benchmark IFT. The benchmark IFT here is the two-predecessor following topology, where each CAV (e.g. vehicle  $i$  in Fig. 3.2(a)) can receive information on kinematic states (i.e., absolute position, speed, and acceleration) from the two closest preceding vehicles (vehicles  $i - 1$  and  $i - 2$  in Fig. 3.2(a)). Due to communication failures, the benchmark IFT (i.e., CACC1 in Fig. 3.2(a)) may degenerate to the three potential scenarios shown in Figures 3.2(b)-3.2(d). Note that Fig. 3.2 is drawn based on the perspective of ego CAV  $i$ .

### 3.2.1 IFT degeneration and receiver status

Figure 3.2 presents the receiver status and controller sets.

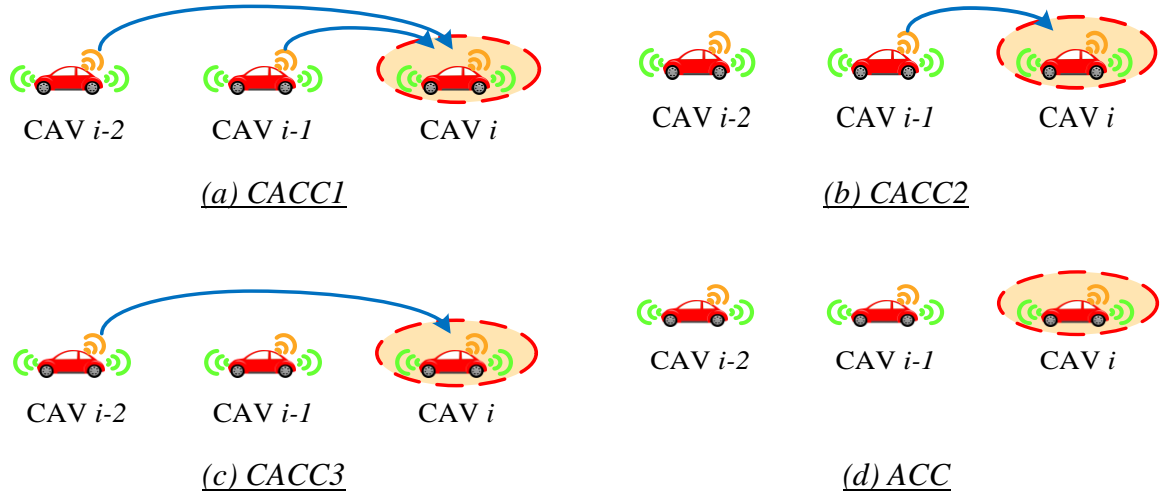


Figure 3.2. Receiver status and controller sets

Since the IFT optimization involves activation and deactivation of “send” functionality, to describe the IFT in a CAV platoon, we introduce a sender status vector  $\xi$ .  $\xi = [\eta_0, \eta_1, \dots, \eta_N]$ ,  $\eta_i \in \{0, 1\}$  for  $i = 0, 1, \dots, N$  to indicate the expected IFT of a platoon with  $N + 1$  vehicles.  $\eta_i$  indicates send status of vehicle  $i$ :  $\eta_i = 0$  means deactivated “send” functionality,  $\eta_i = 1$  implies activated “send” functionality. Then, we define  $\xi_d(\xi)$  as the possible degeneration scenarios of expected IFT  $\xi$ .

As illustrated in section 3.2 of (Wang et al., 2019), the receiver status (i.e., the controller that the vehicle will apply) of each vehicle in the platoon is dependent on the degeneration of the expected benchmark IFT. Correspondingly, the receiver status vector  $\zeta(\xi_d(\xi))$  can be formulated using  $\xi_d(\xi)$ :

$$\zeta(\xi_d(\xi)) = \begin{bmatrix} \zeta_0(\xi_d(\xi)) \\ \zeta_1(\xi_d(\xi)) \\ \vdots \\ \zeta_N(\xi_d(\xi)) \end{bmatrix}^T = \begin{bmatrix} 4 \\ 4 \\ \vdots \\ 4 \end{bmatrix}^T - \xi_d(\xi) \begin{bmatrix} 0 & 2 & 1 & 0 & \dots & 0 \\ \vdots & 0 & 2 & \ddots & \ddots & \vdots \\ \vdots & \ddots & \ddots & \ddots & \ddots & 0 \\ \vdots & \ddots & \ddots & \ddots & 2 & 1 \\ \vdots & \ddots & \ddots & \ddots & 0 & 2 \\ 0 & \dots & \dots & \dots & \dots & 0 \end{bmatrix} \quad (3.1)$$

in which  $\zeta_i(\xi_d(\xi))$  is the corresponding receiver status of vehicle  $i$  in a platoon with IFT degeneration scenario  $\xi_d$ ,  $\zeta_i \in \{1, 2, 3, 4\}$  for  $i = 0, 1, \dots, N$ . Additionally, as illustrated in Fig. 3.2, the receiver status  $\zeta_i(\xi_d(\xi)) = 1, 2, 3, 4$  indicates that vehicle  $i$  is controlled under CACC1, CACC2, CACC3, or ACC strategy, respectively.

### 3.2.2 Controller structure

The controller design is inspired by our previous work (Gong et al., 2019). The control schematic of vehicle  $i$  in the platoon is depicted in Fig. 3.3.  $X_i$  and  $U_i$  are the absolute position and control inputs of vehicle  $i$ , respectively.  $U_{f,i-1}$  ( $U_{f,i-2}$ ) is the feedforward input generated from the acceleration  $\ddot{X}_{i-1}$  ( $\ddot{X}_{i-2}$ ) of vehicle  $i-1$  ( $i-2$ ).  $U_{b,i}$  is the feedback input generated from tracking error  $E_i$ .  $X_{d,i}$  represents the (desired) virtual arrival position of vehicle  $i$ .  $\alpha_{b,i}(\zeta_i)$ ,  $\alpha_{f,i}(\zeta_i)$ ,  $\beta_{b,i}(\zeta_i)$ ,  $\beta_{f,i}(\zeta_i)$ ,  $G_i$ ,  $H_i$ ,  $K_i$ , and  $F_{l,i}$  ( $l \in \{1,2\}$ ) are discussed below.

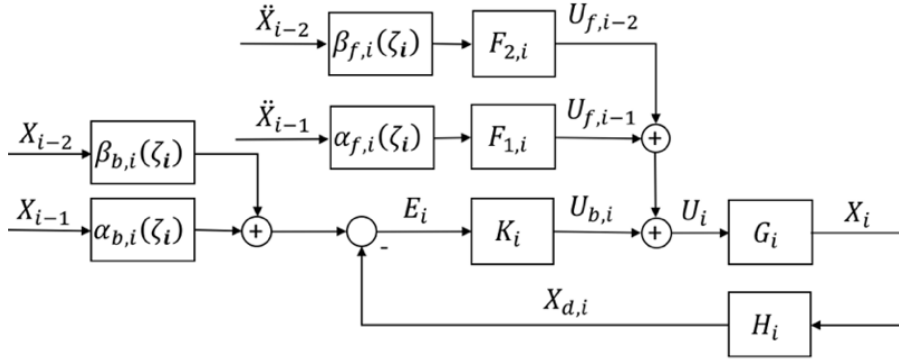


Figure 3.3. Block diagram of control schematic

Indicator values. The indicator values corresponding to receiver status will be applied to switch controllers for different IFTs, as described in Table 3.1.

Table 3.1. Indicator values for controller sets

Controller	$\zeta_i$	$\alpha_{b,i}(\zeta_i)$	$\alpha_{f,i}(\zeta_i)$	$\beta_{b,i}(\zeta_i)$	$\beta_{f,i}(\zeta_i)$
CACC1	1	$\alpha$	$\alpha$	$\beta$	$\beta$
CACC2	2	1	1	0	0
CACC3	3	0	0	1	1
ACC	4	1	0	0	0

The weighting factors  $\alpha$  and  $\beta$  are subject to following constraints:  $\alpha + \beta = 1$ ,  $0 \leq \alpha, \beta \leq 1$ . Vehicle dynamics. With the assumption that a fundamental controller is used to address nonlinearities in vehicle operation, the longitudinal vehicle dynamics can be approximated using a third-order model (Zheng et al., 2018):

$$G_i(s) = \frac{X_i(s)}{U_i(s)} = \frac{1}{s^2(\tau_i s + 1)} \quad (3.2)$$

The vehicle time constant  $\tau_i \in (0,1)$  represents the inertial delay of vehicle powertrain.  $\tau_i$  is identical for all CAVs in a homogeneous platoon.

Note that  $s$  is the Laplace operator for control design in Laplace domain. In addition,  $s = j\omega$

will be further used for analysis of string stability performance in frequency domain.  $\omega$  is the angular frequency, and  $j$  is the indicator of complex number. By using  $s$  as a differentiator, and  $\frac{1}{s}$  as an integrator, each transfer function in Laplace domain can be converted to specific ordinary differential equation in time domain.

Spacing policy. The constant time headway (CTH) is applied by factoring string stability and safety (Naus et al., 2010):

$$H_i(s) = 1 + (2 - \alpha_{b,i}(\zeta_i)) h_d s \quad (3.3)$$

in which  $h_d$  is the desired time headway between vehicles.

Feedback controller. To rectify the spacing error and speed tracking error, a PD feedback controller is devised:

$$K_i(s) = k_{p,i} + k_{d,i}s \quad (3.4)$$

where  $k_{p,i}$  and  $k_{d,i}$  are the controller proportional gain and derivative gain for vehicle  $i$ , respectively.

Feedforward filter. Feedforward filters are applied to process the acceleration of preceding vehicles to guarantee string stability performance. The formulation is expressed as:

$$F_{l,i}(s) = k_{f,l} \frac{1 + \tau_i s}{H_i(s)}, l \in \{1,2\} \quad (3.5)$$

where  $k_{f,l}$  is feedforward gain for the  $l$ th ( $l \in \{1,2\}$ ) preceding vehicle. The numerator is designed for canceling the inertial delay in vehicle dynamics to enhance string stability performance.

Control input. As illustrated in Fig. 3.3, the control input of vehicle  $i$  consists of two feedforward terms  $U_{f,i-l}(s)$ ,  $l \in \{1,2\}$ , and a feedback term  $U_{b,i}(s)$ :

$$\begin{aligned} U_i(s) &= U_{b,i}(s) + U_{f,i-1}(s) + U_{f,i-2}(s) \\ &= k_{p,i}E(s) + k_{d,i}\dot{E}(s) + \alpha_{f,i}(\zeta_i)F_{1,i}(s)\ddot{X}_{i-1}(s) \\ &\quad + \beta_{f,i}(\zeta_i)F_{2,i}(s)\ddot{X}_{i-2}(s) \end{aligned} \quad (3.6)$$

where the spacing error can be expressed as:

$$E_i(s) = \alpha_{b,i}(\zeta_i)X_{i-1}(s) + \beta_{b,i}(\zeta_i)X_{i-2}(s) - H_i(s)X_i(s) \quad (3.7)$$

### 3.2.3 Stability analysis

In this section, we analytically set up some conditions for controller parameters to guarantee local stability and string stability, such that vehicle movements are stable and traffic oscillations can be attenuated in the platoon.

Local stability. The local stability is associated with the movement of each individual vehicle in the platoon. If a vehicle is locally stable in the platoon, it will converge to the equilibrium position and equilibrium speed asymptotically as time progresses. To ensure local stability, the poles (the roots of the denominator) of the closed-loop sensitivity transfer function need to be in the left half complex plane (LHP) (Gong et al., 2019).

The sensitivity transfer function  $T_i(s)$  is used to describe the relationship of the virtual arrival position of vehicle  $i$  with the positions of preceding vehicles:

$$X_{d,i}(s) = \alpha_{b,i}(\zeta_i)T_i(s)X_{i-1}(s) + \beta_{b,i}(\zeta_i)T_i(s)X_{i-2}(s) \quad (3.8)$$

where

$$T_i(s) = \frac{X_{d,i}(s)}{X_{i-1}(s)} = \frac{X_{d,i}(s)}{X_{i-2}(s)} = \frac{H_i(s)G_i(s)K_i(s)}{1 + H_i(s)G_i(s)K_i(s)} \quad (3.9)$$

Substituting in  $G_i$ ,  $H_i$ , and  $K_i$ ,  $T_i(s)$  can be expressed as:

$$T_i(s) = \frac{k_{d,i}s^2 + (k_{d,i} + k_{p,i}h_d)s + k_{p,i}}{\tau_i s^3 + (1 + k_{d,i}h_d)s^2 + (k_{d,i} + k_{p,i}h_d)s + k_{p,i}} \quad (3.10)$$

We then apply the Routh-Hurwitz stability criterion to analyze the positions of the roots of the denominator. The specific steps of the Routh-Hurwitz test are as follows:

First, we rearrange the coefficients of the denominator of  $T_i(s)$  in (3.10) in the Routh-Hurwitz array:

$s^3$	$\tau_i$	$k_{d,i}$ $+ k_{p,i}h_d$	0	
$s^2$	$1 + k_{d,i}h_d$	$k_{p,i}$	0	
$s^1$	$\frac{(k_{d,i} + k_{p,i}h_d)(1 + k_{d,i}h_d) - \tau_i k_{p,i}}{(1 + k_{d,i}h_d)}$	0	0	(3.11)
$s^0$	$k_{p,i}$	0	0	

Then, according to the Routh-Hurwitz theorem, to guarantee that the roots of the characteristic equation are located in the LHP, we need to constrain all entries in the second column of (3.11) to be positive. Thereby, the condition for local stability can be expressed as:

$$k_{p,i} > 0 \quad (3.12)$$

$$k_{d,i} > -\frac{1}{h_d} \quad (3.13)$$

$$(k_{d,i} + k_{p,i}h_d)(1 + k_{d,i}h_d) > \tau_i k_{p,i} \quad (3.14)$$

String stability. The string stability can be interpreted as a stable property of signal propagation. In the case of string-stable platoon control, the fluctuations of vehicle speed, or the disturbances of vehicle movement will not be amplified upstream of the platoon, indicating that traffic oscillations can be damped effectively.

In this study, we apply the head-to-tail string stability transfer function (SSTF)  $SS_{X,i}(s, \zeta_i(\xi_d(\xi)))$  to measure the propagation of traffic oscillations. The SSTF is defined as the ratio of the trajectory oscillations of vehicle  $i$  and leading vehicle 0:

$$\begin{aligned}
 SS_{X,i}(s, \zeta_i(\xi_d(\xi))) &= \frac{X_i(s)}{X_0(s)} \\
 &= \left( \alpha_{f,i}(\zeta_i) \Lambda_{f,i-1}(s) + \alpha_{b,i}(\zeta_i) \Lambda_{b,i-1}(s) \right) \frac{X_{i-1}(s)}{X_0(s)} \\
 &\quad + \left( \beta_{f,i}(\zeta_i) \Lambda_{f,i-2}(s) + \beta_{b,i}(\zeta_i) \Lambda_{b,i-2}(s) \right) \frac{X_{i-2}(s)}{X_0(s)}
 \end{aligned} \tag{3.15}$$

where  $\Lambda_{f,i-l}(s) = \frac{G_i F_{l,i} s^2}{1 + G_i K_i H_i}$ ,  $l \in \{1, 2\}$ ,  $\Lambda_{b,i-1}(s) = \Lambda_{b,i-2}(s) = \frac{G_i K_i}{1 + G_i K_i H_i}$ .

Substituting  $s = j\omega$ , the following condition is essential to ensure string stability:

$$\left\| SS_{X,i}(j\omega) \right\|_{\infty} = \left\| \frac{X_i(j\omega)}{X_0(j\omega)} \right\|_{\infty} \leq 1 \tag{3.16}$$

As the SSTF is a complex high-order transfer function, we use the worst case in control design for Equation (3.15), where  $X_{i-2}/X_0$  and  $X_{i-1}/X_0$  are both set as equal to one, implying a marginal string stability (i.e., the traffic oscillation is neither amplified nor attenuated upstream of the platoon). Thereby, we can obtain a more conservative and safer condition for string stability. Substituting  $G_i$ ,  $H_i$ ,  $K_i$ , and  $F_{l,i}$  into Equation (3.15), the simplified expression for SSTF is obtained as:

$$\begin{aligned}
 &SS_{X,i}(s, \zeta_i(\xi_d(\xi))) \\
 &= \begin{cases} \frac{k_{f,l}}{1 + (2 - \alpha_{b,i}(\zeta_i)) h_d s}, & \zeta_i \in \{1, 2, 3\} \\ \frac{k_{d,i} s + k_{p,i}}{\tau_i s^3 + (1 + k_{d,i} h_d) s^2 + (k_{d,i} + k_{p,i} h_d) s + k_{p,i}}, & \zeta_i = 4 \end{cases}
 \end{aligned} \tag{3.17}$$

The string stability is achieved via satisfying Equation (3.16). Applying similar arithmetic operations in (Gong et al., 2019), the string stability conditions can be derived as follows.

For CACC cases, string stability requires:

$$\left\| SS_{X,i}(s, \zeta_i(\xi_d(\xi))) \right\|_{\infty} = \left\| \frac{k_{f,l}}{1 + (2 - \alpha_{b,i}(\zeta_i)) h_d s} \right\|_{\infty} \leq 1 \tag{3.18}$$

which can be satisfied using following condition (8):

$$\left| SS_{X,i}(j\omega, \zeta_i(\xi_d(\xi))) \right| = \left| \frac{k_{f,l}}{1 + j(2 - \alpha_{b,i}(\zeta_i)) h_d \omega} \right| \leq 1 \tag{3.19}$$

Thus, Equation (3.19) is equivalent to:

$$\left| SS_{X,i}(j\omega, \zeta_i(\xi_d(\xi))) \right| = \frac{|k_{f,l}|}{\sqrt{1 + \left( (2 - \alpha_{b,i}(\zeta_i)) h_d \omega \right)^2}} \leq 1 \tag{3.20}$$

The inequality in (3.16) can then be valid by restricting  $h_d > 0, 0 < k_{f,l} \leq 1, l \in \{1,2\}$ , which solidifies the string stability requirement in ACC cases.

For ACC case, utilizing the same procedures in CACC cases, string stability can be guaranteed via:

$$\begin{aligned} & |SS_{X,i}(j\omega, \zeta_i(\xi_d(\xi)))| \\ &= \frac{\sqrt{k_{p,i}^2 + (k_{d,i}\omega)^2}}{\sqrt{(k_{p,i} - (1 + k_{d,i}h_d)\omega^2)^2 + ((k_{d,i} + k_{p,i}h_d)\omega - \tau_i\omega^3)^2}} \leq 1 \end{aligned} \quad (3.21)$$

By moving the denominator to the right-hand side, Equation (3.21) can be transformed to:

$$\begin{aligned} & k_{p,i}^2 + (k_{d,i}\omega)^2 \\ & \leq (k_{p,i} - (1 + k_{d,i}h_d)\omega^2)^2 \\ & \quad + ((k_{d,i} + k_{p,i}h_d)\omega - \tau_i\omega^3)^2 \end{aligned} \quad (3.22)$$

Then we expand the square terms and reorganize the inequality (3.22) as:

$$\begin{aligned} & \tau_i^2\omega^4 + \left[ (1 + k_{d,i}h_d)^2 - 2\tau_i(k_{d,i} + k_{p,i}h_d) \right] \omega^2 - 2k_{p,i} + k_{p,i}^2h_d^2 \\ & \geq 0 \end{aligned} \quad (3.23)$$

To ensure inequality (3.23) is valid, we require following inequality to make the polynomial of  $\omega$  on the left-hand side having no real roots:

$$\left[ (1 + k_{d,i}h_d)^2 - 2\tau_i(k_{d,i} + k_{p,i}h_d) \right]^2 - 4\tau_i^2(-2k_{p,i} + k_{p,i}^2h_d^2) < 0 \quad (3.24)$$

The inequality (3.24) can be transformed into:

$$\begin{aligned} & (1 + k_{d,i}h_d)^2 \left[ (1 + k_{d,i}h_d)^2 - 4\tau_i(k_{d,i} + k_{p,i}h_d) \right] + 4\tau_i^2(k_{d,i}^2 \\ & \quad + 2k_{d,i}k_{p,i}h_d + 2k_{p,i}) < 0 \end{aligned} \quad (3.25)$$

from which we can obtain the condition of controller parameters to ensure string stability in ACC case:

$$\begin{aligned} & 4\tau_i(k_{d,i} + k_{p,i}h_d) \\ & > \frac{4\tau_i^2(k_{d,i}^2 + 2k_{d,i}k_{p,i}h_d + 2k_{p,i})}{(1 + k_{d,i}h_d)^2} + (1 + k_{d,i}h_d)^2 \end{aligned} \quad (3.26)$$

### 3.3 IFT optimization

#### 3.3.1 Probability of IFT degeneration

From (Qiu et al., 2012),  $P_d(\xi_d(\xi))$  is formulated as a contention model with saturated and unsaturated communication traffic using the Markov chain:

$$P_d(\xi_d(\xi)) = \prod_{i \in A_d(\xi)} p_{i,\text{unsat}} \prod_{i \in B_d(\xi)} (1 - p_{i,\text{unsat}}) \quad (3.27)$$

where  $\mathbf{A}_d(\xi_d(\xi))$  and  $\mathbf{B}_d(\xi_d(\xi))$  are the indices of vehicles with successful and unsuccessful send status, respectively. Specifically,  $\mathbf{A}_d(\xi_d(\xi)) = \{i | \eta_i = 1, \eta_{i,d} = 1, i = 0, \dots, N\}$  and  $\mathbf{B}_d(\xi_d(\xi)) = \{i | \eta_i = 1, \eta_{i,d} = 0, i = 0, \dots, N\}$ , where  $\eta_{i,d}$  is the sender status of vehicle  $i$  after IFT degeneration.

$p_{i,\text{unsat}}$  is the communication success rate of a sender vehicle  $i$  under unsaturated communication condition:

$$p_{i,\text{unsat}}(\xi) = [k_1 \log(\bar{\rho}_i(\xi)) + k_2 CW + k_3] p_{i,\text{sat}}(\xi) \quad (3.28)$$

where  $CW$  is the contention window size, and  $k_1, k_2, k_3$  are fitting coefficients obtained through linear regression in NS-3 numerical simulation (Wang et al., 2019).  $\bar{\rho}_i(\xi)$  is the average number of vehicles with activated send functionalities within the communication range  $R$  of vehicle  $i$ . With the average density  $\bar{k}$  of the ambient traffic flow, the average number of vehicles within communication range  $R$  can be calculated as  $m = R\bar{k}$ . Then, the vector  $\bar{\rho}(\xi) = [\bar{\rho}_0(\xi), \bar{\rho}_1(\xi), \dots, \bar{\rho}_N(\xi)]$  is expressed as:

$$\bar{\rho}(\xi) = \xi \mathbf{M}(\bar{k}) \quad (3.29)$$

where  $\mathbf{M}(\bar{k})$  is a  $N \times N$   $2m + 1$  diagonal matrix whose non-zero entries are 1 if  $m < N$ . Otherwise,  $\mathbf{M}$  is a  $N \times N$  matrix whose entries are all equal to 1.

$p_{i,\text{sat}}(\xi)$  is the success rate of a sender vehicle  $i$  in saturated communication condition:

$$p_{i,\text{sat}} = 2(1 - b_i)(1 - 2b_i + CW)^{-1} \quad (3.30)$$

where  $b_i$  is the busy rate of sender vehicle  $i$ :

$$b_i = 1 - e^{-\bar{\rho}_i(\xi) p_{i,\text{sat}}} \quad (3.31)$$

From Equations (3.30) and (3.31),  $p_{i,\text{sat}}$  can be solved using the numerical method proposed in (Qiu et al., 2012).

### 3.3.2 Performance metric

To factor both string stability and comfort, the control performance metric  $E_d(\xi_d(\xi))$  is extended to evaluate both traffic oscillations and smooth acceleration. As traffic oscillations can be measured by the fluctuations of vehicle speed (Li et al., 2012), and comfort is closely related to the jerk magnitude, the performance metric  $E_d(\xi_d(\xi))$  is formulated as the summation of the vehicle speed energy  $E_{V,i}$  and jerk energy  $E_{J,i}$  throughout the platoon:

$$E_d(\xi_d(\xi)) = \sum_{i=0}^N (E_{V,i} + E_{J,i}) \quad (3.32)$$

Correspondingly, the speed energy and jerk energy can be obtained by integrating the power spectral density (PSD) of vehicle speed  $V_i^2(j\omega)$  and the PSD of jerk  $J_i^2(j\omega)$  over the whole span of frequency  $\omega$  in the frequency domain, respectively:

$$E_{V,i} = \int_0^{+\infty} V_i^2(j\omega) d\omega \quad (3.33)$$

$$E_{J,i} = \int_0^{+\infty} J_i^2(j\omega) d\omega \quad (3.34)$$

As the information on ambient traffic conditions is usually obtained as vehicle trajectory data through vehicle-to-infrastructure communications under real-time implementation, an approach is needed to extract the speed energy and jerk energy from the vehicle trajectory data. First, the influence of ambient traffic oscillations is introduced into the platoon through the leading vehicle. Next, each vehicle in the platoon is connected to its predecessors, and the performance index of each vehicle in the platoon can be recursively traced back to that of the leading vehicle using SSTF (3.15) defined in Stability Analysis section. Then, we can use the frequency response of the leading vehicle's trajectory  $X_0(j\omega)$ , and the SSTF of each vehicle in the platoon to derive the performance index (i.e., speed fluctuation and jerk energy) for the whole platoon. The specific procedures are described hereafter in detail.

First, by performing the inverse Fourier transform for the trajectory frequency response  $X_i(j\omega)$  of vehicle  $i$ , the vehicle trajectory information can be derived in the time domain:

$$\begin{aligned} x_i(t) &= \int_0^{+\infty} X_i(j\omega) e^{2\pi t j \omega} d\omega \\ &= \int_0^{+\infty} SS_{X,i}(j\omega, \xi_d(\xi)) X_0(j\omega) e^{2\pi t j \omega} d\omega \end{aligned} \quad (3.35)$$

where  $X_0(j\omega)$  represents the trajectory oscillations of the leading vehicle  $i = 0$ , and  $SS_{X,i}(j\omega, \xi_d(\xi))$  is the SSTF describing the propagation of a traffic oscillation from the leading vehicle, as defined in the Stability Analysis section.

Second, the derivative of vehicle trajectory is used to obtain speed information in the time domain:

$$v_i(t) = \dot{x}_i(t) = \int_0^{+\infty} 2\pi j \omega SS_{X,i}(j\omega, \xi_d(\xi)) X_0(j\omega) e^{2\pi t j \omega} d\omega \quad (3.36)$$

The vehicle speed can be obtained from its frequency response  $V_i(j\omega)$  using the inverse Fourier transform:

$$v_i(t) = \int_0^{+\infty} V_i(j\omega) e^{2\pi t j \omega} d\omega \quad (3.37)$$

Then, since equations (3.36) and (3.37) are equivalent, we can extract  $V_i(j\omega)$  out as follows:

$$V_i(j\omega) = 2\pi j \omega SS_{X,i}(j\omega, \xi_d(\xi)) X_0(j\omega) \quad (3.38)$$

Similarly, the third-order derivative of vehicle trajectory can be used to obtain the jerk in the time domain:

$$J_i(t) = x_i^{(3)}(t) = - \int_0^{+\infty} 8\pi^3 j \omega^3 SS_{X,i}(j\omega, \xi_d(\xi)) X_0(j\omega) e^{2\pi t j \omega} d\omega \quad (3.39)$$

Then, we compare it to the equivalency obtained from inverse Fourier transform to obtain  $J_i(j\omega)$ :

$$J_i(j\omega) = -8\pi^3 j\omega^3 SS_{X,i}(j\omega, \xi_d(\xi))X_0(j\omega) \quad (3.40)$$

Using equations (3.32), (3.33), (3.34), (3.38) and (3.40), the platoon control performance metric  $E_d(\xi_d(\xi))$  is expressed as:

$$\begin{aligned} E_d(\xi_d(\xi)) &= \sum_{i=0}^N \int_0^{+\infty} (V_i^2(j\omega) + J_i^2(j\omega)) d\omega \\ &= \sum_{i=0}^N \int_0^{+\infty} (4\pi^2 \omega^2 \\ &\quad + 64\pi^6 \omega^6) SS_{X,i}^2(j\omega, \xi_d(\xi)) X_0^2(j\omega) d\omega \end{aligned} \quad (3.41)$$

Remark 1: The first-layer optimization is solved using the two-step algorithm in (Wang et al., 2019). The period of updating optimal IFT depends on the oscillations in ambient traffic and platoon length. Once the PSD of leading vehicle trajectory changes appreciably (i.e., changes of oscillation magnitude and oscillation frequency), or some vehicles leave or join in the platoon, the first-layer IFT optimization will be performed and generate a new optimal IFT. Moreover, as mentioned in (Li et al., 2010), the invariant-pattern of traffic oscillations usually persists around 10 minutes, indicating a 10-minute interval could be a potential selection in real world implementation.

### 3.4 Controller parameter optimization

Though the first-layer IFT optimization improves the robustness of V2V communications to reduce the frequency of controller switching, IFT dynamics are inevitable in real-time traffic. Thus, the switching control based CACC shown in Fig. 3.3, which can adaptively switch controllers according to the IFT dynamics, is necessary for acceptable control performance (Gong et al., 2019). To achieve smooth acceleration profile for riding comfort as well as string stability, a linear quadratic method is implemented in the second-layer optimization to update controller feedback gains  $k_{p,i}(k)$ ,  $k_{d,i}(k)$ , and feedforward gains  $k_{f,1}(k)$ ,  $k_{f,2}(k)$  for vehicle  $i$  at each time step  $k$ , such that vehicle acceleration can be throttled in a comfortable range while maintaining string-stable tracking (i.e., the spacing error and speed tracking error can be minimized upstream the platoon). To perform controller switching and realize real-time implementation, the control inputs and vehicle dynamics are discretized using zero-order hold method as described in (Gong et al., 2019). Correspondingly, the optimization model for controller parameters is formulated as:

$$\begin{aligned} \min_{k_{p,i}, k_{d,i}, k_{f,1}, k_{f,2}} \text{OBJ}(k) &= \Phi_{i,1}(k)^T \alpha(k) P \Phi_{i,1}(k) + \Phi_{i,2}(k)^T \beta(k) P \Phi_{i,2}(k) \\ &\quad + Q(a_i(k+1) - a_i(k))^2 \end{aligned} \quad (3.42)$$

$$\text{s.t.} \quad \bar{X}_i(k+1) = A_i \bar{X}_i(k) + B_i u_i(k) \quad (3.43)$$

$$u_i(k) = \alpha(k) K(k)^T \Phi_{i,1}(k) + \beta(k) K(k)^T \Phi_{i,2}(k) + \alpha(k) u_{f,i-1}(k) + \beta(k) u_{f,i-2}(k) \quad (3.44)$$

$$k_{p,\min} \leq k_{p,i}(k) \leq k_{p,\max} \quad (3.45)$$

$$k_{d,min} \leq k_{d,i}(k) \leq k_{d,max} \quad (3.46)$$

$$k_{f,min} \leq k_{f,1}(k) \leq k_{f,max} \quad (3.47)$$

$$k_{f,min} \leq k_{f,2}(k) \leq k_{f,max} \quad (3.48)$$

where  $\Phi_{i,l}(k) = \Xi_{i-l}(k+1) - \Xi_i(k+1) - lh_d \dot{\Xi}_i(k+1)$ ,  $l \in \{1,2\}$ ,  $\Xi_i(k) = [x_i(k), v_i(k)]^T$ ,  $\dot{\Xi}_i(k) = [v_i(k), a_i(k)]^T$  is used to formulate spacing error and speed tracking error between vehicle  $i$  and its  $l$ th predecessor.  $\bar{X}_i(k) = [x_i(k), v_i(k), a_i(k)]^T$  is the state vector of vehicle  $i$  at

time step  $k$ ,  $A_i = \begin{bmatrix} 1 & dt & 0.5dt^2 \\ 0 & 1 & dt \\ 0 & 0 & \frac{dt}{\tau_i + dt} \end{bmatrix}$ , and  $B_i = \begin{bmatrix} 0 \\ 0 \\ \frac{dt}{\tau_i + dt} \end{bmatrix}$  are the state matrices of discrete vehicle

dynamics,  $P = \begin{bmatrix} P_{11} & 0 \\ 0 & P_{22} \end{bmatrix}$  is the diagonal weighting matrix for spacing error and speed tracking error, and  $Q$  denotes the weighting coefficients for jerk,  $\alpha(k)$  and  $\beta(k)$  are indicator values defined in the section of Controller Structure. Increasing  $P_{11}$  ( $P_{22}$ ) implies more penalty on spacing error (speed tracking error), while increasing  $Q$  indicates more emphasis on riding comfort (i.e., jerk minimization).  $dt$  is the sampling period.  $K(k) = [k_{p,i}(k), k_{d,i}(k)]^T$  is the vector of controller gains.  $u_{f,i-l}(k)$ ,  $l \in \{1,2\}$  is the discretized feedforward input:

$$u_{f,i-l}(k) = \frac{dt}{dt + lh_d} \left[ k_{f,l}(k) \left( \frac{\tau_i + dt}{dt} a_{i-l}(k) - \frac{\tau_i}{dt} a_{i-l}(k-1) \right) + \frac{lh_d}{dt} u_{f,i-l}(k-1) \right], l \in \{1,2\} \quad (3.49)$$

The last term of the objective function (3.42) is associated with jerk minimization, while the first two terms are related to the spacing error and speed tracking error with respect to two predecessors, respectively. Constraint (3.43) is the discrete vehicle dynamics model describing changes in the vehicle states. Constraint (3.44) is the control command for CAVs in the platoon. Constraints (3.45) to (3.48) are the upper and lower bounds of controller feedforward and feedback gains for achieving desirable local stability, string stability performance.

Remark 2: The second-layer optimization is formulated in a standard Quadratic Programming (QP) form, which can be solved efficiently using existed QP solvers and algorithms.

### 3.5 State estimation and Kalman predictor

In this section, the Kalman filter is applied as the third smoothing strategy to estimate the states of preceding vehicles to counteract the negative effects of measurement noise and acceleration disturbance. Further, with the prediction of vehicle acceleration from the Kalman predictor, in some situations, even though some V2V communication links are broken due to communication failure, we can reconstruct CACC from ACC to enhance control performance.

#### 3.5.1 Kalman filter structure

The Kalman filter is implemented based on the discretized longitudinal vehicle dynamics

model considering measurement noise  $\mathcal{E}(k)$  and input disturbance  $w(k)$ :

$$\bar{X}_i(k+1) = A_i \bar{X}_i(k) + B_i u_i(k) + B_w w(k) \quad (3.50)$$

$$y_i(k) = C_i \bar{X}_i(k) + \mathcal{E}(k) \quad (3.51)$$

in which  $A_i$ ,  $B_i$ , and  $\bar{X}_i(k)$  are defined in the section of Controller Parameter Optimization,  $B_w = [0 \ 0 \ dt]^T$ ,  $C_i = \begin{bmatrix} 1 & 0 & 0 \\ 0 & 1 & 0 \end{bmatrix}$  is the output matrix of vehicle  $i$  at time step  $k$ ,  $y_i(k) = [x_i(k), v_i(k)]^T$  is the output vector that can be directly measured by onboard sensors of the following vehicles,  $\mathcal{E}(k) = [\mathcal{E}_x(k), \mathcal{E}_v(k)]^T$  is the measurement noise vector,  $\mathcal{E}_x(k)$  is the noise in position measurement,  $\mathcal{E}_v(k)$  is the noise in speed measurement,  $w(k)$  is the vehicle acceleration disturbance induced by uncertainties (e.g., impact of road grade, unprecise throttle response). We assume that  $\mathcal{E}_x(k) \sim \mathcal{N}(0, \sigma_x)$ ,  $\mathcal{E}_v(k) \sim \mathcal{N}(0, \sigma_v)$ ,  $w(k) \sim \mathcal{N}(0, \sigma_a)$  are all independent zero-mean Gaussian distributed random variables with known variance (Ploeg et al., 2015). In a homogeneous CAV platoon,  $A_i$ ,  $B_i$ ,  $C_i$ ,  $\sigma_a$ ,  $\sigma_x$ , and  $\sigma_v$  are assumed to be identical for all CAVs in the platoon.

The Kalman filter estimation consists of two steps. The first step is called a priori estimation:

$$\hat{X}_i(k+1|k) = A_i \hat{X}_i(k|k) + B_i u_i(k) \quad (3.52)$$

where  $\hat{X}_i(k+1|k) = [x_i(k+1|k), v_i(k+1|k), a_i(k+1|k)]^T$ , the prior estimated state vector of vehicle  $i$  for next time step  $k+1$ , is predicted based on vehicle dynamics model (3.43), with the control input  $u_i(k)$  at current time step  $k$ .

The second step is called a posteriori estimation:

$$\begin{aligned} \hat{X}_i(k+1|k+1) &= A_i \hat{X}_i(k+1|k) \\ &+ L_{KF,i}(k+1) [y_i(k+1) - C_i \hat{X}_i(k+1|k)] \end{aligned} \quad (3.53)$$

in which the posterior estimated state vector  $\hat{X}_i(k+1|k+1)$  is corrected from  $\hat{X}_i(k+1|k)$  by applying optimal Kalman gain  $L_{KF,i}(k+1)$  to minimize the difference between actual measurement  $y_i(k+1)$  and estimated output  $\hat{y}_i(k+1|k) = C_i \hat{X}_i(k+1|k)$  of vehicle  $i$  at next time step  $k+1$ .

The optimal Kalman gain is calculated as follows:

$$L_{KF,i}(k+1) = M_i(k+1) C_i^T (C_i M_i(k+1) C_i^T + \mathcal{E})^{-1} \quad (3.54)$$

Where:

$$M_i(k+1) = A_i Z_i(k) A_i^T + B_w W B_w^T \quad (3.55)$$

$$Z_i(k) = (I_{2 \times 2} - L_{KF,i}(k) C_i) M_i(k) \quad (3.56)$$

$M_i(k)$  is covariance matrix of estimation error at time step  $k$ , and  $Z_i(k)$  is the estimation error at time step  $k$ . From (3.54)-(3.56), with the statistical information of measurement noise and input disturbance, the optimal Kalman gain can be calculated offline to improve the efficiency of real-time estimation process.

Remark 3: The estimated vehicle states  $\hat{X}_i(k+1|k)$  will be used to derive the tracking error  $E(s)$ , speed tracking error  $\dot{E}(s)$ , and vehicle accelerations (i.e.,  $\ddot{X}_{i-1}(s)$ ,  $\ddot{X}_{i-2}(s)$ ) in the

control input (3.6), such that the smoothness of car-following behaviors can be improved.

### 3.5.2 Kalman predictor and CACC reconstruction

With proper adjustment of time index  $k$  in (3.52), (3.53), and (3.54), we can derive the formula for the Kalman predictor.

$$\begin{aligned} \hat{X}_i(k+1|k+1) &= A_i \hat{X}_i(k|k) + B_i u_i(k) + L_{KF,i}(k \\ &+ 1) [y_i(k+1) - C_i (A_i \hat{X}_i(k|k) + B_i u_i(k))] \end{aligned} \quad (3.57)$$

With the application of Kalman predictor, once vehicle  $i$  obtains the control command  $u_{i-1}(k)$  ( $u_{i-2}(k)$ ) via V2V communication at time step  $k$ , and the position and speed measurements  $y_{i-1}(k+1)$  ( $y_{i-2}(k+1)$ ) via onboard sensors at time step  $k+1$  from the preceding vehicle  $i-1$  ( $i-2$ ), it can estimate the acceleration rate  $a_{i-1}(k+1)$  ( $a_{i-2}(k+1)$ ) of the preceding vehicle  $i-1$  ( $i-2$ ) at time step  $k+1$  to reconstruct the CACC scenarios. If the CACC reconstruction is feasible, the indicator values corresponding to specific controller set will be updated at time step  $k$ , such that the control input (3.6) of vehicle  $i$  is reformulated into CACC mode as well. Table 3.2 presents the potential scenarios of CACC reconstruction.

Specifically, if vehicle  $i$  is controlled under CACC1 at time step  $k$ , then it can obtain vehicle states  $\bar{X}_{i-1}(k)$ ,  $\bar{X}_{i-2}(k)$  and control commands  $u_{i-1}(k)$ ,  $u_{i-2}(k)$  from vehicles  $i-1$  and  $i-2$ . Then, at time step  $k+1$ : (i) If CACC1 degrades to CACC2 (the communication link between vehicle  $i$  and vehicle  $i-2$  breaks), vehicle  $i$  can still obtain all vehicle states  $\bar{X}_{i-1}(k+1)$  of vehicle  $i-1$  (through CACC2). As vehicle  $i-1$  can send position and speed measurements of vehicle  $i-2$  to vehicle  $i$  via V2V communications, vehicle  $i$  can estimate the acceleration rate of vehicle  $i-2$  using (3.57) to reconstruct CACC1. (ii) If CACC1 degrades to CACC3 (the communication link between vehicle  $i$  and vehicle  $i-1$  breaks), vehicle  $i$  can measure the position and speed of vehicle  $i-1$  via onboard sensors, and estimate the acceleration information of vehicle  $i-1$  using (3.57) to reconstruct CACC1. (iii) If CACC1 degrades to ACC (both communication links break), vehicle  $i$  can still estimate the acceleration of vehicle  $i-1$  using (3.57) based on the measurement  $y_{i-1}(k+1)$ . However, the acceleration of vehicle  $i-2$  cannot be estimated due to the absence of speed and position measurements from vehicle  $i-2$ .

Table 3.2. Scenarios of CACC reconstruction

Time step $k$	Time step $k+1$	
Control method	Possible degeneration	Reconstructed CACC
CACC1	CACC2	CACC1
	CACC3	CACC1
	ACC	CACC2
CACC2	ACC	CACC2
CACC3	ACC	ACC

If vehicle  $i$  is controlled under CACC2 at time step  $k$ , it can obtain the control command  $u_{i-1}(k)$  from vehicle  $i - 1$ . At time step  $k + 1$ , if CACC2 degrades to ACC, vehicle  $i$  can still obtain the position and speed of vehicle  $i - 1$  via onboard sensors, and then using (3.57) estimate the acceleration information of vehicle  $i - 1$  to reconstruct CACC2.

If vehicle  $i$  is controlled under CACC3 at time step  $k$ , then it can obtain the control command  $u_{i-2}(k)$  from vehicle  $i - 2$ . At time step  $k + 1$ , if CACC3 degrades to ACC, since vehicle  $i$  has neither the information of control input from vehicle  $i - 1$  nor the measurement of position and speed from vehicle  $i - 2$ , CACC reconstruction is infeasible.

### 3.6 Numerical experiments

#### 3.6.1 Experiment setup

This section presents three numerical experiments to illustrate the performance of the proposed CACC-SOIFT. The first experiment analyzes the performance of CACC-SOIFT in terms of maintaining string stability and smooth acceleration profile in the environment of dynamic IFT with sensor measurement noise and errors. To showcase the effectiveness of the three smoothing strategies, the second experiment compares the control performance of the proposed CACC-SOIFT to three cases of CACC: case (a) without the IFT optimization, case (b) without the controller parameter optimization, and case (c) without the Kalman predictor, where each case removes one smoothing strategy while retaining the other two. The third experiment illustrates the critical effects of time headway selection in the platoon control process.

The platoon considered is a 12-CAV platoon with one leading CAV ( $i = 0$ ) and 11 following CAVs. The movement of the leading CAV for all experiments is obtained from NGSIM field data (NGSIM, 2007), which contains a 4-minute vehicle trajectory collected on eastbound I-80 at Emeryville, San Francisco, California, from 4:00pm to 4:15pm. We excluded the abnormal accelerations beyond the range of  $[-6, 4]$ , and removed the choppy acceleration profile induced by measurement error. For the first two experiments, the desired time headways  $h_d$  are set as  $h_d = 1s$ , while in the last experiment, time headway are set to be 0.5s, 1s, and 2s, respectively, to evaluate the influence of time headway selection. The identical time headway is utilized throughout the platoon to prevent additional difference in controller transient response, which enables uniform traffic flow. The initial conditions for numerical experiments are: (i) initial acceleration of all CAVs in the platoon is  $a_i(0) = 0m/s^2$ ; (ii) initial speed of all CAVs in the platoon is  $v_i(0) = 25m/s$ ; (iii) initial spacing between adjacent CAVs is  $x_{i-1}(0) - x_i(0) = h_d v_i(0) + L_i$ , in which  $L_i$  is the length of CAV  $i$ , and  $L_i$  is set as 5m for all CAVs. The sampling time  $dt = 0.1s$  for both experiments. The update interval of the IFT optimization is set to 1 minute to ensure the optimal IFT is corresponding to the potential changes of ambient traffic. We set  $P = I_{2 \times 2}$ ,  $Q = 4$  for more emphasis and penalty on comfort. For the constraints of controller parameters, we set  $k_{p,min} = 0.5$ ,  $k_{p,max} = 1.5$ ,  $k_{d,min} = 0.3$ ,  $k_{d,max} = 1.2$ ,  $k_{f,min} = 0$ ,  $k_{f,max} = 1$ ,  $\alpha = 0.7$ , and  $\beta = 0.3$  by referring to Equation (3.12)-(3.14), Equation (3.20) and Equation (3.26). Note that we also applied the trial and error method to construct a feasible region for ensuring desired string stability and comfort performance. The parameter settings of vehicle inertial delay, measurement noise, and acceleration disturbance are according to the numerical experiment in (Ploeg et al., 2015):  $\tau_i =$

$0.1s$ ,  $\sigma_x = 0.17m$ ,  $\sigma_v = 0.13m/s$ , and  $\sigma_a = 0.1m/s^2$ .

While the controller parameters of CACC-SOIFT, case (a), and case (c) are determined at each time step based on the second-layer controller parameter optimization model, the controller parameters of case (b) are set as the average values of controller parameters in CACC-SOIFT. To simulate the environment of dynamic IFT, the V2V communication success rate is calibrated using network simulator NS-3 based on the contention model described in the section of Probability of IFT Degeneration, and the calibration process is the same as our previous experiment (Wang et al., 2019). In the calibrated model, the communication success rate will decrease if the density of CAVs with activated “send” functionality in communication range increases.

### **3.6.2 Experiment results**

The optimal IFTs obtained from the first-layer IFT optimization is  $\xi = [1,1,1,1,0,0,0,1,1,1,0,0]$  for the first minute,  $\xi = [1,1,1,1,1,0,0,1,1,1,0,0]$  for the second minute,  $\xi = [1,1,1,1,0,0,0,1,1,1,0,0]$  for the third minute, and  $\xi = [1,1,1,1,0,0,0,1,1,1,0,0]$  for the last minute.

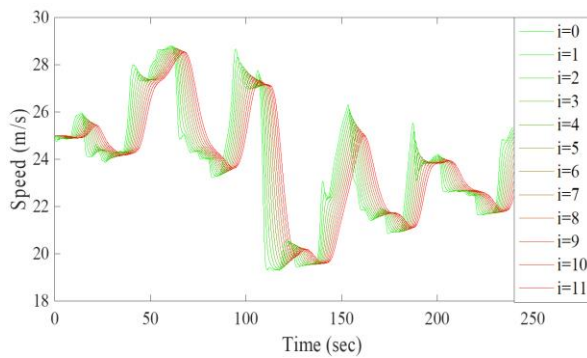
The first experiment tests the string stability of the CAV platoon and the smoothness of vehicle acceleration under the influence of dynamic IFT and measurement noise. Figures 3.4(a) and 3.4(b) show the speed profile and acceleration profile of all vehicles in the platoon, respectively.

Related to the first experiment, Fig. 3.4(a) illustrates that fluctuations of vehicle speed triggered by the abrupt acceleration/deceleration of leading vehicle are sequentially attenuated in the upstream of the platoon, reflecting acceptable string stability performance. In Fig. 3.4(b), the acceleration profiles of all vehicles are smooth compared to the choppy acceleration profiles (in the left corner) generated from CACC-DIFT (Gong et al., 2019) under the effect of measurement noise and uncared parameter settings, indicating that abrupt changes in acceleration are mitigated by CACC-SOIFT. Also, as shown in Fig. 3.4(c), the maximum values of jerk of all following vehicles in the platoon are well below the uncomfortable value of  $\pm 0.3m/s^3$  based on a public surveys (Hoerock, 1977). Additionally, as illustrated in Fig. 3.4(d), the  $\infty$ -norm of vehicle trajectory, speed, and acceleration all decrease sequentially upstream of the platoon, indicating the desired string stability property and attenuated traffic oscillations. Hence, even with the existence of dynamic IFT and contaminated vehicle kinematic states, CACC-SOIFT can still achieve the desired performance of string stability and riding comfort.

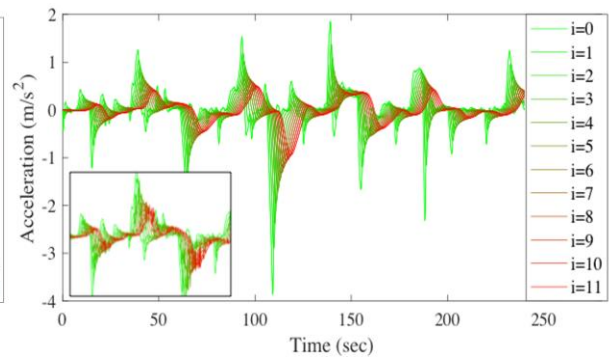
The second experiment compares the proposed CACC-SOIFT to the CACC cases of removing one of the three smoothing strategies at a time. Figures 3.5(a) and 3.5(b) show that, compared to CACC-SOIFT, the other three CACC cases have larger mean values of jerk magnitude and greater standard deviation (STD) of speed fluctuations throughout the platoon, indicating poorer performance in terms of comfort and string stability. Note that in case (b), the mean value of jerk increases substantially for 6th ( $i = 5$ ) and 12th ( $i = 11$ ) vehicles, while the STDs of vehicle speed fluctuations increase appreciably after the 6th vehicle. This phenomenon can be explained as: the predecessors of 6th and 12th vehicles deactivate their send functionalities for most of the time due to IFT optimization, which triggers ACC for both vehicles. Thereby, the control performance deteriorates as the parameter optimization is not performed. The

results show that all three strategies in CACC-SOIFT are essential to improve string stability and riding comfort.

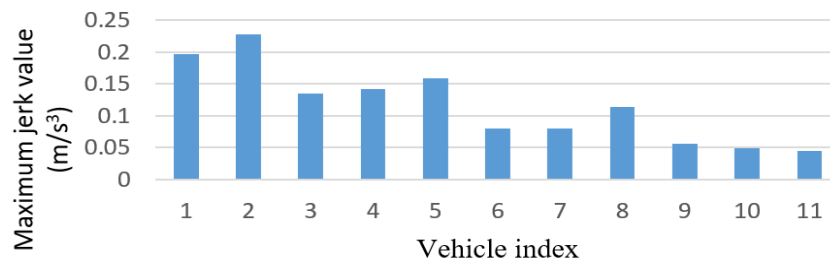
The third experiment sheds some light on the time headway selection. As shown in Fig. 3.6(a) and 6(b), the mean of jerk magnitude corresponding to the platoon with smaller time headway envelops the platoon with greater time headway, and the standard deviation of vehicle speed referring to the platoon with smaller time headway also bounds the platoon with greater time headway. The results indicate that smaller headway selection will induce greater jerks and more speed fluctuations, jeopardizing the control performance regarding to string stability and riding comfort, thereby, a proper selection of time headway is significant for the real-world application.



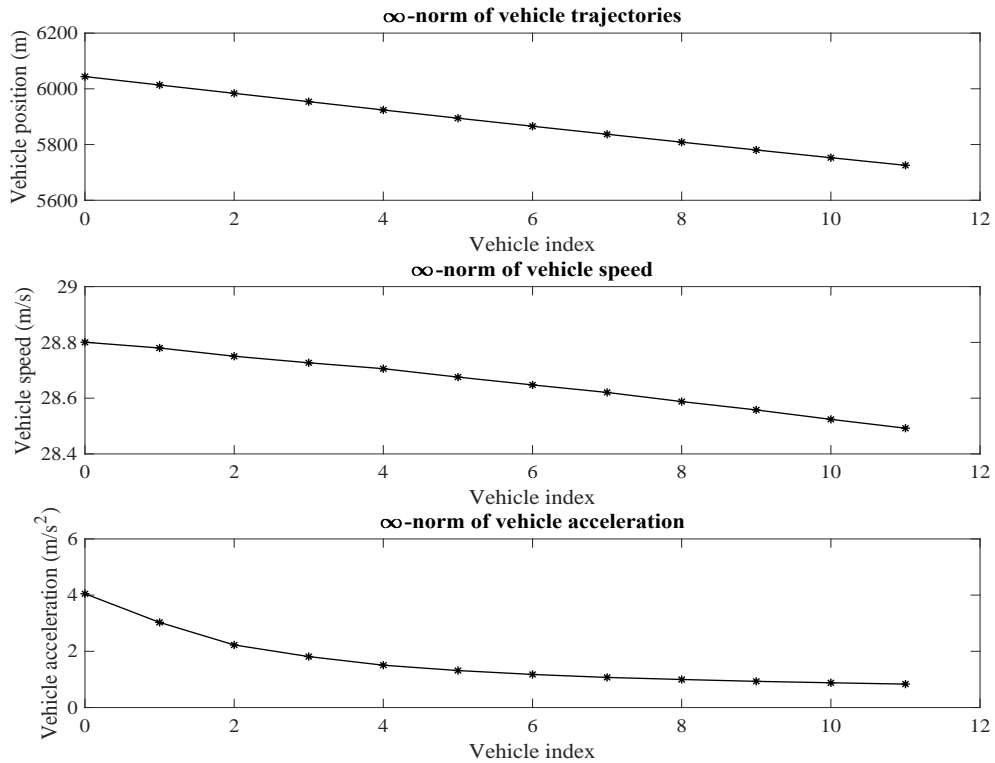
(a). Vehicle speed profile



(b). Vehicle acceleration profile

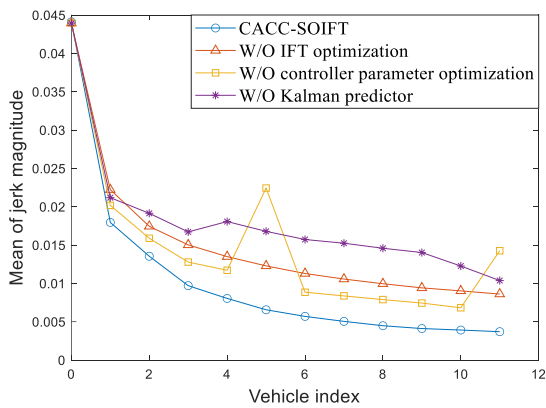


(c). Maximum value of vehicle jerk

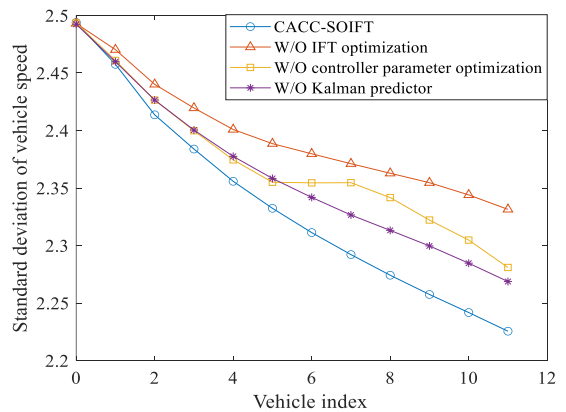


(d).  $\infty$ -norm of vehicle states

Figure 3.4. Performance of the CACC-SOIFT

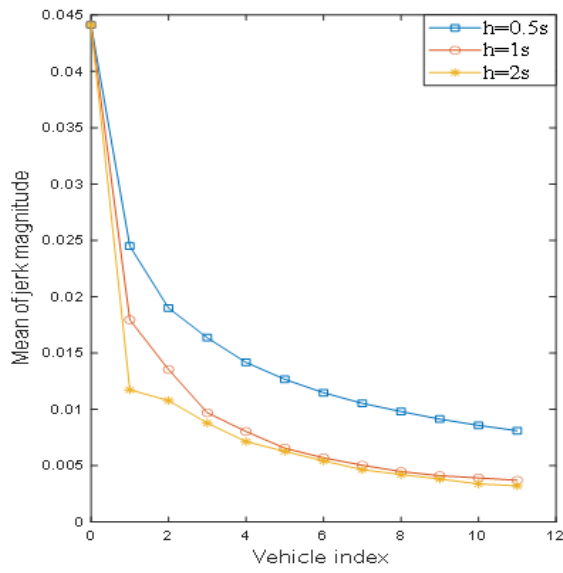


(a). Mean value of jerk

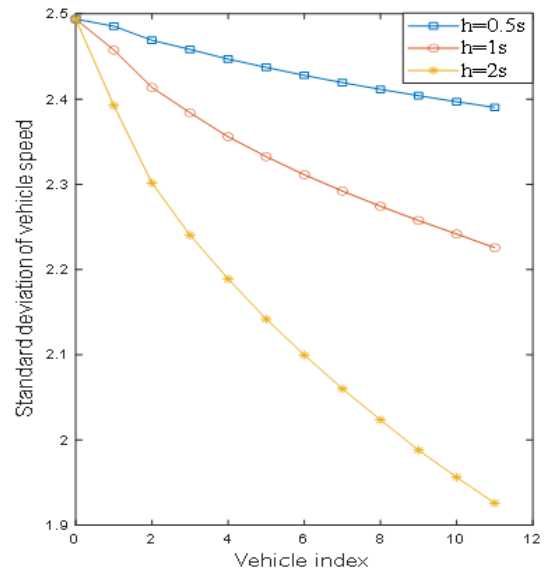


(b). Standard deviation of vehicle speed

Figure 3.5. Comparisons of different CACC cases



(a). Mean value of jerk



(b). Standard deviation of vehicle speed

Figure 3.6. Comparisons of different headway selections in CACC-SOIFT

#### **4. A REAL-TIME DEPLOYABLE MODEL PREDICTIVE CONTROL-BASED COOPERATIVE PLATOONING APPROACH FOR CONNECTED AND AUTONOMOUS VEHICLES**

##### **4.1 Introduction**

Connected and autonomous vehicle (CAV) technologies provide disruptive and transformational opportunities for innovations toward intelligent transportation systems. Unlike human-driven vehicles, CAVs have shorter reaction times, better knowledge of ambient traffic (in terms of speed, position, acceleration, etc.), and faster information processing speeds. These characteristics enable CAVs to form platoons to drive cooperatively on the road, in which a vehicle maintains a small and nearly constant headway with its preceding vehicle. Past studies suggest that vehicle platooning of CAVs can benefit transportation systems in many ways (Jia et al., 2015). It can increase road capacity, reduce energy consumption and tailpipe emissions, and facilitate vehicle-to-vehicle based applications (involving data sharing and dissemination) due to the relatively fixed positions of vehicles within a platoon.

In the literature, many adaptive cruise control (ACC) models and cooperative ACC (CACC) models have been proposed to control longitudinal car-following behavior of vehicles to enable efficient vehicle platooning. The ACC makes car-following decisions based on the preceding vehicle's information (speed and position) obtained through onboard sensors (e.g., VanderWerf et al., 2001; Hasebe et al., 2003; Kesting et al., 2008; Darbha and Rajagopal, 1999), while CACC makes car-following decisions with more information (speed, position and/or acceleration) from either a single vehicle or multiple vehicles in the platoon by leveraging connectivity technologies. The CACC models can improve the stability and efficiency of the ACC models by reducing the delay in responding to the preceding vehicle. According to Wang et al. (2014b), CACC models can be divided into two categories, the cooperative sensing-based models and the cooperative behavior-based models. The cooperative sensing-based models seek to optimize individual vehicle's performance using, for example, the immediate preceding vehicle's information (with acceleration) (Rajamani, R., Shladover, S.E. 2001, Desjardins and Chaib-draa, 2011), multiple preceding vehicles' information (Li et al., 2011; Jia and Ngoduy, 2016; Ge and Orosz, 2014; Ploeg et al., 2014) or the preceding-and-following vehicles' information (Zheng et al., 2016; Nakayama et al., 2001). It is important to note that the behaviors of vehicles controlled by these models are non-cooperative. That is, the control is not based on viewing a group of vehicles as an integrated system, which can deteriorate system (platoon) performance in terms of safety, mobility, energy consumption, etc.

To bridge this gap, recently, cooperative behavior-based CACC models have been proposed to coordinate the behaviors (accelerations or decelerations) of all of the following vehicles in a CAV platoon (e.g., Wang et al., 2014a; Zhou et al., 2017; Gong and Du, 2018). Most of these models are developed by leveraging the model predictive control (MPC) cooperative control approach. The MPC approach incorporates an optimal control problem to optimize the control decisions of the following vehicles in the platoon for some future period (labeled prediction horizon) to maximize the platoon performance based on the vehicles' state information at the current time. It has the flexibility to deal with multiple design criteria and constraints on state and control variables. Wang et al. (2014a) propose a MPC approach to coordinate the behaviors of all CAVs in a platoon to optimize a cost function reflecting different control objectives. Numerical applications illustrate

that this approach can lead to smoother deceleration behavior and more responsive and agile acceleration behavior compared to non-cooperative controllers. Zhou et al. (2017) extend Wang et al. (2014a) by addressing the impacts of uncertainty in both system dynamics and sensor measurements on vehicle control. They propose a discrete Kalman filter to estimate the system state and a stochastic MPC approach to determine the optimal control. Gong and Du (2018) apply the MPC approach to coordinate multiple CAV platoons separated by human driven vehicles to enhance the smoothness and stability of the mixed flow platoon. Wang et al. (2019) provide a detailed review of the recent CAV trajectory control methods.

While the aforementioned MPC-based cooperative control strategies can coordinate the car-following behaviors of CAVs in a platoon effectively, their real-time deployability requires that at each sampling time instant, the group of CAVs solve the embedded optimal control problem instantaneously (i.e., in much less than 0.1 seconds) to obtain the vehicles' control decisions based on their detected states (e.g., speed and positions) at that instant. These decisions then need to be executed to control the CAV platoon at the sampling time instant with no delay. However, this requirement cannot be satisfied in practice due to the computational time required by the CAVs to solve the optimal control problem. As pointed by Zhou et al. (2017), the computational time for solving the optimal control problem increases monotonically with the number of vehicles in the platoon and the prediction horizon. It can become intractable in real traffic systems due to the expansion of the dimensionality of state and control input spaces (Wang et al., 2016). Thereby, based on platoon size and prediction horizon length, the computational time of the optimal control problem can cause significant delay (labeled control delay) in the execution of the optimal control decisions for the CAV platoon. As the CAVs' states change dynamically, the control delay can significantly deteriorate performance and even induce vehicle collisions. This precludes these MPC-based cooperative control strategies for a CAV platoon from being applied in real-time.

Some recent studies have sought to reduce the control delay induced by the computational time to solve the optimal control problem embedded in MPC-based cooperative control strategies. Wang et al. (2016) propose a decentralized MPC strategy which considers cooperation among only two vehicles in a decoupled platoon system, which reduces the computational time substantially as only two vehicles' control decisions are optimized simultaneously. However, the performance of the CAV platoon cannot be enhanced to the fullest under this strategy as only two vehicles' behaviors are coordinated at the same time under a common objective. Further, the computational time for solving the optimal control problem can increase with the prediction horizon for even the decoupled platoon system. Gong and Du (2018) propose a distributed solution algorithm to reduce computational time by distributing the computational tasks among all CAVs in the platoon. However, the computational time of this algorithm can increase dramatically with platoon size and prediction horizon. Hence, these methods (e.g., Wang et al., 2016; Gong and Du, 2018) alleviate the issue of control delay of MPC-based cooperative control strategies to only a certain extent, but are still limited by platoon size and/or prediction horizon.

This study develops two real-time deployable MPC-based approaches that address the issue of the control delay at a fundamental level. In this study, the phrase "real-time deployable" refers to the capability that these approaches can overcome the control delay issue and can provide the optimal control decisions for all following vehicles in the platoon instantaneously at each sampling time instant. To do so, first, an idealized MPC-based cooperative control strategy is proposed by modifying the strategies proposed by Wang et al. (2014a) and Zhou et al. (2017). It can coordinate

the behavior of all of the following CAVs in the platoon to maneuver them efficiently and safely on the idealized assumption that the embedded optimal control problem can be solved instantaneously. To relax this assumption, two deployable approaches, labeled the deployable MPC (DMPC) approach and the DMPC with first-order approximation (DMPC-FOA) approach, are proposed to address the issue of computational delay associated with solving the optimal control problem in the idealized MPC-based strategy. It should be noted that to enable efficient coordination of the car-following behaviors of all CAVs in the platoon, such approaches need to accurately characterize the optimal control decisions of the idealized MPC-based strategy.

The DMPC approach reserves sufficient time before each sampling time instant to solve the optimal control problem so that the optimal control decisions can be obtained in advance to be executed at the corresponding sampling time instant with no delay. However, as the leading vehicle of a platoon needs to respond to the dynamics of the vehicles downstream of it, its behavior cannot be controlled and coordinated with those of the following vehicles in the platoon. Thereby, its position and speed at each sampling time instant need to be predicted ahead of that time, which is determined by the time reserved for computing. Hence, the optimal control decisions of the DMPC approach can deviate from that of the idealized MPC strategy due to error in predicting the leading vehicle's position and speed in advance. To address this problem, the DMPC-FOA approach is proposed to more accurately characterize the optimal control decisions of the idealized MPC strategy. Before each sampling instant, the DMPC-FOA approach reserves sufficient time to determine not only the optimal control decisions using the leading vehicle's predicted position and speed at the sampling time instant, but also the derivatives of the estimated optimal control decisions with respect to the leading vehicle's position and speed. Thereby, at the sampling time instant when the leading vehicle's actual position and speed are detected, the first-order Taylor approximation method can be applied to correct the estimated optimal control decisions for the following vehicles. Numerical experiments illustrate that the DMPC-FOA approach can address the issue of control delay while accurately estimating the optimal control decisions of the idealized MPC strategy.

The contributions of this study are fivefold. First, an idealized MPC strategy is proposed to coordinate the behaviors of the following vehicles in the platoon by modifying the control strategies proposed by Wang et al. (2014a) and Zhou et al. (2017). Further, a solution algorithm is proposed to solve the optimal control problem with both control constraints and pure state constraints in the idealized MPC strategy. A two-point boundary value problem is derived based on the necessary conditions for optimality to obtain the optimal control decisions to coordinate the behaviors of all vehicles in the platoon to maximize the platoon performance. Second, the study develops the DMPC-FOA approach that simultaneously addresses the control delay issue while accurately characterizing the optimal control decisions of the idealized MPC strategy. Thereby, it can be applied in real-time to efficiently coordinate the car-following behaviors of all CAVs in a platoon. Third, the method for sensitive analysis of the optimal control problem is analytically formulated. It can quantitatively measure the impact of parametric perturbations (e.g., perturbations of initial state of the leading vehicle) on the optimal control decisions and the platoon performance. Fourth, this study shows analytically that the derivatives of the optimal control decisions with respect to the parametric perturbations are the same when the inequality constraints in the proposed optimal control problem (e.g., acceleration range constraints, speed range constraints, spacing headway constraints) are inactive in some traffic scenarios (e.g., uncongested traffic flow with mild acceleration and deceleration behavior of the leading vehicle). These results can be used as the initial point in the algorithm to solve for these derivatives faster when the constraints in the optimal

control problem are active in certain traffic scenarios (e.g., very congested flow). This enhances the real-time application of the proposed method. Fifth, an analytical method is provided for stability analysis of the idealized MPC strategy. It helps to identify the inputs of the parameters in the idealized MPC strategy to better dampen the oscillations in the platoon.

It is important to note that this study is fundamentally different from that of Wang et al. (2018b), which discusses a compensation strategy for sensor delay and actuator lag. The compensation strategy can account for the differences between the sensed kinematic states of all following vehicles and the actual ones at the sampling time instant by leveraging the optimal control decisions for all following vehicles in the last control cycle. However, in their study, the computational time for solving the optimal control problem is neglected. Thereby, they do not study the impacts of the prediction error of the leading vehicle's state at the sampling time instant on the optimal control decision. Note that the leading vehicle's behavior cannot be controlled. Thereby, unlike for the following vehicles in the platoon, the deviation between the predicted leading vehicle's state and the actual one at the sampling time instant cannot be compensated using the method proposed in Wang et al. (2018b).

The remainder of this paper is organized as follows. The next section provides the analytical formulation of the idealized MPC cooperative control strategy for a CAV platoon and discusses the framework for the DMPC and DMPC-FOA approaches. Section 4.3 introduces the solution algorithm to solve the optimal control problem in the idealized MPC strategy. The method for the sensitivity analysis of the optimal control problem is presented in Section 4.4. Section 4.5 discusses the conditions for the stability of the idealized MPC strategy without inequality constraints. Section 4.6 discusses results of numerical experiments to compare the control performance of the idealized MPC strategy and the DMPC and DMPC-FOA approaches. The last section provides some concluding comments.

## **4.2 MPC approaches for longitudinal control of CAV platoon**

### ***4.2.1 An idealized MPC cooperative control strategy for a CAV platoon***

This section presents an idealized MPC strategy to control the CAVs in a platoon cooperatively by modifying the control strategies developed by Wang et al. (2014a) and Zhou et al. (2017). It seeks to coordinate the behavior of all following vehicles to: (1) maintain a desired safe spacing (labeled equilibrium spacing) between two consecutive vehicles in a platoon, and reduce traffic flow oscillations in terms of spacing and speed changes, and (2) maximize the comfort of travelers in these vehicles by minimizing deceleration and acceleration. The details of the idealized MPC strategy are as follows.

Consider a stream of CAVs in a single highway lane as shown in Fig. 4.1. Let  $0, 1, 2, \dots, n$  represent the CAVs in the platoon sequentially with 0 being the leading CAV and  $n$  being the tail CAV. The following assumptions will be used to design the longitudinal control of the CAV platoon:

All vehicles in the platoon are CAVs.

Two-way V2V communications exist between the leading vehicle and each of the following vehicles in the platoon (see Fig.1). Each following vehicle sends real-time information (speed

and position) to the leading vehicle. The leading vehicle sends the computed optimal control decisions to each of the following vehicles to control their driving behavior.

All CAVs can sense their kinematic states (speed, position, etc.) accurately and can send that information to the leading vehicle of their platoon instantaneously.

The leading CAV computes and sends the optimal control decisions (i.e., accelerations and decelerations) to all of the following CAVs which implement these decisions.

The actuator delay is negligible; that is, vehicles can implement the control instantly.

The pavement of the highway lane is in good condition and longitudinal slope is negligible.

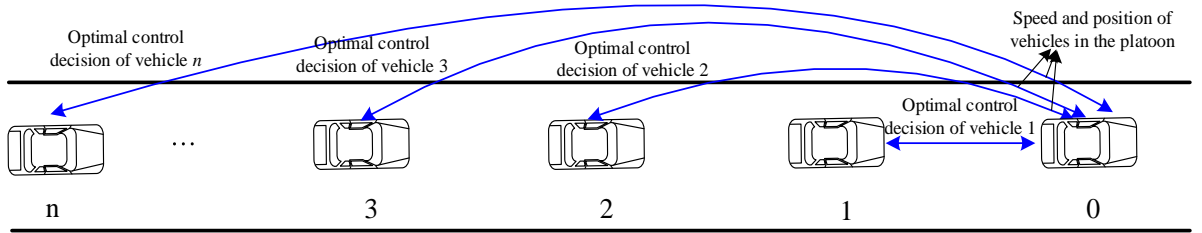


Figure 4.1. A CAV platoon stream.

In this study, we treat a platoon of CAVs as an integrated system, in which vehicles within the platoon are controlled in a coordinated manner. Define the state of a follower vehicle  $i$  as  $(s_i(t) - s_i^*(t), v_i(t) - v_{i-1}(t))$ , where  $s_i(t)$  is the spacing of vehicle  $i$  with its predecessor vehicle at time  $t$ ,  $v_i(t)$  is the speed of vehicle  $i$  at time  $t$ , and  $s_i^*(t)$  is the equilibrium spacing at time  $t$ .

This study uses the constant time headway policy to determine the equilibrium spacing. Thereby,  $s_i^*(t) = r_i^* \cdot v_i(t) + s_f$ , where  $r_i^*$  is the constant time headway for vehicle  $i$  and  $s_f$  is the safe distance to the predecessor vehicle.

For simplicity, the constant time headway for each follower vehicle in the platoon is assumed to be the same, i.e.,  $r_i^* = r^*, \forall i = 1, 2, \dots, n$ . Let  $x_i(t) = s_i(t) - s_i^*(t), \forall i$  be the position error between the desired spacing and actual spacing of vehicle  $i$  from its predecessor vehicle at time  $t$ . Denote  $y_i(t)$  as the speed difference of vehicle  $i$  from its predecessor vehicle at time  $t$ , i.e.,  $y_i(t) = v_i(t) - v_{i-1}(t)$ . Denote  $d_i(t)$  as the longitudinal position of CAV  $i$  in the platoon at time  $t$ . Then,

$$x_i(t) = d_{i-1}(t) - d_i(t) - r^* \cdot v_i(t) - s_f \quad (4.1)$$

and

$$\dot{x}_i(t) = v_{i-1}(t) - v_i(t) - r^* \cdot u_i(t) \quad (4.2a)$$

$$\dot{y}_i(t) = u_i(t) - u_{i-1}(t) \quad (4.2b)$$

where  $\dot{x}_i(t)$  is the first-order derivative of position error of vehicle  $i$  from its predecessor vehicle with respect to time  $t$ .  $\dot{y}_i(t)$  is the first-order derivative of speed difference of vehicle  $i$  from its predecessor vehicle with respect to time  $t$ .  $u_i(t)$  is the acceleration of CAV  $i$  at time



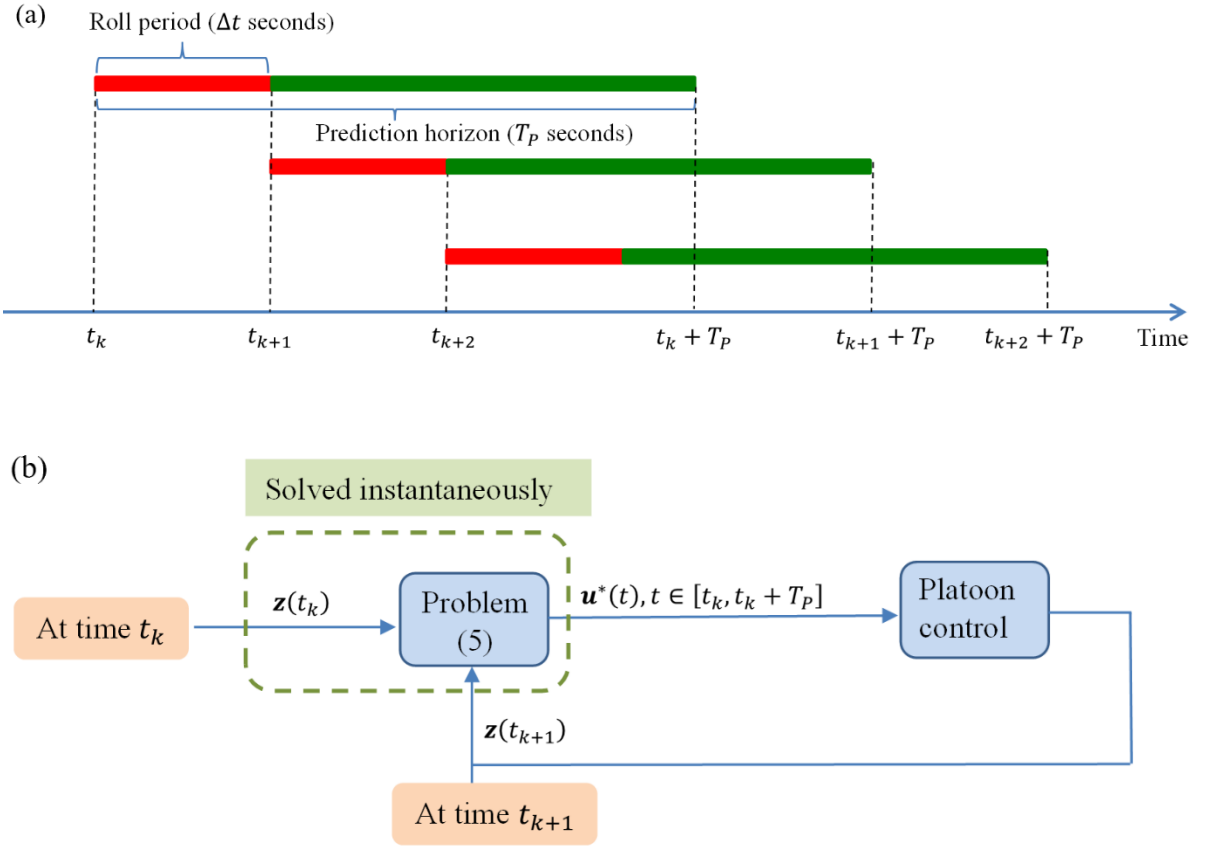


Figure 4.2. The idealized MPC strategy: (a) Implementation framework, and (b) Computational procedure.

Next, the idealized MPC strategy to determine the optimal control decisions and its computational procedure are exposted. Let  $\mathbf{z}(t) = [\mathbf{x}(t)^T, \mathbf{y}(t)^T]^T$ . Following Wang et al. (2014a) and Zhou et al. (2017), at each sampling time instant  $t_k, \forall k = 0, 1, 2, \dots$ , the optimal control decisions of all of the following vehicles in the platoon can be obtained by solving the following optimal control problem:

$$\min_{\mathbf{u}} \int_0^{T_P} \frac{1}{2} e^{-\beta t} L(\mathbf{z}(t), \mathbf{u}(t)) dt + \frac{1}{2} e^{-\beta T_P} \phi(\mathbf{z}(T_P)) \quad (4.5a)$$

$$\dot{\mathbf{z}}(t) = \mathbf{A} \cdot \mathbf{z}(t) + \mathbf{B} \cdot \mathbf{u}(t) \quad (4.5b)$$

$$s_i(t) = x_i(t) + r^* \cdot \left( v_0(0) + \sum_{j=1}^i y_j(t) \right) + s_f \geq s_{min}; i = 1, 2, \dots, n \quad (4.5c)$$

$$0 \leq v_i(t) \leq v_{max}; i = 1, 2, \dots, n \quad (4.5d)$$

$$u_{min} \leq u_i \leq u_{max}; i = 1, 2, \dots, n \quad (4.5e)$$

$$\mathbf{z}(0) = [\mathbf{x}_0^T \quad \mathbf{y}_0^T]^T \quad (4.5f)$$

where

$$L(\mathbf{z}(t), \mathbf{u}(t)) = \mathbf{z}(t)^T \begin{bmatrix} \mathbf{R}_1 & \\ & \mathbf{R}_2 \end{bmatrix} \mathbf{z}(t) + \mathbf{u}(t)^T \mathbf{R}_3 \mathbf{u}(t)$$

$$\phi(\mathbf{z}(T_p)) = \mathbf{z}(T_p)^T \begin{bmatrix} \mathbf{R}_4 & \\ & \mathbf{R}_5 \end{bmatrix} \mathbf{z}(T_p)$$

In problem (4.5), for expository convenience, we consider a generic prediction horizon and ignore the sampling time instant  $t_k$ . So,  $t \in [0, T_p]$  without loss of generality in (4.5). Here,  $\mathbf{R}_1$ ,  $\mathbf{R}_2$ ,  $\mathbf{R}_3$ ,  $\mathbf{R}_4$ , and  $\mathbf{R}_5$  are weight matrices;  $\mathbf{R}_1$ ,  $\mathbf{R}_2$ ,  $\mathbf{R}_4$ , and  $\mathbf{R}_5$  are symmetric positive definite matrices; and  $\mathbf{R}_3$  is a positive definite diagonal matrix (Zhou et al., 2017).  $L(\mathbf{z}(t), \mathbf{a}(t))$  is the running cost which is the cost incurred during an infinitesimal period (Wang et al. 2014a). It consists of two terms. The first term  $\mathbf{z}(t)^T \begin{bmatrix} \mathbf{R}_1 & \\ & \mathbf{R}_2 \end{bmatrix} \mathbf{z}(t)$  seeks to minimize the position errors and the relative speed of all adjacent vehicle pairs. The second component (i.e.,  $\mathbf{u}(t)^T \mathbf{R}_3 \mathbf{u}(t)$ ) is to maximize comfort by reducing hard braking and acceleration.  $e^{-\beta t}$  is a term to weight the running cost at different times and  $\beta$  is the discount coefficient. This term provides higher weight for the running cost for the near-term future than for the longer-term future as the uncertainty in running cost increases with time (Wang et al., 2014a).  $\phi(\mathbf{z}(T_p))$  is the terminal cost which is used to penalize the value of objective function if the values of the state variables at the end of the prediction horizon deviate from the equilibrium point (i.e., 0). Eq. (4.5b) describes the dynamics of the state variables (i.e., position errors and relative speeds of all adjacent vehicle pairs in the platoon). Eq. (4.5c) is a safety constraint to ensure that the spacing between two consecutive CAVs in the platoon is always larger than a positive lower bound  $s_{min}$ ,  $s_{min} > 0$ . Eq. (4.5d) specifies that the range of the speed of each vehicle in the platoon.  $v_{max}$  is the speed limit of the road. Eq. (4.5e) specifies the upper bound ( $u_{max}$ ) and lower bound ( $u_{min}$ ) of the acceleration. These inequality constraints are extensively used in literature for designing effective control method for CAV platoon (see e.g., Wang et al., 2018b; Lu et al., 2019). Eq. (4.5f) specifies the initial inputs for the state variables. Hence, for example, for any sampling time instant  $t_k$ ,  $\mathbf{x}_k = [x_1(t_k), x_2(t_k), \dots, x_n(t_k)]$  and  $\mathbf{y}_k = [y_1(t_k), y_2(t_k), \dots, y_n(t_k)]$  are values of  $\mathbf{x}_0^T$  and  $\mathbf{y}_0^T$ , respectively.

There are primarily two differences between optimal control problem (4.5) and the ones developed by Wang et al. (2014a) and Zhou et al. (2017). First, a term  $e^{-\beta t}$  is added to the objective function to weight the running costs at different times. Second, a terminal cost  $\phi(\mathbf{z}(T_p))$  is added to penalize the objective function if the state variables deviate from the equilibrium point 0 at the end of the prediction horizon. These two terms will be useful to analyze the stability of the idealized MPC strategy. In addition, for convenience of stability analysis, the weight matrices  $\mathbf{R}_i (i = 1, 2, 4, 5)$  are assumed to have the following forms:

$$\mathbf{R}_1 = \Lambda^T \mathbf{D}_a \Lambda, \mathbf{R}_2 = \Lambda^T \mathbf{D}_b \Lambda, \mathbf{R}_4 = \Lambda^T \mathbf{D}_c \Lambda, \text{ and } \mathbf{R}_5 = \Lambda^T \mathbf{D}_e \Lambda \quad (4.6)$$

where  $\Lambda$  is an orthogonal matrix,  $\Lambda^T \Lambda = \Lambda \Lambda^T = \mathbf{E}_n$ , and  $\mathbf{D}_a$ ,  $\mathbf{D}_b$ ,  $\mathbf{D}_c$  and  $\mathbf{D}_e$  are positive definite diagonal matrices. The inputs of these weight matrices will be determined by the

stability analysis in Section 4.5. Eq. (4.6) shows that if  $\Lambda = E_n$ , then  $R_1, R_2, R_4$ , and  $R_5$  are positive definite diagonal matrices.

Let  $\mathbf{z}(t_k)$  be the actual values of the state variables at the sampling time instant  $t_k, (k = 1, 2, \dots)$ ,  $\mathbf{z}(t_k) = [\mathbf{x}_k^T \ \mathbf{y}_k^T]^T$ . The computational procedure of the idealized MPC strategy is summarized in Fig. 4.2(b). At each sampling time instant  $t_k (k = 1, 2, \dots)$ , the leading vehicle obtains the value of  $\mathbf{z}(t_k)$  through V2V communications. It solves the optimal control problem (4.5) to determine the optimal control decisions (i.e.,  $\mathbf{u}^*(t)$ ) during the prediction horizon  $[t_k, t_k + T_p]$  by inputting the value of  $\mathbf{z}(t_k)$  into Eq. (4.5e). The optimal control decisions are sent by the leading vehicle to the following vehicles to control their behaviors only for the roll period  $[t_k, t_k + \Delta t]$ , (i.e.,  $[t_k, t_{k+1}]$ ). Then, at the sampling time instant  $t_{k+1}$ , the optimal control problem (4.5) is solved again to obtain the optimal control decisions  $\mathbf{u}^*(t)$  for the prediction horizon  $[t_{k+1}, t_{k+1} + T_p]$ , and is implemented to control the CAV platoon for the roll period  $[t_{k+1}, t_{k+1} + \Delta t]$ . These steps are repeated at each sampling time instant.

As can be noted, the idealized MPC strategy computes the optimal control decisions by solving optimal control problem (4.5) at each sampling time instant and implements it to control the CAVs for the roll period starting at that instant. To achieve this, it is assumed that the leading vehicle can solve the optimal control problem (4.5) of the idealized MPC strategy instantaneously at each sampling time instant  $t_k$ . However, in practice, the computational time for solving optimal control problem (4.5) increases with platoon size and prediction horizon size. It can cause significant delays in executing the control decisions, which can deteriorate the performance and even lead to vehicle collisions. Thereby, while the idealized MPC strategy can coordinate the behavior of the following vehicles in the platoon to maneuver them efficiently and safely, it cannot be deployed to control the CAV platoon in real-time.

#### **4.2.2 DMPC approach framework**

The leading vehicle of a CAV platoon needs to respond to the dynamics of the vehicles downstream of it. Thereby, its behavior is not known in advance. However, the behavior of all following vehicles in the platoon for each roll period can be estimated at the corresponding sampling time instant through the known optimal control decisions of the previous roll period (i.e.,  $\mathbf{u}^*(t), t \in [t_{k-1}, t_{k-1} + \Delta t]$ ). To account for this difference, we divide  $\mathbf{z}(t)$  into two parts,  $\mathbf{z}_1(t)$  and  $\mathbf{z}_2(t)$ . We denote the vector of position error and speed difference of vehicle 1 from that of the leading vehicle 0 as  $\mathbf{z}_1(t) = [x_1(t), y_1(t)]^T$ , and the vector of state variables for the other following vehicles as  $\mathbf{z}_2(t) = [x_2(t), x_3(t), \dots, x_n(t), y_2(t), y_3(t), \dots, y_n(t)]^T$ . At each sampling time instant  $t_k$ , the value of  $\mathbf{z}_1(t_k)$  cannot be computed in advance due to the unknown position and speed of the leading vehicle at that instant. However,  $\mathbf{z}_2(t_k)$  can be estimated in advance at a short time before the sampling time instant  $t_k$ .

We propose the DMPC approach to address the strong assumption of the idealized MPC strategy that the optimal control problem (4.5) can be solved instantaneously. The implementation framework for the DMPC approach is shown in Fig. 4.3(a). Unlike the idealized MPC strategy, the DMPC approach reserves a sufficient amount of time, labeled reserved time (denoted as  $\tau_1$ ), before each sampling time instant  $t_k (k = 1, 2, \dots)$  to solve the optimal control problem (4.5) so that the optimal control decisions are available at  $t_k$  for the corresponding roll period. It is important to note that the roll period  $\Delta t$  should be larger than

$\tau_1$  to enable the real-time implementation of the DMPC approach.

The DMPC computational procedure is illustrated in Fig. 4.3(b). The DMPC approach starts to solve the optimal control problem at time  $t_k - \tau_1$  to predict the values of all state variables at time  $t_k$  (i.e.,  $\mathbf{z}(t_k)$ ). As stated in the assumptions, the leading vehicle can obtain the actual states of all following vehicles at time instant  $t_k - \tau_1$  through V2V communications. Also, as discussed earlier in this section, it knows the control decisions of all following vehicles in the time period  $[t_k - \tau_1, t_k]$  as they are determined at the beginning of the previous roll period. The DMPC approach leverages these two sets of inputs to predict  $\mathbf{z}_2(t_k)$  with low error. This is because in the context of the CAV platooning application,  $\tau_1$  is much smaller than the roll period, in the order of a fraction of a second. Hence, as the actual states are available close to  $t_k$ , and prior control decisions are known, we assume that the error in estimating  $\mathbf{z}_2(t_k)$  is negligible.

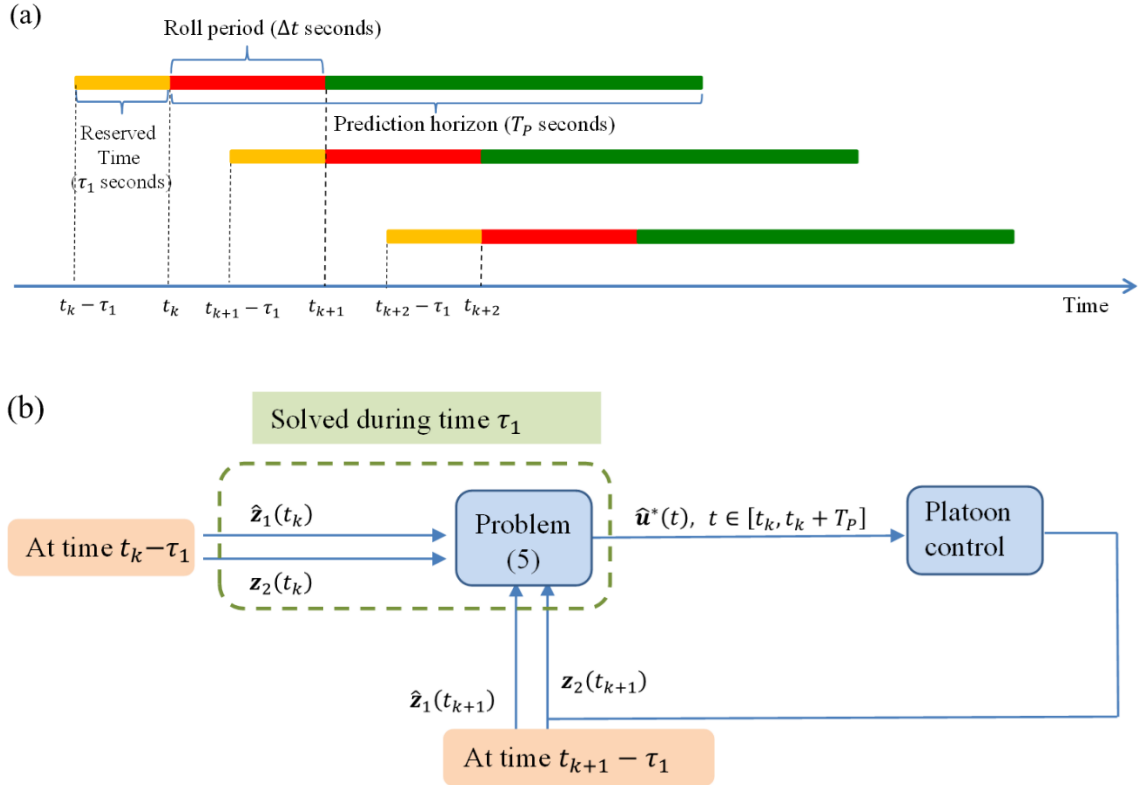


Figure 4.3. The DMPC approach: (a) Implementation framework, and (b) Computational procedure.

As discussed earlier, the leading vehicle's behavior is not known in advance. Thereby,  $\mathbf{z}_1(t_k)$  cannot be estimated with low error unlike  $\mathbf{z}_2(t_k)$ . Hence, the value of  $\mathbf{z}_1(t_k)$  needs to be predicted at time instant  $t_k - \tau_1$ . To do so, the leading vehicle's behavior at  $t_k$  needs to be predicted at  $t_k - \tau_1$ . As  $\tau_1$  is much smaller than the roll period, we assume the acceleration of the leading vehicle 0 during the small time interval  $[t_k - \tau_1, t_k]$  remains the same as at time instant  $t_k - \tau_1$ . Then,

$$\hat{v}_0(t_k) = v_0(t_k - \tau_1) + u_0(t_k - \tau_1) \cdot \tau_1 \quad (4.7a)$$

$$\hat{d}_0(t_k) = d_0(t_k - \tau_1) + v_0(t_k - \tau_1) \cdot \tau_1 + 0.5 \cdot u_0(t_k - \tau_1) \cdot (\tau_1)^2 \quad (4.7b)$$

where  $\hat{v}_0(t_k)$  and  $\hat{d}_0(t_k)$  are the predicted speed and predicted position of the leading vehicle at time instant  $t_k$ , respectively. Here,  $v_0(t_k - \tau_1)$ ,  $d_0(t_k - \tau_1)$  and  $u_0(t_k - \tau_1)$  are the actual speed, position and acceleration of the leading vehicle at  $t_k - \tau_1$ , respectively, that are detected through onboard sensors. The position error and relative speed of vehicle 1 from that of the leading vehicle 0 at time instant  $t_k$  can then be predicted as:

$$\hat{x}_1(t_k) = \hat{d}_0(t_k) - d_1(t_k) - r^* \cdot v_1(t_k) - s_f \quad (4.8a)$$

$$\hat{y}_1(t_k) = v_1(t_k) - \hat{v}_0(t_k) \quad (4.8b)$$

where  $\hat{x}_1(t_k)$  and  $\hat{y}_1(t_k)$  are the predicted position error and speed difference of vehicle 1 with respect to the leading vehicle 0 at time  $t_k$ , respectively. Note that the speed and position of vehicle 1 at time instant  $t_k - \tau_1$  are detected through the onboard sensors, and the corresponding control decision  $u_1(t)$ ,  $t \in [t_k - \tau_1, t_k]$  is known. Then,  $d_1(t_k)$  and  $v_1(t_k)$  can be computed as:

$$v_1(t_k) = v_1(t_k - \tau_1) + \int_{t_k - \tau_1}^{t_k} u_1(t) dt \quad (4.9a)$$

$$\begin{aligned} d_1(t_k) &= d_1(t_k - \tau_1) + \int_{t_k - \tau_1}^{t_k} v_1(t) dt \\ &= d_1(t_k - \tau_1) + \int_{t_k - \tau_1}^{t_k} \left[ v_1(t_k - \tau_1) + \left( \int_{t_k - \tau_1}^t u_1(\zeta) d\zeta \right) \right] dt \end{aligned} \quad (4.9b)$$

Note that the predicted value  $\hat{\mathbf{z}}_1(t_k)$  ( $\hat{\mathbf{z}}_1(t_k) = [\hat{x}_1(t_k), \hat{y}_1(t_k)]$ ) is different from the actual value  $\mathbf{z}_1(t_k)$  due to the error in predicting the leading vehicle's position and speed. Thereby, the estimated control decisions of the DMPC approach (i.e.,  $\hat{\mathbf{u}}(t)$ ) are different from the optimal control decisions computed by the idealized MPC strategy (i.e.,  $\mathbf{u}^*(t)$ ). In the numerical experiments, we will show that the estimated control decisions of the DMPC approach will deviate significantly from those of the idealized MPC strategy when the error in predicting  $\mathbf{z}_1(t_k)$  is large. This will deteriorate the efficiency of the CAV platoon and can cause vehicular collisions.

It should be noted that other models can also be used to predict the leading vehicle's state. However, prediction error exists for all models as the leading vehicle's behavior is unknown, which may impact the control performance of the DMPC approach.

### **4.2.3 DMPC-FOA approach framework**

The DMPC approach circumvents the strong assumption of the idealized MPC strategy at the cost that the estimated control decisions may deviate significantly from those of the idealized MPC strategy due to the error in predicting  $\mathbf{z}_1(t_k)$ . To address this problem, we propose the DMPC-FOA approach which simultaneously addresses the control delay issue of the idealized MPC strategy while more accurately characterizing the optimal control decisions.

Let  $\tau_2$  be the reserved time for computing the optimal control decisions for the DMPC-FOA approach. Also, let  $\tilde{\mathbf{z}}_1(t_k) = [\tilde{x}_1(t_k) \quad \tilde{y}_1(t_k)]$  be the predicted value of  $\mathbf{z}_1(t_k)$  for the

DMPC-FOA approach at time instant  $t_k - \tau_2$  by replacing  $\tau_1$  with  $\tau_2$  in Eqs. (7) and (8). Here,  $\tilde{x}_1(t_k)$  and  $\tilde{y}_1(t_k)$  are the predicted position error and speed difference of vehicle 1 with respect to the leading vehicle at time instant  $t_k$ , respectively. Similar to the DMPC approach, we assume the error in estimating  $\mathbf{z}_2(t_k)$  is negligible as the actual states (i.e.,  $\mathbf{z}_2(t_k - \tau_2)$ ) are available close to  $t_k$ , and prior control decisions are known.

Denote  $\boldsymbol{\gamma}(t)$  as the vector of costate variables associated with the state equations (5b). The costate variables indicate the change in the objective function value for a unit change in the corresponding state variable at the optimal state (Gaimon, 2002). The computational procedure for the DMPC-FOA approach is illustrated in Fig. 4.4, where  $\tilde{\mathbf{z}}^*(t)$  and  $\tilde{\boldsymbol{\gamma}}^*(t)$ ,  $t \in [t_k, t_k + T_p]$  are the solutions for the state and costate variables obtained by solving optimal control problem (4.5) with initial inputs  $[\tilde{\mathbf{z}}_1(t_k), \mathbf{z}_2(t_k)]$ . The optimal control decisions for the idealized MPC strategy,  $\boldsymbol{\varphi}(\mathbf{z}^*(t), \boldsymbol{\gamma}^*(t))$  (denoted as  $\mathbf{u}^*(t)$ ), are analytically derived in Section 4.3 (see Eq. (4.23)) which discusses the solution algorithm. Then,  $\mathbf{u}^*(t)$ ,  $t \in [t_k, t_k + T_p]$  can be approximated by  $\boldsymbol{\varphi}(\tilde{\mathbf{z}}^*(t), \tilde{\boldsymbol{\gamma}}^*(t))$  (denoted as  $\tilde{\mathbf{u}}^*(t)$ ). Note that the difference between  $[\tilde{\mathbf{z}}^*(t), \tilde{\boldsymbol{\gamma}}^*(t)]$  and  $[\mathbf{z}^*(t), \boldsymbol{\gamma}^*(t)]$  significantly impacts the accuracy of the estimated control decisions  $\tilde{\mathbf{u}}^*(t)$ . To reduce the difference between  $\tilde{\mathbf{u}}^*(t)$  and  $\mathbf{u}^*(t)$ ,  $t \in [t_k, t_k + T_p]$ , sensitivity analysis of the optimal control problem (4.5) is performed to determine the derivatives of  $\partial \tilde{\mathbf{z}}^*(t) / \partial \tilde{\mathbf{z}}_1(t_k)$  (i.e.,  $\left[ \frac{\partial \tilde{\mathbf{z}}^*(t)}{\partial \tilde{x}_1(t_k)}, \frac{\partial \tilde{\mathbf{z}}^*(t)}{\partial \tilde{y}_1(t_k)} \right]$ ) and  $\partial \tilde{\boldsymbol{\gamma}}^*(t) / \partial \tilde{\mathbf{z}}_1(t_k)$  (i.e.,  $\left[ \frac{\partial \tilde{\boldsymbol{\gamma}}^*(t)}{\partial \tilde{x}_1(t_k)}, \frac{\partial \tilde{\boldsymbol{\gamma}}^*(t)}{\partial \tilde{y}_1(t_k)} \right]$ ). These two terms can quantitatively measure the changes in the optimal solutions for  $\tilde{\mathbf{z}}^*(t)$  and  $\tilde{\boldsymbol{\gamma}}^*(t)$  for a unit increase in  $\tilde{\mathbf{z}}_1(t_k)$ . Thereby, at sampling time instant  $t_k$  when the actual value of  $x_1(t_k)$  and  $y_1(t_k)$  are detected through onboard sensors, the first-order Taylor's approximation is applied to better estimate the solutions of  $\mathbf{z}^*(t)$  and  $\boldsymbol{\gamma}^*(t)$ , as follows:

$$\begin{aligned} \bar{\mathbf{z}}^*(t) = \tilde{\mathbf{z}}^*(t) &+ \frac{\partial \tilde{\mathbf{z}}^*(t)}{\partial \tilde{x}_1(t_k)} (x_1(t_k) - \tilde{x}_1(t_k)) \\ &+ \frac{\partial \tilde{\mathbf{z}}^*(t)}{\partial \tilde{y}_1(t_k)} (y_1(t_k) - \tilde{y}_1(t_k)), t \in [t_k, t_k + T_p] \end{aligned} \quad (4.10a)$$

$$\begin{aligned} \bar{\boldsymbol{\gamma}}^*(t) = \tilde{\boldsymbol{\gamma}}^*(t) &+ \frac{\partial \tilde{\boldsymbol{\gamma}}^*(t)}{\partial \tilde{x}_1(t_k)} (x_1(t_k) - \tilde{x}_1(t_k)) \\ &+ \frac{\partial \tilde{\boldsymbol{\gamma}}^*(t)}{\partial \tilde{y}_1(t_k)} (y_1(t_k) - \tilde{y}_1(t_k)), t \in [t_k, t_k + T_p] \end{aligned} \quad (4.10b)$$

where  $\bar{\mathbf{z}}^*(t)$  and  $\bar{\boldsymbol{\gamma}}^*(t)$  are the values of  $\mathbf{z}^*(t)$  and  $\boldsymbol{\gamma}^*(t)$  estimated by the DMPC-FOA approach, respectively.

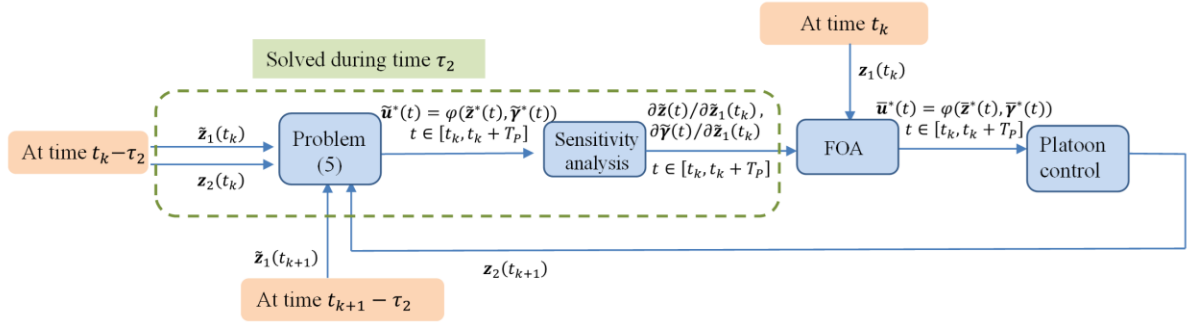


Figure 4.4. Computational procedure of the DMPC-FOA approach.

When compared to  $[\tilde{z}^*(t), \tilde{\gamma}^*(t)]$ ,  $[\bar{z}^*(t), \bar{\gamma}^*(t)]$  are closer to  $[z^*(t), \gamma^*(t)]$ . Thereby, in Fig. 4.4, the estimated control decisions  $\bar{u}^*(t) = \varphi(\bar{z}^*(t), \bar{\gamma}^*(t))$  are closer to  $u^*(t)$  compared to  $\tilde{u}^*(t), t \in [t_k, t_k + T_p]$ . It is important to note here that Eq. (4.10) can be calculated instantaneously if the derivatives are obtained before the sampling time instant  $t_k$ . In addition,  $\varphi(\bar{z}^*(t), \bar{\gamma}^*(t))$  can also be calculated instantaneously due to the closed-form formulation (Eq. (4.23)). Thereby, the DMPC-FOA approach can be applied for real-time control of the CAV platoon with no control delay.

As can be noted, before each sampling time instant  $t_k$ , the DMPC-FOA approach needs to solve the optimal control problem (4.5) and conduct sensitivity analysis. Hence, the reserved time  $\tau_2 \geq \tau_1$ . Nevertheless, we will show using numerical examples that the gap between  $\bar{u}^*(t)$  and  $u^*(t)$  is negligible even for large prediction errors of  $z_1(t_k)$  at every sampling time instant  $t_k$ .

### 4.3 Solution algorithm for optimal control problem (4.5)

To solve optimal control problem (4.5), a two-point boundary value problem is developed in this section based on the necessary conditions for optimality, the solution of which determines the optimal control decisions for all following CAVs. The two-point boundary value problem can be solved efficiently using methods such as the shooting method (Keller, 1976), method of steepest descent (Kirk, 2012), and iterative algorithm (Wang et al., 2014b).

Optimal control problem (4.5) contains control constraints (Eq. (4.5d)) and pure state variable inequality constraints (5c). The presence of pure state variable inequality constraints increases the difficulty in designing an effective solution algorithm as these constraints depend on the control history. To address this problem, optimal control problem (4.5) is converted to an equivalent optimal control problem without pure state variable inequality constraints. To do so, we define a

new variable  $z_N$  that has the following functional relationship

$$\dot{z}_N(t) = \sum_{i=1}^n (z_{N,1}^i + z_{N,2}^i + z_{N,3}^i) \quad (4.11)$$

$$\text{Where } z_{N,1}^i = [s_i(t) - s_{min}]^2 I(s_i(t) - s_{min})$$

$$z_{N,2}^i = [v_{max} - v_i(t)]^2 I(v_{max} - v_i(t))$$

$$z_{N,3}^i = v_i(t) I(v_i(t))$$

$$I(s_i(t) - s_{min}) = \begin{cases} 0, & \text{if } s_i(t) - s_{min} \geq 0 \\ 1, & \text{otherwise} \end{cases}$$

$$I(v_{max} - v_i(t)) = \begin{cases} 0, & \text{if } v_{max} - v_i(t) \geq 0 \\ 1, & \text{otherwise} \end{cases}$$

$$I(v_i(t)) = \begin{cases} 0, & \text{if } v_i(t) \geq 0 \\ 1, & \text{otherwise} \end{cases}$$

Proposition 1: If  $z_N(0) = z_N(T_P) = 0$ , then  $s_i(t) \geq s_{min}$  and  $0 \leq v_i(t) \leq v_{max}$ ;  $i = 1, 2, \dots, n$  for  $t \in [0, T_P]$ .

Proof: According to Eq. (4.11),  $z_N(t)$  is a continuous function of time  $t$  and  $\dot{z}_N(t) \geq 0$ . Thereby,  $z_N(t)$  is a non-decreasing function of time  $t$ . Since  $z_N(0) = z_N(T_P) = 0$ , this implies that  $\dot{z}_N(t) \equiv 0$  for  $t \in [0, T_P]$  (otherwise,  $z_N(T_P) = \int_0^{T_P} \dot{z}_N(t) dt + z_N(0) = \int_0^{T_P} \dot{z}_N(t) dt > 0$ ). According to Eq. (4.11),  $\dot{z}_N(t) \equiv 0$  if and only if  $s_i(t) \geq s_{min}$  and  $v_i(t) \leq v_{max}$ ;  $i = 1, 2, \dots, n$  for  $t \in [0, T_P]$ . This completes the proof.

According to Proposition 1, the optimal control problem (4.5) can be rewritten as the following equivalent problem:

$$\min_{\mathbf{u}} \int_0^{T_P} \frac{1}{2} e^{-\beta t} [\mathbf{z}(t)^T \mathbf{Q}_1 \mathbf{z}(t) + \mathbf{u}(t)^T \mathbf{R}_3 \mathbf{u}(t)] dt + \frac{1}{2} e^{-\beta T_P} \mathbf{z}(T_P)^T \mathbf{Q}_2 \mathbf{z}(T_P) \quad (4.12a)$$

$$\dot{\mathbf{z}}(t) = \mathbf{A} \cdot \mathbf{z}(t) + \mathbf{B} \cdot \mathbf{u}(t) \quad (4.12b)$$

$$\dot{z}_N(t) = \sum_{i=1}^n (z_{N,1}^i + z_{N,2}^i + z_{N,3}^i) \quad (4.12c)$$

$$u_{min} \leq u_i \leq u_{max}; i = 1, 2, \dots, n \quad (4.12d)$$

$$\mathbf{z}(0) = [\mathbf{x}_0^T \quad \mathbf{y}_0^T]^T; z_N(0) = z_N(T_P) = 0 \quad (4.12e)$$

$$\text{where } \mathbf{Q}_1 = \begin{bmatrix} \mathbf{R}_1 & \\ & \mathbf{R}_2 \end{bmatrix}; \mathbf{Q}_2 = \begin{bmatrix} \mathbf{R}_4 & \\ & \mathbf{R}_5 \end{bmatrix}$$

To develop a two-point boundary value problem based on the necessary conditions for optimality

of optimal control problem (4.5), the terminal condition  $z_N(T_p) = 0$  is removed from Eq. (4.12e). To ensure  $z_N(T_p) \rightarrow 0$ , similar to the study of Naidu (2003), the term  $M \cdot (z_N(T_p))^2$  is added to the objective function, where  $M$  is a sufficiently large number. If  $z_N(T_p) \neq 0$ , the objective function is penalized. The optimal control problem (4.12) can then be re-written as:

$$\min_{\mathbf{u}} \int_0^{T_p} \frac{1}{2} e^{-\beta t} [\mathbf{z}(t)^T \mathbf{Q}_1 \mathbf{z}(t) + \mathbf{u}(t)^T \mathbf{R}_3 \mathbf{u}(t)] dt + \frac{1}{2} e^{-\beta T_p} \mathbf{z}(T_p)^T \mathbf{Q}_2 \mathbf{z}(T_p) + M \cdot (z(T_p))^2 \quad (4.13a)$$

$$\dot{\mathbf{z}}(t) = \mathbf{A} \cdot \mathbf{z}(t) + \mathbf{B} \cdot \mathbf{u}(t) \quad (4.13b)$$

$$\dot{z}_N(t) = \sum_{i=1}^n (z_{N,1}^i + z_{N,2}^i + z_{N,3}^i) \quad (4.13c)$$

$$u_{min} \leq u_i \leq u_{max}; i = 1, 2, \dots, n \quad (4.13d)$$

$$\mathbf{z}(0) = [\mathbf{x}_0^T \quad \mathbf{y}_0^T]^T; z_N(0) = 0 \quad (4.13e)$$

Optimal control problem (4.13) is equivalent to problem (4.5). It contains only control constraints. Define the vector of functions  $\mathbf{f}_1(\mathbf{z}(t), \mathbf{u}(t))$  and the function  $f_2(\mathbf{z}(t), \mathbf{u}(t))$  as follows:

$$\dot{\mathbf{z}}(t) = \begin{bmatrix} \dot{\mathbf{x}}(t) \\ \dot{\mathbf{y}}(t) \end{bmatrix} = \mathbf{f}_1(\mathbf{z}(t), \mathbf{u}(t)) = \mathbf{A} \cdot \mathbf{z}(t) + \mathbf{B} \cdot \mathbf{u}(t) \quad (4.14a)$$

$$\dot{z}_N(t) = f_2(\mathbf{z}(t), \mathbf{u}(t)) = \sum_{i=1}^n (z_{N,1}^i + z_{N,2}^i + z_{N,3}^i) \quad (4.14b)$$

Then, the Hamiltonian function for optimal control problem (4.13) is written as:

$$\begin{aligned} \mathbf{H}(\mathbf{z}(t), \boldsymbol{\lambda}_A(t), \mathbf{u}(t)) \\ = e^{-\beta t} L(\mathbf{z}(t), \mathbf{u}(t)) + \boldsymbol{\lambda}(t)^T \cdot \mathbf{f}_1(\mathbf{z}(t), \mathbf{u}(t)) + \lambda_N(t) \\ \cdot f_2(\mathbf{z}(t), \mathbf{u}(t)). \end{aligned} \quad (4.15)$$

where  $\boldsymbol{\lambda}(t) = [\lambda_1(t) \quad \dots \quad \lambda_{2n}(t)]^T$  and  $\lambda_N(t)$  are the costate variables associated with  $\mathbf{f}_1(\mathbf{z}(t), \mathbf{u}(t))$  and  $f_2(\mathbf{z}(t), \mathbf{u}(t))$ , respectively. Let  $\boldsymbol{\lambda}_A(t) = [\boldsymbol{\lambda}(t)^T, \lambda_N(t)]^T$ , and  $\mathbf{z}_A(t) = [\mathbf{z}(t)^T, z_N(t)]^T$ . According to Pontryagin's minimum principle, the necessary conditions for  $\mathbf{u}^*(t)$

to be an optimal solution for problem (4.13) are

$$\dot{\lambda}_A(t) = - \left( \frac{\partial \mathbf{H}}{\partial \mathbf{z}_A(t)} \right) \quad (4.16a)$$

$$\begin{bmatrix} \dot{\mathbf{z}}(t) \\ \dot{z}_N(t) \end{bmatrix} = \begin{bmatrix} \mathbf{f}_1(\mathbf{z}(t), \mathbf{u}(t)) \\ f_2(\mathbf{z}(t), \mathbf{u}(t)) \end{bmatrix} \quad (4.16b)$$

with the initial conditions given in Eq. (4.13e) and the terminal conditions as:

$$\lambda(T_P) = \partial \left( \frac{1}{2} e^{-\beta T_P} \mathbf{z}(t)^T \mathbf{Q}_2 \mathbf{z}(t) \right) / \partial \mathbf{z}(t) \Big|_{t=T_P} \quad (4.16c)$$

$$= e^{-\beta T_P} \cdot \mathbf{Q}_2 \cdot \mathbf{z}(T_P);$$

$$\lambda_N(T_P) = \partial (M \cdot z_N(t)^2) / \partial z_N(t) \Big|_{t=T_P} \quad (4.16d)$$

$$= 2 M \cdot z_N(T_P).$$

In addition, the optimal state trajectory  $\mathbf{z}^*(t)$ , the optimal costate trajectory  $\lambda_A^*(t)$  and the optimal control decisions  $\mathbf{u}^*(t)$  should satisfy

$$\mathbf{H}(\mathbf{z}^*(t), \lambda_A^*(t), \mathbf{u}^*(t)) \leq \mathbf{H}(\mathbf{z}^*(t), \lambda_A^*(t), \mathbf{u}(t)); \quad \mathbf{u}(t), \mathbf{u}^*(t) \in \mathbf{U} \quad (4.16e)$$

where  $\mathbf{U} = \{\mathbf{u} | u_{min} \leq u_i \leq u_{max}; i = 1, 2, \dots, n\}$ . To convert these necessary conditions for optimality into a two-point boundary value problem, we define the current-value Hamiltonian function as follows:

$$\mathbf{H}_c = e^{\beta t} \mathbf{H} = L(\mathbf{z}(t), \mathbf{u}(t)) + \boldsymbol{\gamma}(t)^T \mathbf{f}_1(\mathbf{z}(t), \mathbf{u}(t)) + \gamma_N(t) f_2(\mathbf{z}(t), \mathbf{u}(t)). \quad (4.17)$$

where  $\boldsymbol{\gamma}(t) = \boldsymbol{\lambda}(t) e^{\beta t}$ ,  $\gamma_N = \lambda_N(t) e^{\beta t}$  are the costate variables for the current-value Hamiltonian function. Since the discount factor  $e^{-\beta t}$  does not depend on the control variables, the optimal control  $\mathbf{u}^*$  that minimizes the Hamiltonian function  $\mathbf{H}$  must also minimize the current-value

Hamiltonian function (Eq. (4.17)). Let  $\boldsymbol{\gamma}_A = [\boldsymbol{\gamma}(t)^T, \gamma_N(t)^T]^T$ . Then,

$$\dot{\boldsymbol{\lambda}}_A(t) = -\beta e^{-\beta t} \boldsymbol{\gamma}_A(t) + e^{-\beta t} \dot{\boldsymbol{\gamma}}_A(t). \quad (4.18a)$$

$$\frac{\partial \mathbf{H}}{\partial \mathbf{z}_A(t)} = \frac{\partial \mathbf{H}_c}{\partial \mathbf{z}_A(t)} e^{-\beta \cdot t} \quad (4.18b)$$

Eqs. 18(a) and 18(b) imply

$$\dot{\boldsymbol{\gamma}}_A(t) = \dot{\boldsymbol{\lambda}}_A(t) + \beta \boldsymbol{\gamma}_A(t) \quad (4.19)$$

Thereby,

$$\begin{aligned} \dot{\boldsymbol{\gamma}}(t) &= -\frac{\partial \mathbf{H}_c}{\partial \mathbf{z}} + \beta \boldsymbol{\gamma}(t) \\ &= -\frac{\partial \mathbf{f}_1(\mathbf{z}, \mathbf{u})}{\partial \mathbf{z}} \boldsymbol{\gamma}(t) - \frac{\partial \mathbf{f}_2(\mathbf{z}, \mathbf{u})}{\partial \mathbf{z}} \gamma_N(t) - \frac{\partial L(\mathbf{z}, \mathbf{u})}{\partial \mathbf{z}} + \beta \boldsymbol{\gamma}(t) \end{aligned} \quad (4.20a)$$

$$= -\mathbf{A} \cdot \boldsymbol{\gamma}(t) - \begin{bmatrix} \mathbf{C}_x \\ \mathbf{C}_y \end{bmatrix} \gamma_N(t) - \mathbf{Q}_1 \mathbf{z}(t) + \beta \boldsymbol{\gamma}(t).$$

$$\dot{\gamma}_N(t) - \beta \cdot \gamma_N(t) = -\partial \mathbf{H}_c / \partial z_N(t) = 0 \quad (4.20b)$$

where

$$\mathbf{C}_x = \frac{\partial \mathbf{f}_2(\mathbf{z}(t), \mathbf{u}(t))}{\partial \mathbf{x}(t)} = \begin{bmatrix} 2 \cdot [s_1(t) - s_{min}] \cdot I(s_1(t) - s_{min}) \\ 2 \cdot [s_2(t) - s_{min}] \cdot I(s_2(t) - s_{min}) \\ \vdots \\ 2 \cdot [s_n(t) - s_{min}] \cdot I(s_n(t) - s_{min}) \end{bmatrix}$$

$$\begin{aligned} \mathbf{C}_y &= \frac{\partial \mathbf{f}_2(\mathbf{z}(t), \mathbf{u}(t))}{\partial \mathbf{y}(t)} \\ &= \begin{bmatrix} 2 \cdot [v_{max} - v_1(t)] \cdot I(v_{max} - v_1(t)) \\ 2 \cdot [v_{max} - v_2(t)] \cdot I(v_{max} - v_2(t)) \\ \vdots \\ 2 \cdot [v_{max} - v_n(t)] \cdot I(v_{max} - v_n(t)) \end{bmatrix} + \begin{bmatrix} 2 \cdot v_1(t) \cdot I(v_1(t)) \\ 2 \cdot v_2(t) \cdot I(v_2(t)) \\ \vdots \\ 2 \cdot v_3(t) \cdot I(v_3(t)) \end{bmatrix} \\ &\quad + \begin{bmatrix} \mathbf{C}_{1,y} \\ \mathbf{C}_{2,y} \\ \vdots \\ \mathbf{C}_{n,y} \end{bmatrix} \end{aligned}$$

$$\mathbf{C}_{i,y} = \sum_{j=1}^i 2 \cdot [s_j(t) - s_{min}] \cdot I(s_j(t) - s_{min}), \forall i = 1, 2, \dots, n.$$

The terminal conditions in Eq. (4.16c) and Eq. (4.16d) imply that

$$\boldsymbol{\gamma}(T_P) = \mathbf{Q}_2 \cdot \mathbf{z}(T_P)^T, \gamma_N(T_P) = e^{\beta T_P} \cdot \mathbf{M} \cdot \mathbf{2} \cdot \mathbf{z}_N(T_P) \quad (4.21)$$

Let  $\boldsymbol{\gamma}_A^*(t) = \boldsymbol{\lambda}_A^*(t)e^{\beta t}$ . Since  $e^{\beta t} > 0$ , according to Eq. (4.17), at time  $t$ , minimizing  $\mathbf{H}(\mathbf{z}^*(t), \boldsymbol{\lambda}_A^*(t), \mathbf{u}(t))$  with respect to  $\mathbf{u}(t)$  is equivalent to minimizing  $\mathbf{H}_c(\mathbf{z}^*(t), \boldsymbol{\gamma}_A^*(t), \mathbf{u}(t))$  with respect to  $\mathbf{u}(t)$ . This indicates that if the optimal control  $\mathbf{u}^*$  minimizes  $\mathbf{H}_c(\mathbf{z}^*(t), \boldsymbol{\lambda}_A^*(t), \mathbf{u}(t))$ , it is the solution to inequality (4.16e). Thereby,  $\mathbf{u}^*(t)$  can be found by solving the following minimization problem

$$\min_{\mathbf{u}(t)} \mathbf{H}_c(\mathbf{z}^*(t), \boldsymbol{\gamma}_A^*(t), \mathbf{u}(t)); \quad \mathbf{u}(t), \mathbf{u}^*(t) \in \mathbf{U} \quad (4.22)$$

Proposition 2. Let  $[p_1(t) \ p_2(t) \ \dots \ p_n(t)]^T = -(\mathbf{R}_3)^{-1}(\mathbf{B}^T \boldsymbol{\gamma}^*(t))$ ; if  $\mathbf{R}_3$  is a diagonal positive definite matrix, then the optimal control decisions  $\mathbf{u}^* = [u_1^* \ u_2^* \ \dots \ u_n^*]$  that minimizes  $\mathbf{H}_c(\mathbf{z}^*, \boldsymbol{\gamma}_A^*, \mathbf{u})$  is unique and can be formulated as

$$u_i^*(t) = \varphi(\mathbf{z}^*(t), \boldsymbol{\gamma}^*(t)) = \begin{cases} u_{min}, & \text{if } p_i(t) < u_{min} \\ u_{max}, & \text{if } p_i(t) > u_{max} \\ p_i(t), & \text{if } u_{min} \leq p_i(t) \leq u_{max} \end{cases} \quad (4.23)$$

Proof. If  $\mathbf{u}^* = [u_1^* \ u_2^* \ \dots \ u_n^*]$  minimizes  $\mathbf{H}_c(\mathbf{z}^*(t), \boldsymbol{\gamma}_A^*(t), \mathbf{u}(t))$ , then we have

$$\begin{aligned} & L(\mathbf{z}^*(t), \mathbf{u}^*(t)) + \boldsymbol{\gamma}^*(t) \mathbf{f}_1(\mathbf{z}^*(t), \mathbf{u}^*(t)) + \gamma_N^*(t) \mathbf{f}_2(\mathbf{z}^*(t), \mathbf{u}^*(t)) \\ & \leq L(\mathbf{z}^*(t), \mathbf{u}(t)) + \boldsymbol{\gamma}^*(t) \mathbf{f}_1(\mathbf{z}^*(t), \mathbf{u}(t)) + \gamma_N^*(t) \mathbf{f}_2(\mathbf{z}^*(t), \mathbf{u}(t)) \end{aligned} \quad (4.24)$$

Eq. (4.24) indicates

$$\begin{aligned} & 0.5 \cdot \mathbf{u}^*(t)^T \mathbf{R}_3 \mathbf{u}^*(t) + (\boldsymbol{\gamma}^*(t))^T \cdot \mathbf{B} \cdot \mathbf{u}^*(t) \\ & \leq 0.5 \cdot \mathbf{u}(t)^T \mathbf{R}_3 \mathbf{u}(t) + (\boldsymbol{\gamma}^*(t))^T \cdot \mathbf{B} \cdot \mathbf{u}(t) \end{aligned} \quad (4.25)$$

Let  $\mathbf{p}^*(t) = (\mathbf{R}_3)^{-1}(\mathbf{B}^T \boldsymbol{\gamma}^*(t)) = -[p_1 \ p_2 \ \dots \ p_n]^T$ . Then

$$(\boldsymbol{\gamma}^*(t))^T \cdot \mathbf{B} \cdot \mathbf{u}^*(t) = (\mathbf{u}^*(t))^T \mathbf{B}^T \boldsymbol{\gamma}^*(t) = (\mathbf{u}^*(t))^T \mathbf{R}_3 \mathbf{p}^*(t) \quad (4.26a)$$

$$(\boldsymbol{\gamma}^*(t))^T \cdot \mathbf{B} \cdot \mathbf{u}(t) = (\mathbf{u}(t))^T \mathbf{B}^T \boldsymbol{\gamma}^*(t) = (\mathbf{u}(t))^T \mathbf{R}_3 \mathbf{p}^*(t) \quad (4.26b)$$

Substituting Eq. (4.26) into Eq. (4.25), we have

$$\begin{aligned} & 0.5 \cdot \mathbf{u}^*(t)^T \mathbf{R}_3 \mathbf{u}^*(t) + (\mathbf{u}^*(t))^T \mathbf{R}_3 \mathbf{p}^*(t) \\ & \leq 0.5 \cdot \mathbf{u}(t)^T \mathbf{R}_3 \mathbf{u}(t) + (\mathbf{u}(t))^T \mathbf{R}_3 \mathbf{p}^*(t) \end{aligned} \quad (4.27)$$

Adding  $0.5 \cdot \mathbf{p}^*(t)^T \mathbf{R}_3 \mathbf{p}^*(t) = 0.5(\boldsymbol{\gamma}^*(t))^T \cdot \mathbf{B}(\mathbf{R}_3)^{-1} \mathbf{B}^T \boldsymbol{\gamma}^*(t)$  to both sides of inequality (4.27), we have

$$0.5[\mathbf{u}^*(t) + \mathbf{p}^*(t)]^T \mathbf{R}_3 [\mathbf{u}^*(t) + \mathbf{p}^*(t)] \leq 0.5[\mathbf{u}(t) + \mathbf{p}^*(t)]^T \mathbf{R}_3 [\mathbf{u}(t) + \mathbf{p}^*(t)] \quad (4.28)$$

Inequality (4.28) implies that if  $\mathbf{u}^*$  minimizes  $\mathbf{H}_c(\mathbf{z}^*(t), \boldsymbol{\gamma}_A^*(t), \mathbf{u}(t))$ , it must minimize inequality

(4.27) and vice versa. Thereby

$$\mathbf{u}^*(t) = \min_{\mathbf{u} \in \mathbf{U}} [\mathbf{u}(t) + \mathbf{p}^*(t)]^T \mathbf{R}_3 [\mathbf{u}(t) + \mathbf{p}^*(t)] \quad (4.29)$$

Note  $\mathbf{R}_3$  is a diagonal positive definite matrix; without loss of generality, let  $\mathbf{R}_3 = \text{diag}([\omega_1, \omega_2 \dots, \omega_n])$ ,  $\omega_i > 0, \forall i = 1, 2, \dots, n$ . Then, inequality (4.29) can be written as

$$\begin{aligned} \mathbf{u}^*(t) &= \min_{\mathbf{u} \in \mathbf{U}} \sum_{i=1}^n \omega_i [u_i(t) - p_i]^2 \\ &= \sum_{i=1}^n \min_{u_{\min} \leq u_i \leq u_{\max}} \omega_i [u_i(t) - p_i]^2 \end{aligned} \quad (4.30)$$

The only solution to the above inequality is

$$u_i^*(t) = \begin{cases} u_{\min}, & \text{if } p_i(t) < u_{\min} \\ u_{\max}, & \text{if } p_i(t) > u_{\max} \\ p_i(t), & \text{if } u_{\min} \leq p_i(t) \leq u_{\max} \end{cases} ; \forall i = 1, 2, \dots, n \quad (4.31)$$

This completes the proof. ■

Eq. (4.13b), Eq. (4.13c), Eq. (4.20a), Eq. (4.20b) and Eq. (4.23) form a two-point boundary value problem as follows with initial conditions and terminal conditions provided by Eq.(12e) and Eq. (4.21), respectively.

$$\dot{\mathbf{z}}(t) = \mathbf{A} \cdot \mathbf{z}(t) + \mathbf{B} \cdot \varphi(\mathbf{z}(t), \boldsymbol{\gamma}(t)) \quad (4.32a)$$

$$\dot{z}_N(t) = \sum_{i=1}^n (z_{N,1}^i + z_{,2}^i + z_{N,3}^i) \quad (4.32b)$$

$$\dot{\boldsymbol{\gamma}}(t) = -\mathbf{A} \cdot \boldsymbol{\gamma}(t) - \begin{bmatrix} \mathbf{C}_x \\ \mathbf{C}_y \end{bmatrix} \boldsymbol{\gamma}_N(t) - \mathbf{Q}_1 \mathbf{z}(t) + \beta \boldsymbol{\gamma}(t) \quad (4.32c)$$

$$\dot{\boldsymbol{\gamma}}_N(t) = \beta \cdot \boldsymbol{\gamma}_N(t) \quad (4.32d)$$

$$\mathbf{z}(0) = [\mathbf{x}_0^T \quad \mathbf{y}_0^T]^T; z_N(0) = 0; \quad (4.32e)$$

$$\boldsymbol{\gamma}(T_P) = \mathbf{Q}_2 \mathbf{z}(T_P), \boldsymbol{\gamma}_N(T_P) = e^{\beta T_P} \cdot \mathbf{M} \cdot 2 \cdot z_N(T_P) \quad (4.32f)$$

The two-point boundary value problem can be solved using many existing solution algorithms. A review of these algorithms is provided in Kirk (2012). In this study, the shooting method is used to solve the two-point boundary value problem (4.32). The details of implementing the shooting method can be found in Keller (1976). The main advantage of the shooting method is that it converges very fast if the algorithm starts to converge (Keller, 1976). Note,  $\partial^2 \mathbf{H}_c / \partial (\mathbf{u}(t))^2 = \mathbf{R}_3$  is a positive definite matrix. Thereby, the solution  $(\mathbf{z}^*(t), z_N^*(t), \boldsymbol{\gamma}^*(t), \boldsymbol{\gamma}_N^*(t))$  of the two-point boundary value problem (4.32) is a minimum solution of optimal control problem (4.5). The

optimal control  $\mathbf{u}^*(t)$  can be obtained by inputting  $\boldsymbol{\gamma}^*(t)$  into Eq. (4.23).

#### 4.4 Sensitivity analysis of the optimal control problem

For the DMPC approach, at each sampling time instant  $t_k$ , the control decisions are determined by solving the two-point boundary value problem (4.32) with the predicted spacing error and relative speed of vehicle 1 with respect to the leading vehicle (i.e.,  $\hat{x}_1(t_k)$  and  $\hat{y}_1(t_k)$ ). The resulting control decisions may deviate significantly from those of the idealized MPC strategy due to errors in predicting  $x_1(t_k)$  and  $y_1(t_k)$ , which can decrease the platoon performance and cause collisions. To address this issue, the DMPC-FOA approach corrects the estimated control decisions of the DMPC approach using first-order Taylor approximation. To do so, the main step is to obtain the derivatives of the optimal solution of the state and costate variables with respect to  $\tilde{x}_1(t_k)$  and  $\tilde{y}_1(t_k)$  in the DMPC-FOA approach, respectively.

The sensitivity analysis of an optimal control problem quantitatively measures the change in the optimal solution of the state and costate variables induced by a unit change in the perturbed parameters (i.e.,  $\tilde{x}_1(t_k)$  and  $\tilde{y}_1(t_k)$  in this study). Parametric sensitivity of optimal problem has been extensively studied. Dorato (1963) developed an analytical model to study the variation of the objective function with respect to parametric perturbations. Malanowski (1984, 1987) discussed the conditions for directional differentiability of the solutions for an optimal control problem with nonlinear ordinary dynamics. Maurer and Pesch (1984) developed an analytical method for sensitivity analysis of optimal control problems with no constraints. This method is further extended to study the sensitivity analysis of optimal control problems with control constraints (Maurer and Pesch, 1995; Malanowski and Maurer, 1996), and pure state variable constraints (Augustin and Maurer, 2001; Malanowski, 2011). Here, the analytical method for sensitivity analysis of the optimal control decisions with respect to  $\tilde{x}_1(t_k)$  and  $\tilde{y}_1(t_k)$  will be derived by modifying the method developed by Maurer and Pesch (1995) for a general optimal control problem.

Denote  $\tilde{\mathbf{u}}^*(t) = [\tilde{u}_1^*(t), \dots, \tilde{u}_n^*(t)]$  as the control decisions obtained by solving Eq. (4.32) using  $\tilde{x}_1(t_k)$  and  $\tilde{y}_1(t_k)$  predicted by the DMPC-FOA approach. The corresponding solutions for the state variables (i.e.,  $\mathbf{z}(t)$ ,  $z_N(t)$ ) and costate variables (i.e.,  $\boldsymbol{\gamma}(t)$ ,  $\gamma(t)$ ) are denoted as  $\tilde{\mathbf{z}}^*(t)$ ,  $\tilde{z}_N^*(t)$ ,  $\tilde{\boldsymbol{\gamma}}^*(t)$  and  $\tilde{\gamma}_N^*(t)$ , respectively. Let the derivatives of the optimal solutions for the state and costate variables with respect to  $\tilde{x}_1(t_k)$  be defined as follows:

$$\mathbf{h}_{\tilde{x}_1}(t) = \frac{\partial \tilde{\mathbf{z}}^*(t)}{\partial \tilde{x}_1(t_k)}; h_{N, \tilde{x}_1}(t) = \frac{\partial \tilde{z}_N^*(t)}{\partial \tilde{x}_1(t_k)}$$

$$\boldsymbol{\eta}_{\tilde{x}_1}(t) = \frac{\partial \tilde{\boldsymbol{\gamma}}^*(t)}{\partial \tilde{x}_1(t_k)}; \eta_{N, \tilde{x}_1}(t) = \frac{\partial \tilde{\gamma}_N^*(t)}{\partial \tilde{x}_1(t_k)}.$$

According to  $\tilde{u}_i^*(t)$ , we can obtain the set of time intervals  $\Omega_{i,1}$ ,  $\Omega_{i,2}$ , and  $\Omega_{i,2}$  ( $\Omega_{i,1} \cup \Omega_{i,2} \cup \Omega_{i,2} =$

$[0, T_p]$ ) for each vehicle  $i, i = 1, 2, \dots, n$  such that

$$\tilde{u}_i^*(t) = \begin{cases} u_{min}, t \in \Omega_{i,1} \\ u_{max}, t \in \Omega_{i,2} \\ \tilde{p}_i, t \in \Omega_{i,3} \end{cases} \quad (4.33)$$

where  $[\tilde{p}_1(t) \quad \tilde{p}_2(t) \quad \dots \quad \tilde{p}_n(t)] = -(\mathbf{R}_3)^{-1}(\mathbf{B}^T \tilde{\boldsymbol{\gamma}}^*(t))$ .

Then, according to Eq. (4.33), we have

$$\frac{d\tilde{u}_i^*(t)}{d\tilde{x}_1(t_k)} = \begin{cases} 0, t \in (\Omega_{i,1} \cup \Omega_{i,2}) \\ m_{\tilde{x}_1, i}(t), t \in \Omega_{i,3} \end{cases} \quad (4.34a)$$

where

$$[m_{\tilde{x}_1, 1}(t) \quad m_{\tilde{x}_1, 2}(t) \quad \dots \quad m_{\tilde{x}_1, n}(t)]^T = -(\mathbf{R}_3)^{-1}(\mathbf{B}^T \boldsymbol{\eta}_{\tilde{x}_1}(t)). \quad (4.34b)$$

Let  $\Psi(\boldsymbol{\eta}_{\tilde{x}_1}(t)) = \left[ \frac{d\tilde{u}_1^*(t)}{d\tilde{x}_1(t_k)} \quad \frac{d\tilde{u}_2^*(t)}{d\tilde{x}_1(t_k)} \quad \dots \quad \frac{d\tilde{u}_n^*(t)}{d\tilde{x}_1(t_k)} \right]^T$ . Differentiating both sides of Eqs. (32a)-(32g) with respect to  $\tilde{x}_1(t_k)$ , we have

$$\dot{\mathbf{h}}_{\tilde{x}_1}(t) = \mathbf{A} \cdot \mathbf{h}_{\tilde{x}_1} + \mathbf{B} \cdot \Psi(\boldsymbol{\eta}_{\tilde{x}_1}(t)) \quad (4.35a)$$

$$\dot{h}_{N, \tilde{x}_1} = [\mathbf{C}_x^T \quad \mathbf{C}_y^T] \cdot \mathbf{h}_{\tilde{x}_1} \quad (4.35b)$$

$$\dot{\boldsymbol{\eta}}_{\tilde{x}_1} = -\mathbf{A} \cdot \boldsymbol{\eta}_{\tilde{x}_1}(t) - \begin{bmatrix} \mathbf{C}_x \\ \mathbf{C}_y \end{bmatrix} \boldsymbol{\eta}_{N, \tilde{x}_1}(t) - \mathbf{Q}_1 \mathbf{h}_{\tilde{x}_1} + \beta \boldsymbol{\eta}_{\tilde{x}_1}(t) \quad (4.35c)$$

$$\dot{\eta}_{N, \tilde{x}_1}(t) = \beta \cdot \eta_{N, \tilde{x}_1}(t) \quad (4.35d)$$

with initial and terminal conditions as:

$$\mathbf{h}_{\tilde{x}_1}(0) = \frac{\partial \tilde{\mathbf{z}}(0)}{\partial \tilde{x}_1(t_k)} = \frac{\partial \tilde{\mathbf{z}}(t_k)}{\partial \tilde{x}_1(t_k)} = [1, \mathbf{0}_{1 \times 2n-1}]^T \quad (4.35e)$$

$$h_{N, \tilde{x}_1}(0) = \frac{\partial \tilde{z}_N(0)}{\partial \tilde{x}_1(t_k)} = \frac{\partial(0)}{\partial \tilde{x}_1(t_k)} = 0 \quad (4.35f)$$

$$\boldsymbol{\eta}_{\tilde{x}_1}(T_p) = \frac{\partial \tilde{\boldsymbol{\gamma}}_1(T_p)}{\partial \tilde{x}_1(t_k)} = \frac{\partial(\mathbf{Q}_2 \tilde{\mathbf{z}}(T_p))}{\partial \tilde{x}_1(t_k)} = \mathbf{Q}_2 \cdot \mathbf{h}_{\tilde{x}_1}(T_p) \quad (4.35g)$$

$$\eta_{N, \tilde{x}_1}(T_p) = \frac{\partial \tilde{\boldsymbol{\gamma}}_N(T_p)}{\partial \tilde{x}_1(t_k)} = \frac{\partial(e^{\beta T_p} \cdot \mathbf{M} \cdot 2 \cdot \tilde{z}_N(T_p))}{\partial \tilde{x}_1(t_k)} = e^{\beta T_p} \cdot \mathbf{M} \cdot 2 \cdot h_{N, \tilde{x}_1}(T_p) \quad (4.35h)$$

where  $\mathbf{0}_{1 \times 2n-1}$  is a  $(2n - 1)$ -dimensional zero vector. Eqs. (4.35a)-(4.35h) also form a two-point boundary value problem which can be solved using the shooting method.

To obtain the derivatives of the optimal state and costate variables with respect to  $\tilde{y}_1(t_k)$ , similarly,

let

$$\mathbf{h}_{\tilde{y}_1}(t) = \frac{\partial \tilde{\mathbf{z}}^*(t)}{\partial \tilde{y}_1(t_k)}; \quad h_{N,\tilde{y}_1}(t) = \frac{\partial \tilde{z}_N^*(t)}{\partial \tilde{y}_1(t_k)} \quad (4.36a)$$

$$\boldsymbol{\eta}_{\tilde{y}_1}(t) = \frac{\partial \tilde{\boldsymbol{\gamma}}^*(t)}{\partial \tilde{y}_1(t_k)}; \quad \eta_{N,\tilde{y}_1}(t) = \frac{\partial \tilde{\gamma}_N^*(t)}{\partial \tilde{y}_1(t_k)}. \quad (4.36b)$$

Differentiating both sides of Eqs. (4.32a)-(4.32f) with respect to  $\tilde{y}_1(t_k)$ , we can obtain a similar two-point boundary value problem, as follows:

$$\dot{\mathbf{h}}_{\tilde{y}_1}(t) = \mathbf{A} \cdot \mathbf{h}_{\tilde{y}_1} + \mathbf{B} \cdot \Psi(\boldsymbol{\eta}_{\tilde{y}_1}(t)) \quad (4.37a)$$

$$\dot{h}_{N,\tilde{y}_1} = [\mathbf{C}_x^T \quad \mathbf{C}_y^T] \mathbf{h}_{\tilde{y}_1} \quad (4.37b)$$

$$\dot{\boldsymbol{\eta}}_{\tilde{y}_1} = -\mathbf{A} \cdot \boldsymbol{\eta}_{\tilde{y}_1}(t) - \begin{bmatrix} \mathbf{C}_x \\ \mathbf{C}_y \end{bmatrix} \eta_{N,\tilde{y}_1}(t) - \mathbf{Q}_1 \mathbf{h}_{\tilde{y}_1} + \beta \boldsymbol{\eta}_{\tilde{y}_1}(t) \quad (4.37c)$$

$$\dot{\eta}_{N,\tilde{y}_1}(t) = \beta \cdot \eta_{N,\tilde{y}_1}(t) \quad (4.37d)$$

with initial and terminal conditions as:

$$\mathbf{h}_{\tilde{y}_1}(0) = \frac{\partial \tilde{\mathbf{z}}(0)}{\partial \tilde{y}_1(t_k)} = \frac{\partial \tilde{\mathbf{z}}(t_k)}{\partial \tilde{y}_1(t_k)} = [\mathbf{0}_{1 \times n}, 1, \mathbf{0}_{1 \times n-1}]^T \quad (4.37e)$$

$$h_{N,\tilde{y}_1}(0) = \frac{\partial \tilde{z}_N(0)}{\partial \tilde{y}_1(t_k)} = \frac{\partial(0)}{\partial \tilde{y}_1(t_k)} = 0 \quad (4.37f)$$

$$\boldsymbol{\eta}_{\tilde{y}_1}(T_P) = \frac{\partial \tilde{\boldsymbol{\gamma}}_1(T_P)}{\partial \tilde{y}_1(t_k)} = \frac{d(\mathbf{Q}_2 \tilde{\mathbf{z}}(T_P))}{d\tilde{y}_1(t_k)} = \mathbf{Q}_2 \cdot \mathbf{h}_{\tilde{y}_1}(T_P) \quad (4.37g)$$

$$\eta_{N,\tilde{y}_1}(T_P) = \frac{\partial \tilde{\gamma}_N(T_P)}{\partial \tilde{y}_1(t_k)} = \frac{\partial(e^{\beta T_P} \cdot \mathbf{M} \cdot 2 \cdot \tilde{z}_N(T_P))}{\partial \tilde{y}_1(t_k)} = e^{\beta T_P} \cdot \mathbf{M} \cdot 2 \cdot h_{N,\tilde{y}_1}(T_P) \quad (4.37h)$$

where  $\mathbf{0}_{1 \times n-1}$  is a  $(n - 1)$ -dimensional zero vector. The vector of functions  $\Psi(\boldsymbol{\eta}_{\tilde{y}_1}(t))$  is similar to  $\Psi(\boldsymbol{\eta}_{\tilde{x}_1}(t))$ . It is formulated by replacing the subscript “ $\tilde{x}_1$ ” in Eq. (4.34) with “ $\tilde{y}_1$ ”.

The derivatives of the optimal solutions for the state and costate variables with respect to  $\tilde{x}_1(t_k)$  and  $\tilde{y}_1(t_k)$  can be obtained by solving the two-point boundary value problems (4.35) and (4.37), respectively. Then, when the actual value of  $x_1(t_k)$  and  $y_1(t_k)$  are detected at the sampling time instant  $t_k$ , the optimal solution of the state and costate variables of the idealized MPC strategy can be estimated using first-order Taylor approximation, as follows

$$\bar{\mathbf{z}}^*(t) = \tilde{\mathbf{z}}^*(t) + \mathbf{h}_{\tilde{x}_1}(t)(x_1(t_k) - \tilde{x}_1(t_k)) + \mathbf{h}_{\tilde{y}_1}(t)(y_1(t_k) - \tilde{y}_1(t_k)) \quad (4.38a)$$

$$\bar{\boldsymbol{\gamma}}^*(t) = \tilde{\boldsymbol{\gamma}}^*(t) + \boldsymbol{\eta}_{\tilde{x}_1}(t)(x_1(t_k) - \tilde{x}_1(t_k)) + \boldsymbol{\eta}_{\tilde{y}_1}(t)(y_1(t_k) - \tilde{y}_1(t_k)) \quad (4.38b)$$

Eq. (4.38a) and Eq. (4.38b) can be calculated instantaneously at the sampling time instant  $t_k$  as

$\mathbf{h}_{\tilde{x}_1}(t)$ ,  $\mathbf{h}_{\tilde{y}_1}(t)$ ,  $\boldsymbol{\eta}_{\tilde{x}_1}(t)$  and  $\boldsymbol{\eta}_{\tilde{y}_1}(t)$  are obtained before  $t_k$ . Eq. (4.38) indicates that compared to  $[\tilde{\mathbf{z}}^*(t), \tilde{\boldsymbol{\gamma}}^*(t)]$ ,  $[\bar{\mathbf{z}}^*(t), \bar{\boldsymbol{\gamma}}^*(t)]$  are closer to  $[\mathbf{z}^*(t), \boldsymbol{\gamma}^*(t)]$  calculated for the idealized MPC strategy using exact  $x_1(t_k)$  and  $y_1(t_k)$ . According to Eq. (4.23), the optimal control decisions of the idealized MPC strategy can be estimated as

$$\bar{u}_i^*(t) = \varphi(\bar{\mathbf{z}}^*(t), \bar{\boldsymbol{\gamma}}^*(t)) = \begin{cases} u_{min}, & \text{if } \bar{p}_i(t) < u_{min} \\ u_{max}, & \text{if } \bar{p}_i(t) > u_{max} \\ \bar{p}_i(t), & \text{if } u_{min} \leq \bar{p}_i(t) \leq u_{max} \end{cases} ; \forall i = 1, 2, \dots, n \quad (4.39)$$

where  $[\bar{p}_1(t) \ \bar{p}_2(t) \ \dots \ \bar{p}_n(t)]^T = -(\mathbf{R}_3)^{-1}(\mathbf{B}^T \bar{\boldsymbol{\gamma}}^*(t))$ . Compared to  $\tilde{\mathbf{u}}^*(t)$ , the estimated  $\bar{\mathbf{u}}^*(t)$ ,  $(\bar{\mathbf{u}}^*(t) = [\bar{u}_1^*(t) \ \bar{u}_2^*(t) \ \dots \ \bar{u}_n^*(t)]^T)$  is closer to  $\mathbf{u}^*(t)$  calculated using the idealized MPC strategy as  $\bar{\boldsymbol{\gamma}}^*(t)$  is closer to  $\boldsymbol{\gamma}^*(t)$  compared to  $\tilde{\boldsymbol{\gamma}}^*(t)$ .

**Proposition 3:** If the inequality constraints (4.5c), (4.5d) and (4.5e) are not active along the trajectory of the optimal solution  $(\tilde{\mathbf{z}}^*(t), \tilde{z}^*(t), \tilde{\boldsymbol{\gamma}}^*(t), \tilde{\gamma}^*(t))$  obtained with the predicted initial state  $\tilde{x}_1(t_k)$  and  $\tilde{y}_1(t_k)$ , then the derivatives of optimal solutions for the state and costate variables with respect to  $\tilde{x}_1(t_k)$  and  $\tilde{y}_1(t_k)$  are the same for all solutions of  $(\tilde{\mathbf{z}}^*(t), \tilde{z}^*(t), \tilde{\boldsymbol{\gamma}}^*(t), \tilde{\gamma}^*(t))$  for which the inequality constraints (5c) and (5d) are not active.

**Proof:** If the inequality constraints (4.5c), (4.5d) and (4.5e) are not active along the optimal solution,  $\tilde{z}_N^*(t) \equiv 0, t \in [0, T_p]$ . According to Eq. (4.16d),  $\tilde{\gamma}_N^*(T_p) = 2 M \cdot \tilde{z}_N^*(T_p) = 2 M \cdot 0 = 0$ . Based on Eq. (4.32e),  $\tilde{\gamma}_N^*(t) \equiv 0, t \in [0, T_p]$ . This indicates that  $\eta_{N, \tilde{x}_1}(t) = \eta_{N, \tilde{y}_1}(t) \equiv 0, t \in [0, T_p]$ . In addition,  $\Psi(\boldsymbol{\eta}_{\tilde{x}_1}(t)) = -(\mathbf{R}_3)^{-1}(\mathbf{B}^T \boldsymbol{\eta}_{\tilde{x}_1}(t))$  and  $\Psi(\boldsymbol{\eta}_{\tilde{y}_1}(t)) = -(\mathbf{R}_3)^{-1}(\mathbf{B}^T \boldsymbol{\eta}_{\tilde{y}_1}(t))$ . Thereby, the two-point boundary value problems (4.35) and (4.37) are the same for different optimal solutions under which the inequality constraints (4.5c), (4.5d) and (4.5e) are not active. This indicates that the derivatives of the optimal solutions for the state and costate variables with respect to  $\tilde{x}_1(t_k)$  and  $\tilde{y}_1(t_k)$  are the same for all of these solutions. ■

Proposition 3 implies that if under the optimal control decisions, the following vehicles in the platoon do not brake and accelerate at the maximum values, the speed is within the speed limit, and the spacing between all adjacent vehicle pairs is larger than the minimum spacing during time interval  $[t_k, t_k + T_p]$ , the changes in the optimal control decisions for a unit change in  $\tilde{x}_1(t_k)$  and  $\tilde{y}_1(t_k)$  would be the same for all of these optimal control decisions. It is worth noting that the idealized MPC strategy can coordinate the behaviors of all following vehicles to minimize the objective function efficiently. It can enable smoother deceleration and acceleration behavior of all following vehicles even if the leading vehicle decelerates or accelerates at the maximum value. The following vehicles accelerate or decelerate at the maximum value only when the spacing between two consecutive vehicles is too large or too small. Thereby, according to Proposition 3, under normal conditions, the derivatives of the optimal solutions for the state and costate variables, i.e.,  $(\tilde{\mathbf{z}}(t), \tilde{z}_N(t), \tilde{\boldsymbol{\gamma}}(t), \tilde{\gamma}_N(t))$  with respect to  $\tilde{x}_1(t_k)$  and  $\tilde{y}_1(t_k)$  are the same and are independent of these solutions. Let  $\mathbf{h}_l^*(t), h_{N,l}^*(t), \boldsymbol{\eta}_l^*(t), \eta_{N,l}^*(t), l \in \{\tilde{x}_1, \tilde{y}_1\}, t \in [0, T_p]$  be the corresponding derivatives. These derivatives can be obtained offline to avoid solving the two-point boundary value problems (4.35) and (4.37) in real time. Thereby, under normal situations when the inequality constraints (4.5c), (4.5d) and (4.5e) are not active along the optimal solution, the time reserved for

computing in DMPC-FOA approach can be the same as that of the DMPC approach.

Further, when the inequality constraints are active frequently for some traffic flow conditions (e.g., very congested flow), the two-point boundary value problems (4.35) and (4.37) need to be solved in real time.  $\mathbf{h}_l^*(t), h_{N,l}^*(t), \boldsymbol{\eta}_l^*(t), \eta_{N,l}^*(t), l \in \{\tilde{x}_1, \tilde{y}_1\}, t \in [0, T_p]$  can be used as the initial point for the shooting method to solve the two-point boundary value problems. This can significantly reduce the computational time for solving the two problems as they are closer to the optimal solution. This property enhances the applicability of the proposed DMPC-FOA approach for controlling the CAV platoon in real-time.

#### 4.5 Stability analysis of the idealized MPC strategy with no inequality constraints

Stability is an important property for a CAV platoon. It indicates the capability of a platoon to recover to a stable state after external disturbances on the platoon formation (e.g., unexpected hard acceleration and deceleration of the leading vehicle). In this study, the condition for asymptotic stability of the idealized MPC strategy is analyzed to ensure that the CAV platoon can dampen traffic oscillations efficiently. This condition also ensures the local stability of the DMPC-FOA approaches as it is proposed to characterize the control decisions of the idealized MPC strategy. Similar to Gong et al., (2016), the stability analysis of the idealized MPC strategy is based on optimal control problem (4.5) with no inequality constraints as they are not active in most traffic flow scenarios. The conditions for asymptotic stability of the idealized MPC strategy with active constraints will be investigated in our future work.

For convenience of stability analysis, in the following, optimal control problem (4.5) without inequality constraints (4.5c) and (4.5d) is transformed into an equivalent form for analyzing stability. The conditions for asymptotic stability of the unconstrained idealized MPC strategy are analyzed using the stability theorem for continuous MPC problems developed by Mayne et.al. (2000). Let

$$\mathbf{z}_\beta(t) = e^{-\frac{\beta}{2}t} \mathbf{z}(t) \quad (4.40a)$$

$$\mathbf{u}_\beta(t) = e^{-\frac{\beta}{2}t} \mathbf{u}(t) \quad (4.40b)$$

Then, optimal control problem (4.5) without inequality constraints (4.5c) and (4.5d) can be formulated as

$$\min_{\mathbf{u}_\beta} \int_0^{T_p} [\mathbf{z}_\beta(t)^T \mathbf{Q}_1 \mathbf{z}_\beta(t) + \mathbf{u}_\beta(t)^T \mathbf{R}_3 \mathbf{u}_\beta(t)] dt + \mathbf{z}_\beta(T_p)^T \mathbf{Q}_2 \mathbf{z}_\beta(T_p) \quad (4.41a)$$

$$\text{s.t } \dot{\mathbf{z}}_\beta(t) = \left( \mathbf{A} - \frac{\beta}{2} \mathbf{E}_{2n} \right) \mathbf{z}_\beta(t) + \mathbf{B} \mathbf{u}_\beta(t) \quad (4.41b)$$

$$\mathbf{z}_\beta(0) = [\mathbf{x}_k \quad \mathbf{y}_k]^T \quad (4.41c)$$

The following theorem is used to analyze the asymptotical stability of the idealized MPC strategy with no inequality constraints.

Theorem 1 (Mayne et.al. 2000): Consider the following continuous constrained MPC problem

$$\begin{aligned} & \min_{\mathbf{a}} \int_0^{T_p} L(\mathbf{z}(t), \mathbf{u}(t)) dt + F(\mathbf{z}(T_p)) \\ \text{s.t.} \quad & \dot{\mathbf{z}} = g(\mathbf{z}, \mathbf{u}) \\ & \mathbf{z}(t) \in \mathcal{Z}, \text{ for } t \in [0, T_p] \\ & \mathbf{u}(t) \in \mathcal{A}, \text{ for } t \in [0, T_p] \\ & \mathbf{z}(T_p) \in \mathcal{Z}_f \end{aligned}$$

where  $\mathbf{z}$  and  $\mathbf{u}$  are vectors of the state variables and control variables, respectively.  $\mathbf{z}(T_p)$  is the value of  $\mathbf{z}(t)$  at terminal time  $T_p$ .  $\mathcal{Z}$ ,  $\mathcal{A}$ , and  $\mathcal{Z}_f$  are the feasible sets for  $\mathbf{z}(t)$ ,  $\mathbf{u}(t)$  and  $\mathbf{z}(T_p)$ , respectively. If there exists a nominal controller  $\kappa(\mathbf{z})$  such that the following four conditions hold for the above continuous MPC problem, then it is asymptotic stable.

- (1).  $0 \in \mathcal{Z}$
- (2).  $\kappa(\mathbf{z}) \in \mathcal{A}, \forall \mathbf{z} \in \mathcal{Z}_f$
- (3).  $g(\mathbf{z}, \kappa(\mathbf{z})) \in \mathcal{Z}_f$  for  $\forall \mathbf{z} \in \mathcal{Z}_f$
- (4).  $[\dot{F} + L](\mathbf{z}, \kappa(\mathbf{z})) \leq 0$  for  $\forall \mathbf{z} \in \mathcal{Z}_f$

To enable application of Theorem 1 for stability analysis of the unconstrained idealized MPC strategy based on optimal control problem (4.41), let

$$\mathbf{z}(t) = \mathbf{z}_\beta(t) \tag{4.42a}$$

$$\mathbf{u}(t) = \mathbf{u}_\beta(t) \tag{4.42b}$$

$$\dot{\mathbf{z}}(t) = g(\mathbf{z}, \mathbf{u}) = \left( \mathbf{A} - \frac{\beta}{2} \mathbf{E}_{2n} \right) \mathbf{z}(t) + \mathbf{B}\mathbf{u}(t) \tag{4.42c}$$

$$L(\mathbf{z}(t), \mathbf{u}(t)) = \mathbf{z}(t)^T \mathbf{Q}_1 \mathbf{z}(t) + \mathbf{u}(t)^T \mathbf{R}_3(t) \tag{4.42d}$$

$$F(\mathbf{z}(t)) = \mathbf{z}(t)^T \mathbf{Q}_2 \mathbf{z}(t) \tag{4.42e}$$

$$\dot{F}(\mathbf{z}(t)) = \dot{\mathbf{z}}(t)^T \mathbf{Q}_2 \mathbf{z}(t) + \mathbf{z}(t)^T \mathbf{Q}_2 \dot{\mathbf{z}}(t) \tag{4.42f}$$

This study chooses a linear nominal controller (Camacho and Alba, 2013) as follows

$$\kappa(\mathbf{z}) = \mathcal{K}\mathbf{z} \tag{4.43}$$

Let  $\mathcal{K} = \mathbf{0}_{2n \times n}$ . This choice of matrix  $\mathcal{K}$  will simplify the analysis of conditions for asymptotic stability of the unconstrained idealized MPC strategy based on optimal control problem (4.41). Next, we illustrate the conditions for which optimal control problem (4.41) can satisfy the four conditions in Theorem 1.

For optimal control problem (4.41), the feasible set of state variables, control variables, and terminal state variables are  $\mathcal{Z} = \mathbb{R}^{2n}$ ,  $\mathcal{A} = \mathbb{R}^n$ , and  $\mathcal{Z}_f = \mathbb{R}^{2n}$ , respectively. Thereby,  $0 \in \mathcal{Z}$ ; condition 1 is satisfied. According to Eq. (4.43),  $\kappa(\mathbf{z}) = \mathcal{K}\mathbf{z} = \mathbf{0}_{1 \times n} \in \mathbb{R}^n = \mathcal{A}$ . Hence, condition 2 in Theorem 1 is also satisfied. From Eq. (4.42c) and Eq. (4.43),  $g(\mathbf{z}, \kappa(\mathbf{z})) = \left( \mathbf{A} - \frac{\beta}{2} \mathbf{E}_{2n} \right) \mathbf{z}(t) + \mathbf{B}\mathcal{K}\mathbf{z}(t) = \left( \mathbf{A} - \frac{\beta}{2} \mathbf{E}_{2n} \right) \mathbf{z}(t) \in \mathbb{R}^{2n} = \mathcal{Z}_f$ . Therefore, condition 3 holds for optimal control problem (4.41).

To illustrate that condition 4 is satisfied, for simplicity, the notation for time  $t$  is removed. Substituting Eqs. (42c)-(42f) into the inequality in condition 4, we have

$$\begin{aligned} & \left[ \left( A - \frac{\beta}{2} E_{2n} \right) \mathbf{z} + \mathbf{B}\mathcal{K}\mathbf{z} \right]^T \mathbf{Q}_2 \mathbf{z} + \mathbf{z}^T \mathbf{Q}_2 \left[ \left( A - \frac{\beta}{2} E_{2n} \right) \mathbf{z} + \mathbf{B}\mathcal{K}\mathbf{z} \right] \\ & + \mathbf{z}^T \mathbf{Q}_1 \mathbf{z} + (\mathcal{K}\mathbf{z})^T \mathbf{R}_3 (\mathcal{K}\mathbf{z}) \leq 0 \end{aligned} \quad (4.44)$$

Note  $\mathcal{K} = \mathbf{0}_{2n \times n}$ ; hence, inequality (4.44) can be simplified as

$$\mathbf{z}^T \left[ \left( A - \frac{\beta}{2} E_{2n} \right)^T \mathbf{Q}_2 + \mathbf{Q}_2 \left( A - \frac{\beta}{2} E_{2n} \right) + \mathbf{Q}_1 \right] \mathbf{z} \leq 0 \quad (4.45)$$

Let  $\mathbf{W} = \left( A - \frac{\beta}{2} E_{2n} \right)^T \mathbf{Q}_2 + \mathbf{Q}_2 \left( A - \frac{\beta}{2} E_{2n} \right) + \mathbf{Q}_1$ . Obviously, inequality (4.45) holds if matrix  $\mathbf{W}$  is negative semidefinite. According to Eq. (4.6),  $\mathbf{R}_1 = \Lambda^T \mathbf{D}_a \Lambda$ ,  $\mathbf{R}_2 = \Lambda^T \mathbf{D}_b \Lambda$ ,  $\mathbf{R}_4 = \Lambda^T \mathbf{D}_c \Lambda$ , and  $\mathbf{R}_5 = \Lambda^T \mathbf{D}_e \Lambda$ , where  $\Lambda$  is an  $n \times n$  orthogonal matrix and  $\Lambda^T \Lambda = \Lambda \Lambda^T = \mathbf{E}_n$ . Let the diagonal positive definite matrices  $\mathbf{D}_a$ ,  $\mathbf{D}_b$ ,  $\mathbf{D}_c$  and  $\mathbf{D}_e$  be  $\mathbf{D}_a = \text{diag}(a_1, \dots, a_n)$ ,  $\mathbf{D}_b = \text{diag}(b_1, \dots, b_n)$ ,  $\mathbf{D}_c = \text{diag}(c_1, \dots, c_n)$ , and  $\mathbf{D}_e = \text{diag}(e_1, \dots, e_n)$ , respectively, where  $a_i > 0$ ,  $b_i > 0$ ,  $c_i > 0$ , and  $e_i > 0$  for  $i = 1, \dots, n$ . The following proposition discusses the sufficient conditions for matrix  $\mathbf{W}$  to be negative semidefinite

Proposition 4.  $\mathbf{W}$  ( $\mathbf{W} \in \mathbb{R}^{2n \times 2n}$ ) is a negative semidefinite matrix if matrices  $\mathbf{D}_a$ ,  $\mathbf{D}_b$ ,  $\mathbf{D}_c$  and  $\mathbf{D}_e$ , and the discount parameter  $\beta$  are set such that

$$a_i < \beta c_i, \forall i = 1, 2, \dots, n \quad (4.46a)$$

$$e_i \geq \frac{-c_i^2}{\beta(a_i - \beta c_i)}, \forall i = 1, 2, \dots, n \quad (4.46b)$$

$$b_i \leq \frac{c_i^2 + \beta e_i(a_i - \beta c_i)}{a_i - \beta c_i}, \forall i = 1, 2, \dots, n \quad (4.46c)$$

for  $\forall i$ .

Proof. Matrix  $\mathbf{W}$  can be expanded as

$$\begin{aligned} \mathbf{W} &= \left( A - \frac{\beta}{2} E_n \right)^T \mathbf{Q}_2 + \mathbf{Q}_2 \left( A - \frac{\beta}{2} E_n \right) + \mathbf{Q}_1 \\ &= \begin{bmatrix} \mathbf{0}_n & \mathbf{0}_n \\ -\mathbf{E}_n & \mathbf{0}_n \end{bmatrix} \begin{bmatrix} \mathbf{R}_4 & \\ & \mathbf{R}_5 \end{bmatrix} + \begin{bmatrix} \mathbf{R}_4 & \\ & \mathbf{R}_5 \end{bmatrix} \begin{bmatrix} \mathbf{0}_n & -\mathbf{E}_n \\ \mathbf{0}_n & \mathbf{0}_n \end{bmatrix} - \begin{bmatrix} \beta \mathbf{E}_n \mathbf{R}_4 & \\ & \beta \mathbf{E}_n \mathbf{R}_5 \end{bmatrix} \\ &\quad + \begin{bmatrix} \mathbf{R}_1 & \\ & \mathbf{R}_2 \end{bmatrix} \\ &= \begin{bmatrix} \mathbf{R}_1 - \beta \mathbf{R}_4 & -\mathbf{R}_4 \\ -\mathbf{R}_4 & \mathbf{R}_2 - \beta \mathbf{R}_5 \end{bmatrix} \end{aligned} \quad (4.47)$$

Denote  $\tilde{\Lambda} = \begin{bmatrix} \Lambda & \\ & \Lambda \end{bmatrix}$ , then

$$\widehat{\mathbf{W}} = \tilde{\Lambda} \mathbf{W} \tilde{\Lambda}^T = \begin{bmatrix} \Lambda & \\ & \Lambda \end{bmatrix} \begin{bmatrix} \mathbf{R}_1 - \beta \mathbf{R}_4 & -\mathbf{R}_4 \\ -\mathbf{R}_4 & \mathbf{R}_2 - \beta \mathbf{R}_5 \end{bmatrix} \begin{bmatrix} \Lambda^T & \\ & \Lambda^T \end{bmatrix}$$

$$\begin{aligned}
 &= \begin{bmatrix} \Lambda(\Lambda^T \mathbf{D}_a \Lambda - \beta \Lambda^T \mathbf{D}_c \Lambda) \Lambda^T & -\Lambda \Lambda^T \mathbf{D}_c \Lambda \Lambda^T \\ -\Lambda \Lambda^T \mathbf{D}_c \Lambda \Lambda^T & \Lambda(\Lambda^T \mathbf{D}_b \Lambda - \beta \Lambda^T \mathbf{D}_e \Lambda) \Lambda^T \end{bmatrix} \\
 &= \begin{bmatrix} \mathbf{D}_b - \beta \mathbf{D}_c & -\mathbf{D}_c \\ -\mathbf{D}_c & \mathbf{D}_b - \beta \mathbf{D}_e \end{bmatrix}
 \end{aligned} \tag{4.48}$$

According to Eq. (4.47), the eigenvalues of matrix  $\widetilde{\mathbf{W}}$  and  $\mathbf{W}$  are identical. Let  $\check{\mathbf{z}}_\beta = (x_{1,\beta}, y_{1,\beta}, x_{2,\beta}, y_{2,\beta}, \dots, x_{n,\beta}, y_{n,\beta})^T$ ;  $\check{\mathbf{z}}_\beta$  is a vector of variables obtained by changing the order of variables in  $\mathbf{z}_\beta$ . Then,

$$(\mathbf{z}_\beta)^T \widetilde{\mathbf{W}} \cdot \mathbf{z}_\beta = (\check{\mathbf{z}}_\beta)^T \underbrace{\begin{bmatrix} \widetilde{\mathbf{W}}_1 & & & \\ & \widetilde{\mathbf{W}}_2 & & \\ & & \ddots & \\ & & & \widetilde{\mathbf{W}}_n \end{bmatrix}}_{\widetilde{\mathbf{W}}} \cdot \check{\mathbf{z}}_\beta \tag{4.49}$$

where  $\widetilde{\mathbf{W}}$  is a block diagonal matrix defined above, in which  $\widetilde{\mathbf{W}}_i$  ( $\forall i = 1, 2, \dots, n$ ) is

$$\widetilde{\mathbf{W}}_i = \begin{bmatrix} a_i - \beta c_i & -c_i \\ -c_i & b_i - \beta e_i \end{bmatrix} \tag{4.50}$$

Note  $\widetilde{\mathbf{W}}_i$  is a symmetric matrix. It is negative semidefinite if

$$a_i - \beta c_i \leq 0 \tag{4.51a}$$

and

$$(a_i - \beta c_i)(b_i - \beta e_i) - c_i^2 \geq 0 \tag{4.51b}$$

Obviously, inequality (4.51a) holds if  $a_i < \beta c_i$ . According to Eq. (4.51b), we have

$$(a_i - \beta c_i)(b_i - \beta e_i) - c_i^2 = (a_i - \beta c_i)b_i - \beta e_i(a_i - \beta c_i) - c_i^2 \geq 0 \tag{4.52}$$

Note  $a_i < \beta c_i$ , inequality (4.52) implies that

$$b_i \leq \frac{c_i^2 + \beta e_i(a_i - \beta c_i)}{a_i - \beta c_i} \tag{4.53}$$

As  $b_i \geq 0$ , the right-hand side of inequality (4.4.53) holds only if

$$c_i^2 + \beta e_i(a_i - \beta c_i) \leq 0 \tag{4.54}$$

This implies

$$c_i^2 + \beta e_i(a_i - \beta c_i) \leq 0 \tag{4.55}$$

Thereby,

$$e_i \geq \frac{-c_i^2}{\beta(a_i - \beta c_i)} \tag{4.56}$$

The above discussion shows that if inequalities (4.53), (4.56), and  $a_i < \beta c_i$  hold,  $\widetilde{\mathbf{W}}_i$  is a negative semidefinite matrix. Similarly, we can infer that the block diagonal matrix  $\widetilde{\mathbf{W}}$  is negative semidefinite if inequalities (4.46a)-(4.46c) hold. This implies that  $\widetilde{\mathbf{W}}$  is negative semidefinite. Note that matrix  $\widetilde{\mathbf{W}}$  is similar to the symmetric matrix  $\mathbf{W}$ . Thereby,  $\mathbf{W}$  is negative

semidefinite if inequalities (4.46a)-(4.46c) hold. Proposition 4 is proved. ■

It is worth mentioning that Proposition 4 only provides a sufficient condition to ensure the asymptotic stability of the unconstrained idealized MPC strategy. There exist other conditions under which the unconstrained idealized MPC strategy is also asymptotically stable. Further, there may exist multiple equilibrium states for the CAV platoon depending on the speed of the leading vehicle. Proposition 4 only ensures the local stability of the unconstrained idealized MPC strategy.

According to Proposition 4, the method to determine the diagonal positive definite matrices  $\mathbf{D}_a$ ,  $\mathbf{D}_b$ ,  $\mathbf{D}_c$  and  $\mathbf{D}_e$  and the discount parameter  $\beta$  to ensure asymptotic stability of the unconstrained idealized MPC strategy can be summarized as follows. First, set an arbitrary positive value for  $\beta$  and a diagonal positive definite matrix  $\mathbf{D}_c$ . Second, obtain the matrix  $\mathbf{D}_a$  such that inequality (4.56a) is satisfied. Then, obtain matrices  $\mathbf{D}_e$  and  $\mathbf{D}_b$  according to inequalities (4.56b) and (4.56c), respectively.

## 4.6 Numerical experiments

This section discusses four numerical experiments to demonstrate the motivation for this study and to illustrate the effectiveness of the proposed DMPC-FOA approach. The first numerical experiment analyzes the computational time required for the leading vehicle to solve the optimal control problem (4.5) for different initial inputs, prediction horizons, and the number of following vehicles. The second numerical experiment illustrates the detailed steps for sensitivity analysis of the optimal control problem. The first-order Taylor approximation method is then applied to estimate the solution of state variables, costate variables, and the optimal control decisions when the leading vehicle's initial speed and position are changed. The estimated solution and the exact solution (computed using the solution algorithm in Section 4.3) are compared. The third numerical experiment compares the control performance of the DMPC-FOA approach with that of the DMPC approach assuming the movement of the leading vehicle is predetermined according to NGSIM field data. The fourth numerical experiment shows a traffic flow scenario where the DMPC approach fails to control the CAV platoon safely due to poor estimation of the optimal control decisions of the idealized MPC strategy. However, the DMPC-FOA approach can control the CAV platoon effectively and is able to characterize the optimal control decisions of the idealized MPC strategy accurately in this scenario. The last numerical experiment applies two more scenarios to test the performance of the proposed DMPC-FOA approach.

### 4.6.1 Computational time for solving optimal control problem (4.5)

The DMPC approach and DMPC-FOA approach need to reserve  $\tau_1$  and  $\tau_2$  time before each time instant, respectively, to estimate the optimal control decisions of the idealized MPC approach.  $\tau_1$  should be large enough such that the optimal control problem (4.5) (i.e., the two-point boundary value problem (4.32)) can be solved using the shooting method, while  $\tau_2$  should be sufficiently large so as to solve the two-point boundary value problems (32), (35) and (37) with the shooting method. Note that the computational times for the two-point boundary value problems significantly depend on the platoon size ( $n$ ), the prediction horizon ( $T_p$ ) and the initial state of the CAV platoon. In this study, the values of  $\tau_1$  and  $\tau_2$  will be determined offline according to platoon size and the prediction horizon. For each platoon size (varying from 2 to 15) and the prediction horizon (varying from 1 second to 8 seconds), we

randomly generated 1000 initial states of the CAV platoon. The shooting method is applied to solve the two-point boundary value problems (32), (35) and (37) under each initial state. The computational time for solving the two-point boundary value problems (32) corresponding to 0.95 cumulative probability is used as the baseline for  $\tau_1$ , while the total computational time for solving the two-point boundary value problems (32), (35) and (37) corresponding to 0.95 cumulative probability is used as the baseline for  $\tau_2$ .

Table 4.1 shows the detailed inputs of the parameters in the optimal control problem (4.5). These inputs are used for all four numerical experiments. The discount parameter  $\beta$  and the matrices  $\mathbf{R}_1$ ,  $\mathbf{R}_2$ ,  $\mathbf{R}_4$ , and  $\mathbf{R}_5$  in optimal control problem (4.5) are set as follows:  $\beta = 1$ ,  $\mathbf{R}_1 = 0.5\mathbf{E}_n$ ,  $\mathbf{R}_2 = \mathbf{R}_4 = \mathbf{E}_n$ ,  $\mathbf{R}_5 = 3\mathbf{E}_n$ . These inputs satisfy the inequalities in Proposition 4 to ensure that the unconstrained idealized MPC strategy is asymptotic stable. It is worth mentioning that the value of  $\beta$  decides the weights of the running cost at different time in future. It not only impacts the stability of the benchmark MPC approach, but also the estimation performance of the DMPC-FOA approach. Our analysis shows that the stability performance of the benchmark MPC approach and the estimation performance of the DMPC-FOA are better when  $\beta \in [0.5, 1.5]$ .

Table 4.1. Input parameters for optimal control problem (4.5)

Variables	Default value
Minimum acceleration ( $u_{min}$ )	$-5 \text{ m/s}^2$
Maximum acceleration ( $u_{max}$ )	$3 \text{ m/s}^2$
Minimum spacing ( $s_{min}$ )	$5 \text{ m}$
Safety space ( $s_f$ )	$10 \text{ m}$
Speed limit ( $v_{max}$ )	$33.5 \text{ m/s (120 km/h)}$
Time headway ( $r^*$ )	$1 \text{ s}$

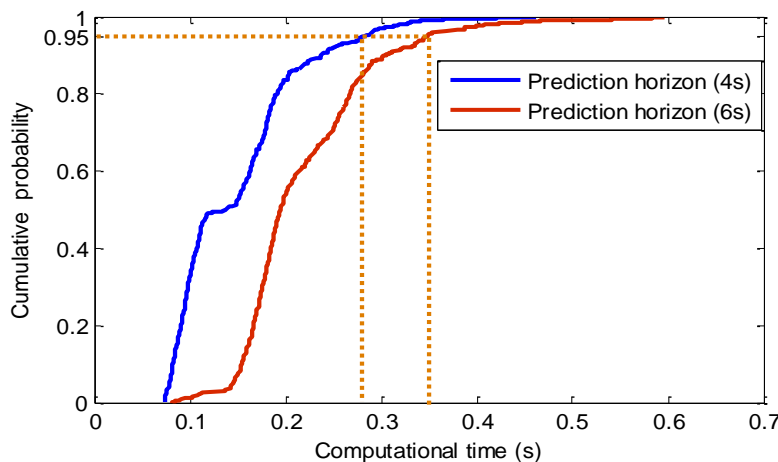


Figure 4.5. Cumulative probability of computational time for solving optimal control problem (4.5) with different initial inputs (i.e.,  $\mathbf{x}(0)$  and  $\mathbf{y}(0)$ ) at  $n = 8$  and  $T_p = 4\text{s}$  and  $6\text{s}$ .

Without loss of generality, suppose the initial time is 0. To ensure that optimal control problem (4.5) can be solved within  $\tau_1$  seconds under different initial inputs of position errors (i.e.,  $\mathbf{x}(0)$ ) and speed differences (i.e.,  $\mathbf{y}(0)$ ) of all adjacent vehicles pairs,  $\mathbf{x}(0)$  is generated randomly in the interval  $[-10,100]$  and  $\mathbf{y}(0)$  is randomly generated in the interval  $[0,20]$ . This study generates 1000 different values for  $\mathbf{x}(0)$  and  $\mathbf{y}(0)$  for which the inequality constraints (Eq. (4.4.5c)) are satisfied.

The numerical experiments were coded in MATLAB and executed on a computer with an Intel Core i7-4790 3.60-GHz CPU with 8.00 GB of RAM. To analyze the impacts of the number of following vehicles in the platoon ( $n$ ) and the prediction horizon ( $T_p$ ) on computational time, optimal control problem (4.5) is solved 1000 times under different feasible initial inputs for each combination of  $n$  and  $T_p$ .

Fig. 4.5 shows the cumulative probability of computational time for solving the optimal control problem (4.5) with different initial inputs (i.e.,  $\mathbf{x}(0)$  and  $\mathbf{y}(0)$ ) for  $n = 8$  and  $T_p = 4s$  and  $6s$ . It shows that the computational time significantly depends on the value of  $\mathbf{x}(0)$  and  $\mathbf{y}(0)$ . The computational time ranges from 0.08s to 0.4s under  $n = 8$  and  $T_p = 4s$ . It is worth noting that computational times are large only when the initial position errors of many adjacent vehicle pairs deviate remarkably from the equilibrium state (i.e., they are close to 100 m), the likelihood of occurrence of which is low in the real world. Hence, this study uses the computational time corresponding to 0.95 cumulative probability as the reference point to determine the reserved time for the DMPC and DMPC-FOA approaches.

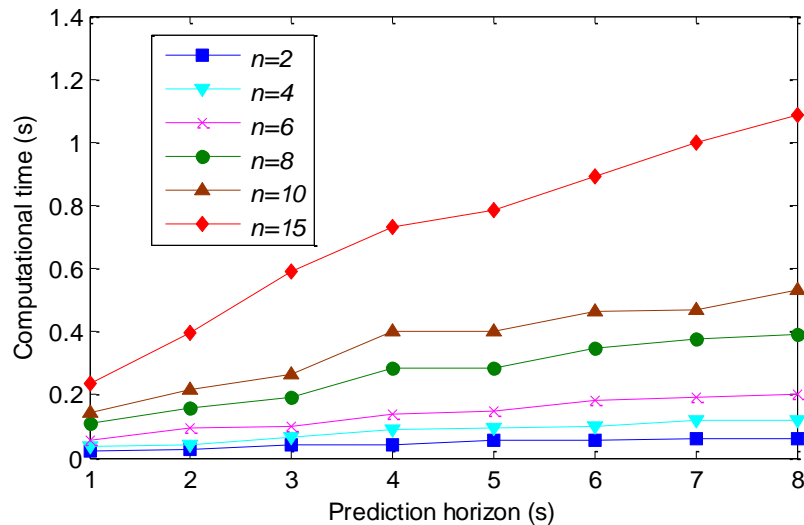


Figure 4.6. Computational time corresponding to 0.95 cumulative probability under different  $n$  and  $T_p$ .

Fig. 4.6 shows the computational time corresponding to 0.95 cumulative probability under different  $n$  and  $T_p$ . The computational time corresponding to 0.95 cumulative probability is the time within which 95% of the experimental scenarios can be solved. Fig. 4.6 illustrates that the computational time corresponding to 0.95 cumulative probability increases monotonically with the number of following vehicles and the prediction horizon.

#### 4.6.2 Sensitivity analysis of optimal control problem (4.5)

Figure 4.7 presents the solutions of costate variables and optimal control decisions at the unperturbed initial state: (a) solutions of costate variables; (b) optimal control decisions.

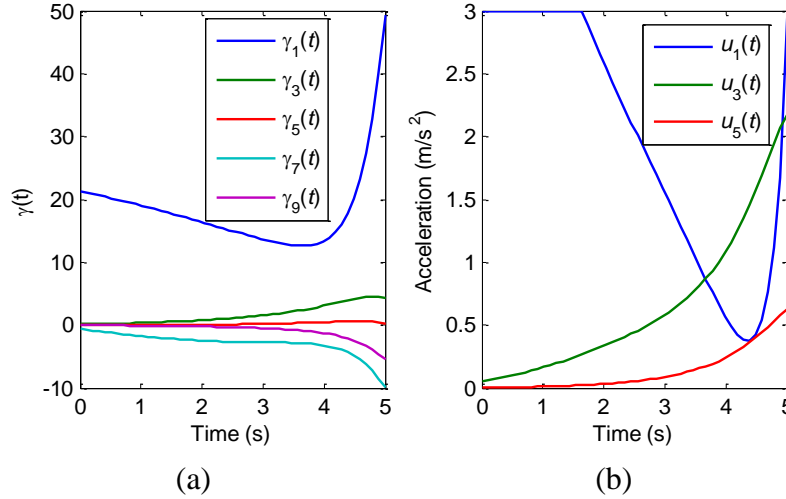


Figure 4.7. Solutions of costate variables and optimal control decisions at the unperturbed initial state: (a) solutions of costate variables; (b) optimal control decisions.

This section shows the details of the sensitivity analysis method implementation for the optimal control problem (4.5) introduced in section 4.4. Consider a CAV platoon with 5 following vehicles ( $n = 5$ ). The leading vehicle and all following vehicles drive at a speed of 20 m/s at time 0 (i.e.,  $\mathbf{y}(0) = 0$ ). Suppose the initial position errors of vehicle 2 to vehicle 5 are all 0, and the initial position error of vehicle 1 with respect to the leading vehicle is 90 m. This implies that the spacing between vehicle 1 and vehicle 0 is  $90 + T \cdot 20 + s_f = 120m$ . It indicates a case where the following vehicles seek to catch up with the leading vehicle. Let  $T_p = 5$  s. Fig. 4.7(a) shows the optimal solutions of the costate variables obtained using the solution algorithm proposed in Section 4.3. The optimal control decisions of all following vehicles in the platoon can then be determined according to Eq. (4.23). Fig. 4.7(b) shows the optimal control decisions of vehicles 1, 3 and 5. It indicates that vehicle 1 accelerates at the maximum value ( $3 m/s^2$ ) for the first 1.7 seconds. Then, the acceleration decreases monotonically in the time interval [1.7s, 4.3s] and then increases.

Suppose the initial position and speed of the leading vehicle at time 0 are perturbed. Then,  $x_1(0)$  and  $y_1(0)$  change from the unperturbed values 90 and 0, respectively. Fig. 4.8 shows the derivatives of solutions for the state and costate variables with respect to  $x_1(0)$  and  $y_1(0)$ , respectively. They are obtained by solving the two-point boundary value problem (4.35) and (37), respectively. Fig. 4.8 shows that at the optimal state, a unit change in  $x_1(0)$  and  $y_1(0)$  will increase the optimal solution of  $x_1(t)$  and  $y_1(t)$  by 1, respectively, at time interval [0,1.7]. The impacts of variations in  $x_1(0)$  and  $y_1(0)$  on  $x_1(t)$  and  $y_1(t)$  decrease after 1.7 seconds.

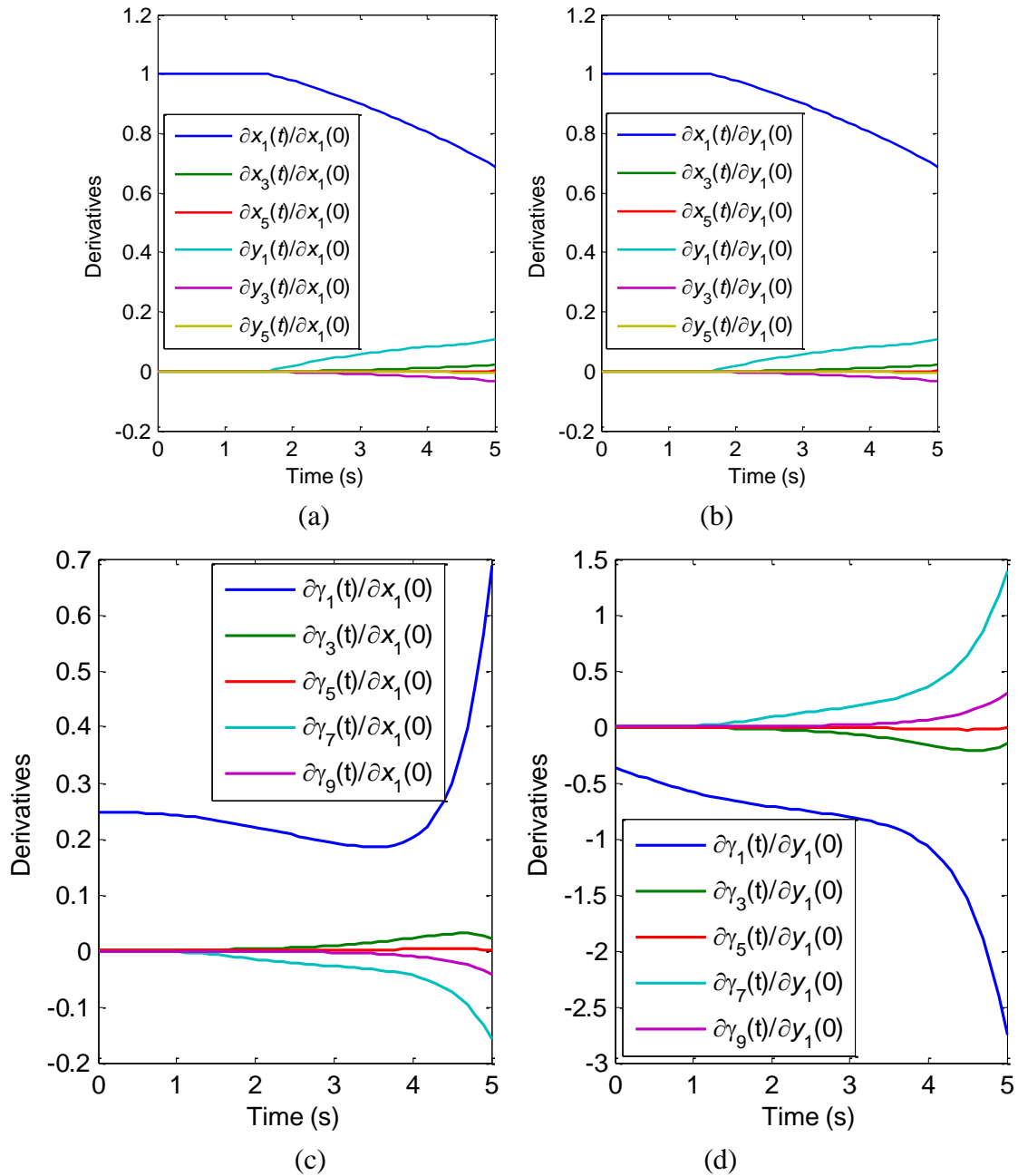


Figure 4.8. Derivatives of the state and costate variables with respect to  $x_1(0)$  and  $y_1(0)$ , respectively, at the unperturbed initial state: (a) derivatives of the state variables with respect to  $x_1(0)$ ; (b) derivatives of the state variables with respect to  $y_1(0)$ ; (c) derivatives of the costate variables with respect to  $x_1(0)$ ; (d) derivatives of the costate variables with respect to  $y_1(0)$ .

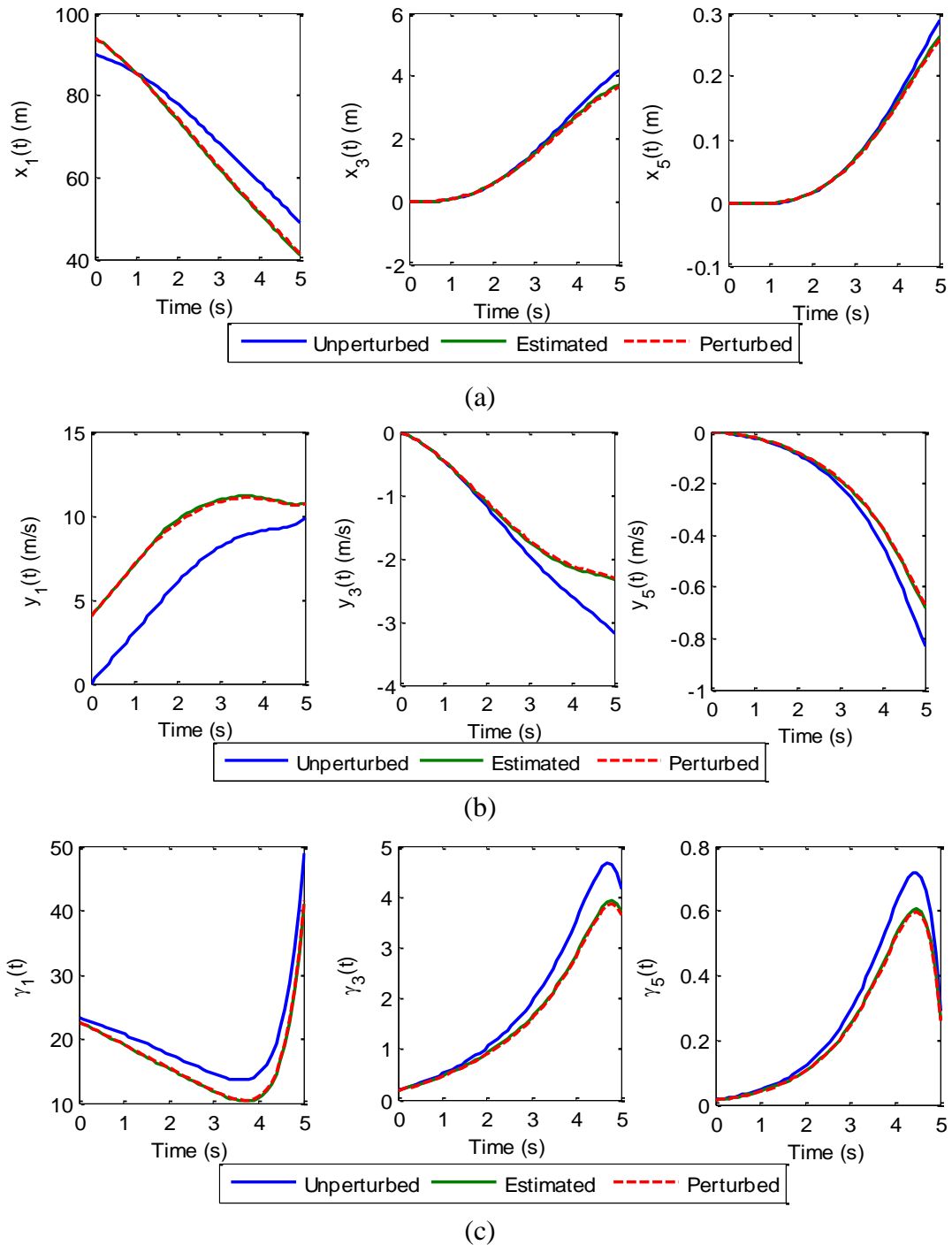


Figure 4.9. Comparison of estimated and perturbed optimal solutions for the state and costate variables: (a) comparison of estimated and perturbed optimal solutions of position errors; (b) comparison of estimated and perturbed optimal solutions of speed difference for adjacent vehicle pairs; (c) comparison of estimated and perturbed optimal solutions for the costate variables.

Suppose both  $x_1(0)$  and  $y_1(0)$  are increased by 4 units (for example, due to prediction error). Using the first-order Taylor approximation (Eq. (4.4.38)), Fig. 4.9 compares the estimated and perturbed optimal solutions for the state variables and costate variables. The perturbed solutions are obtained using the solution algorithm at the perturbed states of  $x_1(0)$  and  $y_1(0)$ . Fig. 4.9 shows that the estimated solutions are very close to those of the perturbed solutions, indicating that the first-order Taylor approximation can accurately characterize the variation in the optimal solutions induced by changes in  $x_1(0)$  and  $y_1(0)$ . Based on the estimated solutions for the costate variables (i.e.,  $\boldsymbol{\gamma}$ ), Fig. 4.10 compares the optimal control decisions of following vehicles estimated by Eq. (4.4.39) and the perturbed ones obtained using the solution algorithm in Section 4.3. It shows that the estimated solutions are also very close to the perturbed ones obtained using the solution algorithm.

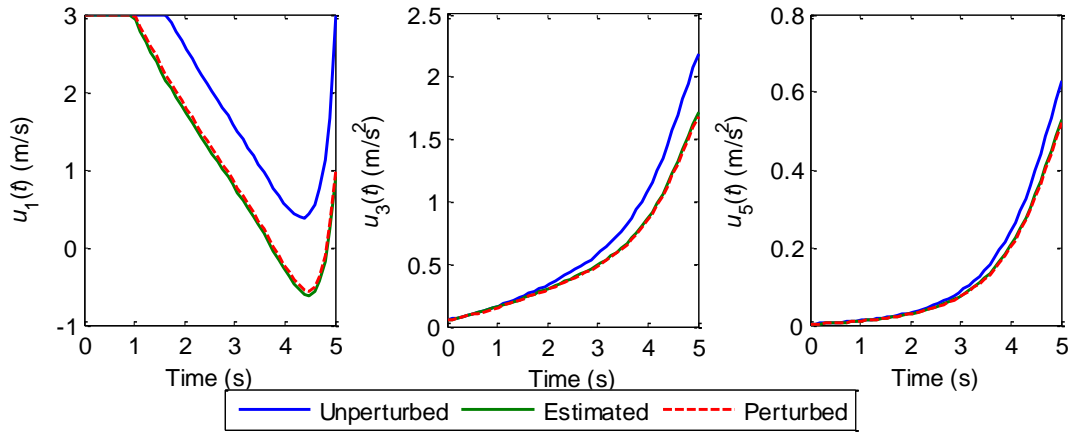


Figure 4.10. Comparison of estimated and perturbed optimal control decisions of the following vehicles.

#### 4.6.3 Control performance of the DMPC and DMPC-FOA approaches

Figure 4.11 presents the acceleration of the leading vehicle.

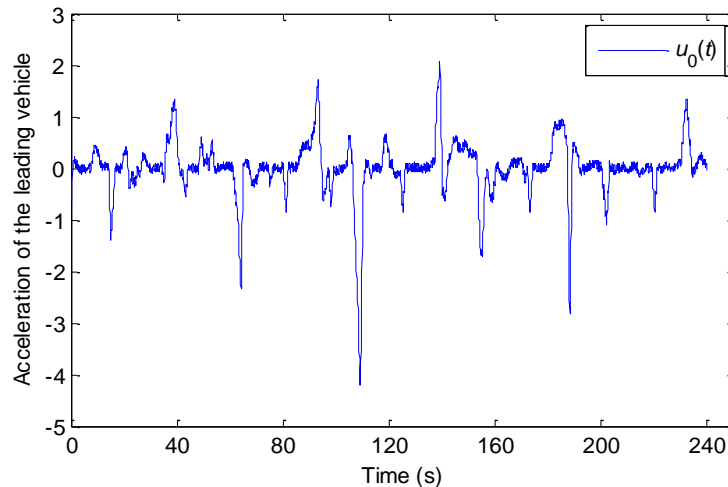


Figure 4.11. Acceleration of the leading vehicle

Note that both the DMPC and DMPC-FOA approaches seek to address the issue of control delay and estimate the optimal control decisions of the idealized MPC strategy. This section compares the control decisions of the DMPC approach, the DMPC-FOA approach and the idealized MPC strategy. To do so, we consider a CAV platoon with 8 following vehicles (vehicle IDs 1-8). The acceleration of the leading vehicle is shown in Fig. 4.11. It contains a 240-seconds (with resolution 0.1 second) real-world vehicle control diary collected on eastbound I-80 in the San Francisco Bay area at Emeryville, California. It can be noted that the vehicle decelerated or accelerated mildly most of the time. However, it contains some time slots with hard braking and high acceleration (e.g., the time slots around 110s, 140s and 186s). Suppose the prediction horizon and the roll period are  $T_p = 5$  seconds and  $\Delta t = 1$  second, respectively. According to Fig. 4.6, the computational time for solving optimal control problem (4.5) corresponding to 95% cumulative probability with 8 following vehicles is 0.33 seconds. To reserve enough time for solving the optimal control problem,  $\tau_1$  is set as 0.4 seconds for the DMPC approach. Note that the DMPC-FOA approach needs to solve optimal control problem (4.5) as well as perform sensitivity analysis of the optimal control problem with respect to  $\tilde{x}_1(0)$  and  $\tilde{y}_1(0)$ . Thereby,  $\tau_2 \geq \tau_1$ . From 1000 simulations, the total computational time for solving the optimal control problem (4.5) and the two-point boundary value problems (problems (35) and (37)) corresponding to 95% cumulative probability is around 0.56 seconds. Thereby,  $\tau_2$  is set as 0.6 seconds. It should be noted that among the 1000 simulations, there are situations where some following vehicles need to brake and accelerate at the maximum rate during the prediction horizon. Thereby,  $\tau_2 = 0.6s > \tau_1 = 0.4s$ . According to Proposition 3, if these situations do not exist and the spacing of each following vehicle is always greater than the minimum value ( $s_{min}$ ),  $\tau_2$  can be set the same as  $\tau_1$ .

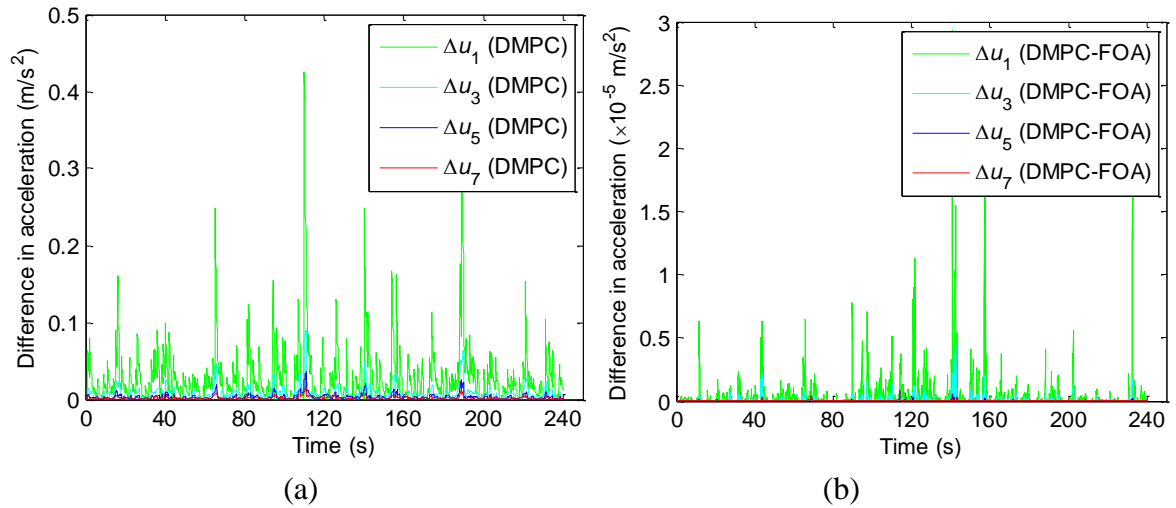


Figure 4.12. Differences between the estimated control decisions of the DMPC and DMPC-FOA approaches from those of the idealized MPC strategy: (a) difference between control decisions of the DMPC approach and those of the idealized MPC strategy; (b) difference between control decisions of the DMPC-FOA approach and those of the idealized MPC strategy.

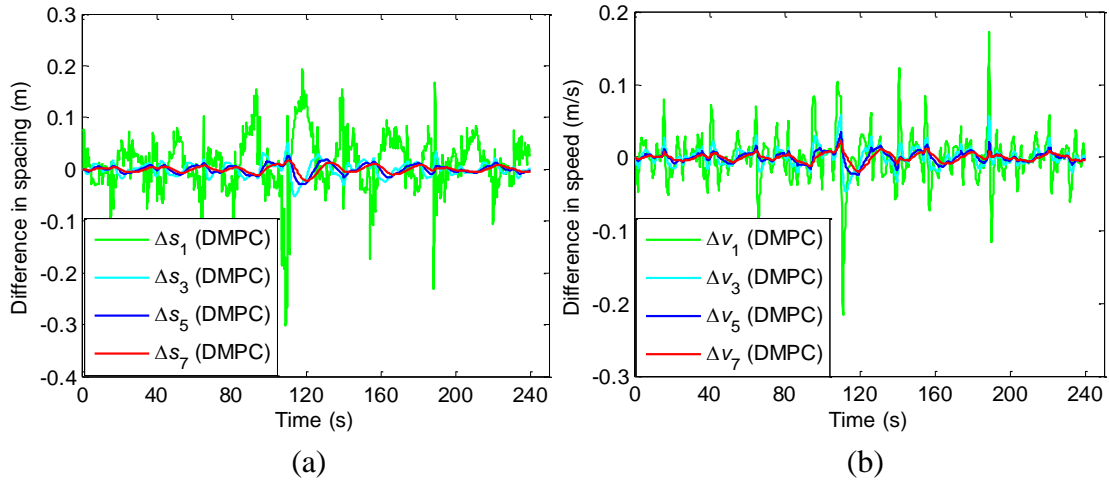


Figure 4.13. Differences in optimal spacing and speed between the DMPC approach and the idealized MPC strategy: (a) difference in optimal spacing; (b) difference in optimal speed.

Fig. 4.12 shows the difference between the estimated control decisions of the DMPC approach (i.e.,  $\Delta u_i = \hat{u}_i^*(t) - u_i^*(t), \forall i = 1, 2, \dots, n$ ) and the DMPC-FOA approach (i.e.,  $\Delta u_i = \bar{u}_i^*(t) - u_i^*(t), \forall i = 1, 2, \dots, n$ ) from those of the idealized MPC strategy. Fig. 4.12(a) shows that the estimated control decisions of the DMPC approach are close to those of the idealized MPC strategy with the maximum difference less than  $0.45 \text{ m/s}^2$ . The estimation errors of the control decisions of DMPC approach are induced by the prediction error of  $x_1(t)$  and  $y_1(t)$  at each sampling time instant. However, through first-order Taylor's approximation, the DMPC-FOA approach can significantly improve on the estimation performance of the DMPC approach. As can be seen from Fig. 4.12(b), the maximum difference between the control decisions estimated by the DMPC-FOA approach and the idealized MPC strategy is less than  $3 \times 10^{-5} \text{ m/s}^2$ , indicating that the DMPC-FOA approach can characterize the decisions of the idealized MPC strategy very well.

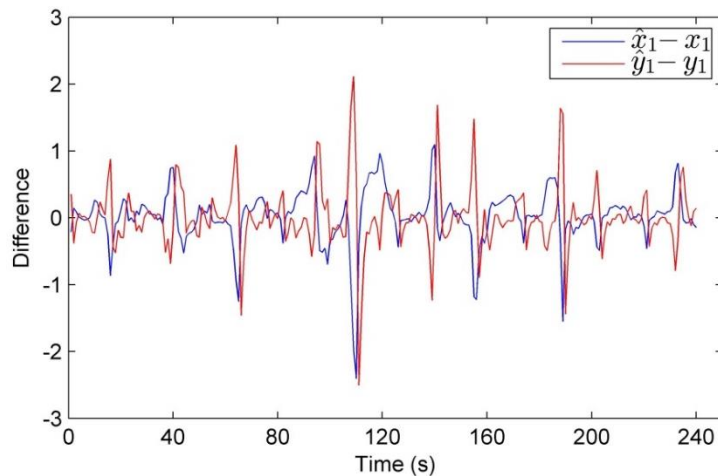


Figure 4.14. Prediction errors of the initial states of  $x_1(t_k)$  and  $y_1(t_k)$ ,  $t_k = 1s, 2s, \dots, 240s$ .

Fig. 4.13 illustrates the differences in optimal spacing and speed between the DMPC approach and the idealized MPC (i. e.,  $\Delta s_i$  and  $\Delta v_i$ , respectively,  $i = 1, 2, \dots, n$ ). It shows that while the estimated control decisions of DMPC approach deviate from the idealized MPC strategy, the optimal spacing and speed obtained by the DMPC approach are very close to those of the idealized MPC strategy. Hence, the DMPC approach is able to control the CAV platoon efficiently in this case. To investigate the reason for the good control performance of the DMPC approach in this scenario, Fig. 4.14 shows the prediction errors of the initial inputs of  $x_1(t)$  and  $y_1(t)$  at each sampling time instant  $t_k, k = 1, 2, \dots$ . Recall  $\Delta t = 1s$ . Hence,  $t_k = 1s, 2s, \dots, 240s$ . It shows that the predicted values of  $x_1(t_k)$  and  $y_1(t_k), k = 1, 2, \dots$  are very close to those of the exact ones as the leading vehicle drives with mild acceleration or deceleration most of the time (see Fig. 4.11). The large prediction error occurs at the moments when the leading vehicle has hard acceleration or deceleration (e.g.,  $t = 110s, 140s, 186s$  etc.). Correspondingly, the DMPC approach also has larger estimation errors in terms of the optimal solutions relative to those of the idealized MPC strategy (see Fig. 4.12(a) and Fig. 4.13). However, as these “extreme” behaviors of the leading vehicle only last for small time periods, their impacts are small. In addition, if  $x_1(t_k)$  and  $y_1(t_k)$  are accurately predicted at a time instant  $t_k$ , the large difference in optimal solutions between the DMPC approach and the idealized MPC strategy in the previous roll period will be reduced significantly at the current roll period starting from time instant  $t_k$ . This can be observed in Fig. 4.12(a) and Fig. 4.13 where the large differences at time instants  $t = 110s, 140s, 186s$  are reduced dramatically in the roll periods following time instants at which  $x_1(t)$  and  $y_1(t)$  are predicted with low errors at the corresponding sampling time instants (i.e.,  $t_k = 111s, 141s, 187s$ , see Fig. 4.14).

Fig. 4.15 shows the control decisions of the following vehicles estimated by the DMPC-FOA approach. It indicates that when the leading vehicle 0 executes hard acceleration/deceleration, vehicle 1 also executes hard acceleration/deceleration with a magnitude slightly less than that of the leading vehicle 0. The acceleration or deceleration decreases sequentially in the platoon, indicating that the traffic oscillation is damped sequentially from the head of the platoon to its tail. Fig. 4.16 shows the optimal spacing and speed differences of adjacent vehicle pairs in the platoon computed by the DMPC-FOA approach. These results are almost identical to those of the idealized MPC strategy with the maximum absolute error less than  $8 \times 10^{-8}$  due to the high accuracy of the estimated optimal control decisions (see Fig. 4.12(b)). As can be seen in Fig. 4.16, the oscillation of the optimal spacing and speed difference of adjacent vehicle pairs decreases sequentially in the platoon. These results indicate that the DMPC-FOA approach can lead to smooth deceleration and acceleration behavior of all following vehicles. In addition, it can coordinate the behavior of all following vehicles to dissipate the traffic oscillation to ensure stability of the CAV platoon.

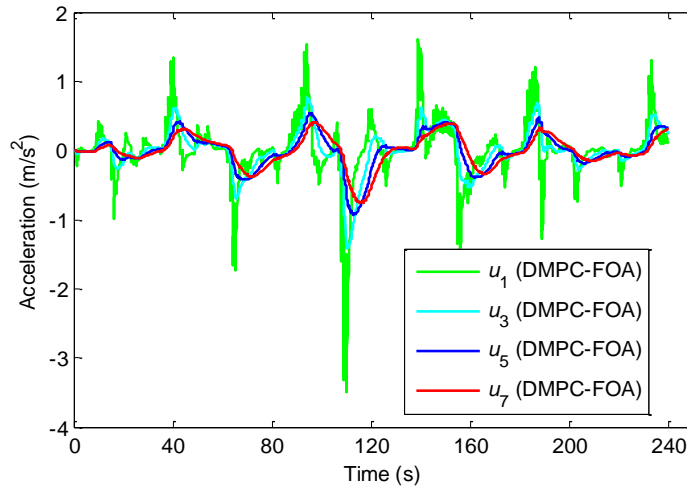


Figure 4.15. Estimated control decisions of the DMPC-FOA approach.

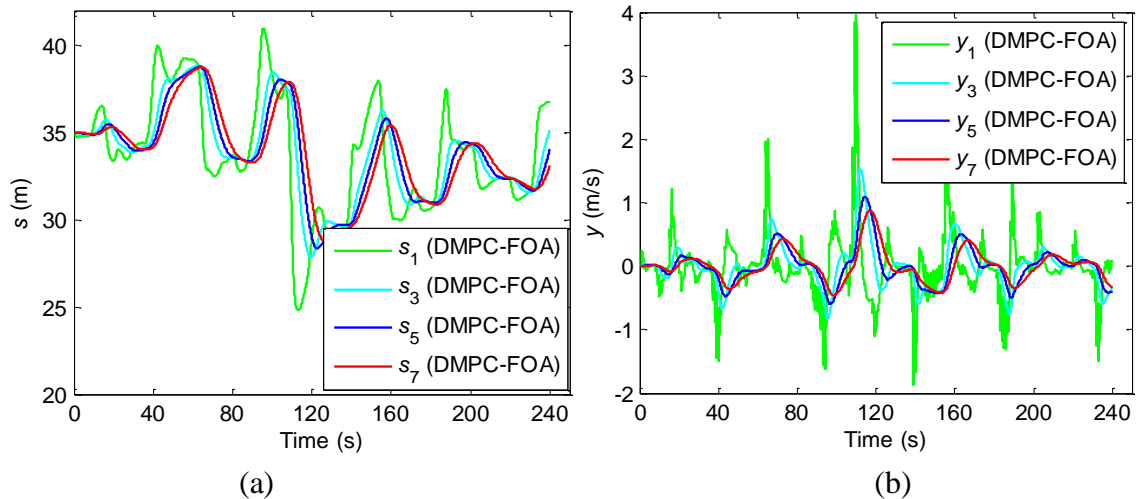


Figure 4.16. Optimal spacing and speed difference for some adjacent vehicle pairs in the platoon computed by DMPC-FOA approach: (a) spacing of adjacent vehicle pairs; (b) speed difference of adjacent vehicle pairs.

#### 4.6.4 Scenario where the DMPC approach fails to control the CAV platoon

The previous section illustrated a scenario in which the estimated control decisions and the solutions for the state variables of the DMPC approach are very close to those of the idealized MPC strategy. Here, we illustrate a scenario in which when the DMPC approach fails to accurately predict the values of  $x_1(t_k)$  and  $y_1(t_k)$  at each sampling time instant  $t_k$ , the error of the control decisions between the DMPC approach and idealized MPC strategy increases with each roll period. Then, the car-following behavior of the vehicles controlled by the DMPC approach significantly deviates from that of the idealized MPC strategy. However, as will be illustrated, the DMPC-FOA approach accurately characterizes the optimal control decisions of the idealized MPC strategy.

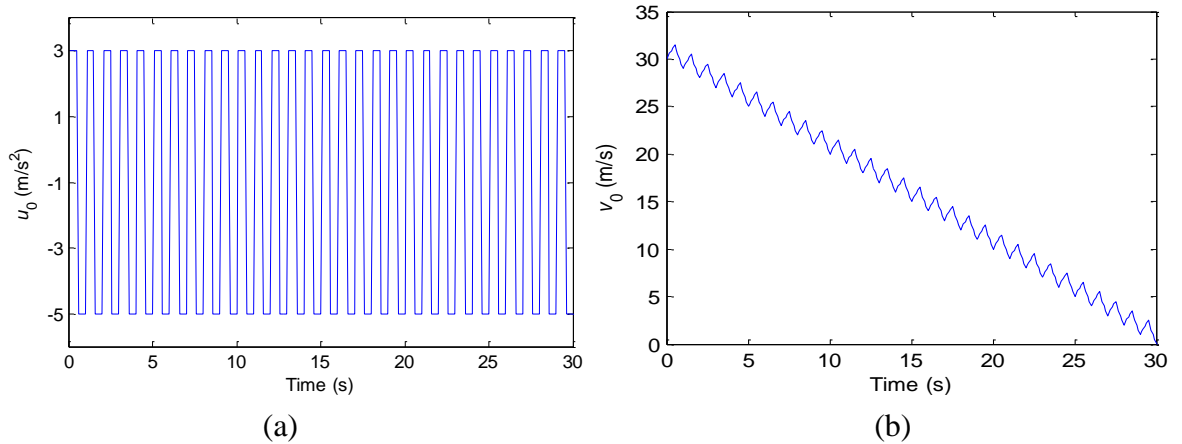


Figure 4.17. Acceleration and speed of the leading vehicle: (a) acceleration of the leading vehicle; (b) speed of the leading vehicle.

Consider a CAV platoon with 10 following vehicles. Let  $T_p = 5$  seconds and  $\Delta t = 1$  second. According to Fig. 4.6, the computational time corresponding to 95% cumulative probability is 0.42 seconds. Hence, we set  $\tau_1 = 0.5$  seconds for the DMPC approach. By conducting 1000 simulation runs with different initial inputs for  $x_1(0)$  and  $y_1(0)$ , the computational time corresponding to 95% cumulative probability for the DMPC-FOA approach is determined as 0.66 seconds. We will set  $\tau_2 = 0.7$  seconds for the DMPC-FOA approach.

Suppose the leading vehicle drives at  $30 \text{ m/s}$  at time 0. Assume the leading vehicle accelerates at the maximum value  $3 \text{ m/s}^2$  for 0.5 seconds and then decelerates at the maximum value  $-5 \text{ m/s}^2$  for 0.5 seconds. Such behavior will repeat for 30 seconds until the leading vehicle stops. Fig. 4.17(a) shows the trajectory of the assumed acceleration of the leading vehicle. The corresponding speed of the leading vehicle is shown in Fig. 4.17(b).

As  $\Delta t = 1$  second, the sampling time instant  $t_k = k$  seconds for  $k = 1, 2, \dots$ . Under the assumed acceleration behavior of the leading vehicle, the prediction errors of  $x_1(t_k)$  and  $y_1(t_k)$  using the DMPC approach are  $-1 \text{ m}$  and  $4 \text{ m/s}$ , respectively, at each sampling time instant  $t_k$ . Note that the prediction errors of  $x_1(t_k)$  and  $y_1(t_k)$  ( $k = 1, 2, 3, \dots$ ) for DMPC-FOA are the same as that of DMPC approach.

Fig. 4.18 compares the optimal solutions for the DMPC approach, the DMPC-FOA approach and the idealized MPC strategy. It illustrates that both spacing and control decisions of vehicle 1 computed using the DMPC approach deviate significantly from those of the idealized MPC strategy due to the large prediction errors of  $x_1(t_k)$  and  $y_1(t_k)$  ( $k = 1, 2, \dots$ ). In addition, the spacing between the leading vehicle 0 and vehicle 1 even reduce to a value less than the minimum allowable spacing  $s_{min}$  ( $s_{min} = 5 \text{ m}$ ). Thereby, a collision will occur between leading vehicle 0 and vehicle 1 in the platoon. Note that the DMPC approach stops at  $t = 18\text{s}$  as the safety constraints (inequality (4.5c)) cannot be satisfied thereafter. Hence, no solution can be found using the DMPC approach. By contrast, the DMPC-FOA approach provides an optimal solution very close to that of the idealized MPC strategy. When the leading vehicle stops at  $t = 30\text{s}$ , the spacing between leading vehicle 0 and vehicle 1 is over  $10 \text{ m}$  to ensure safety. These results highlight that the DMPC-FOA approach can effectively improve the estimation performance significantly beyond that of the DMPC approach even under extreme scenarios.

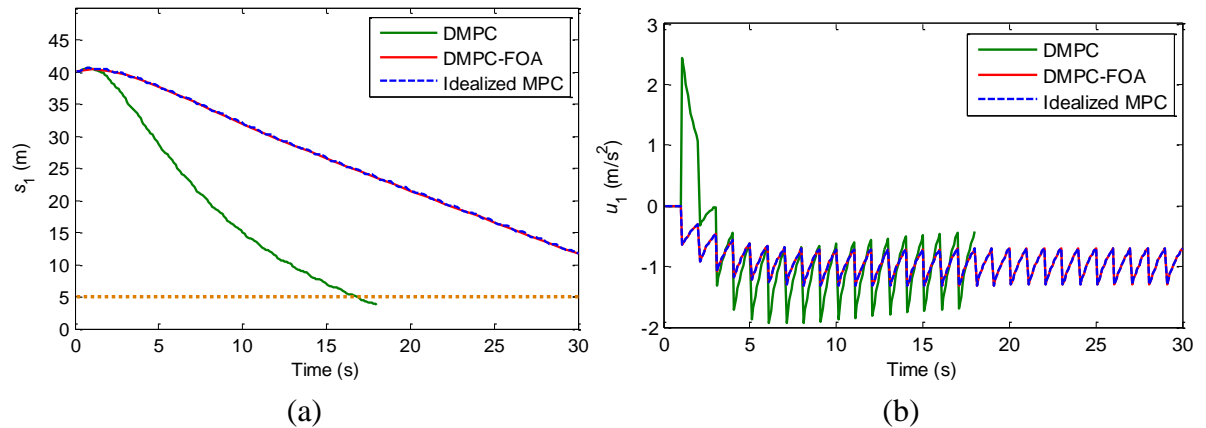


Figure 4.18. Comparison of solutions for spacing and control decisions of vehicle 1 among the DMPC approach, the DMPC-FOA approach and the idealized MPC strategy: (a) comparison of solution for spacing of vehicle 1; (b) comparison of control decisions for vehicle 1

The control performances of the above two scenarios show that when the leading vehicle decelerates or accelerates mildly and less frequently (e.g., when traffic density is low), the DMPC approach is sufficient to control the CAV platoon efficiently. However, when the leading vehicle executes a hard brake or accelerates frequently (e.g., in congested traffic flow), the DMPC-FOA approach should be applied to ensure the safety and efficiency of the CAV platoon.

#### 4.6.5 Two other scenarios to test the control performances of DMPC-FOA approach

In this section, the following two traffic scenarios are considered to validate the performance of the DMPC-FOA approach. Assume that the number of following CAVs in the platoon is 8. Let  $\tau_2 = 0.6$  seconds.

In scenario 1, the leading vehicle performs acceleration and deceleration maneuvers to represent a situation in which the platoon approaches a traffic jam on a highway and moves out of the traffic jam afterwards. In the simulation of 180 seconds, the leading vehicle drives at a constant speed of 25 m/s for 20 seconds. It decelerates at  $-4$  m/s<sup>2</sup> and accelerates at 3 m/s<sup>2</sup> in time [20s, 23s] and [110s, 114s], respectively.

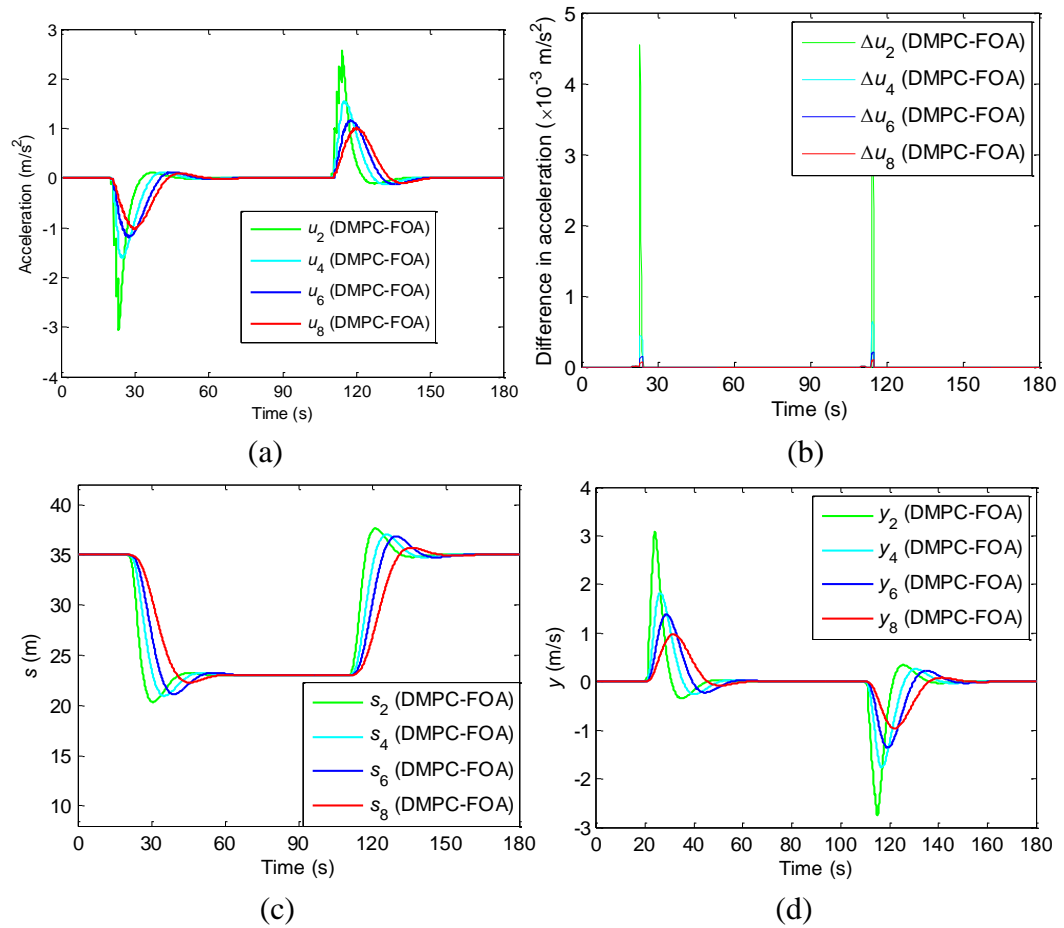


Figure 4.19. Optimal results computed by DMPC-FOA approach for scenario 1: (a) Control decision; (b) Difference in optimal control decisions between the DMPC approach and the idealized MPC strategy; (c) spacing of adjacent vehicle pairs; (d) difference in speed of adjacent vehicle pairs

In scenario 2, suppose the platoon approaches a signalized intersection. The leading vehicle drives at a constant speed of  $30 m/s$  initially and decelerates at  $-2 m/s^2$  at  $t = 10s$  until it stops completely. Fig. 4.19 shows the optimal results of the DMPC-FOA approach for scenario 1. As can be seen, the magnitudes of deceleration and acceleration decrease from the head of the platoon to its tail, implying that the scale of perturbation decreases sequentially in the platoon (Fig. 4.19(a)). Fig. 4.19(b) shows that the maximum error of the estimated optimal control is less than  $5 \times 10^{-3} m/s^2$ , indicating that the DMPC-FOA approach can accurately characterize the optimal control of the idealized MPC approach. Fig. 4.19(c) and Fig. 4.19(d) illustrate the evolution of space headway and speed difference of adjacent vehicle pairs, respectively. These results further validate that the DMPC-FOA approach can damp traffic oscillations effectively.

For scenario 2, similarly, the DMPC-FOA approach can accurately estimate the optimal control decisions of the idealized MPC approach (see Fig. 4.20(a)). The following vehicles decelerate when the leading vehicle decelerates and converge to the equilibrium state sequentially (see Fig. 4.19(b)). The evolution of space headway and speed difference of adjacent vehicle pairs show that the traffic oscillation decays in the platoon (Figures 4.20(c)

and 4.20 (d)). ”

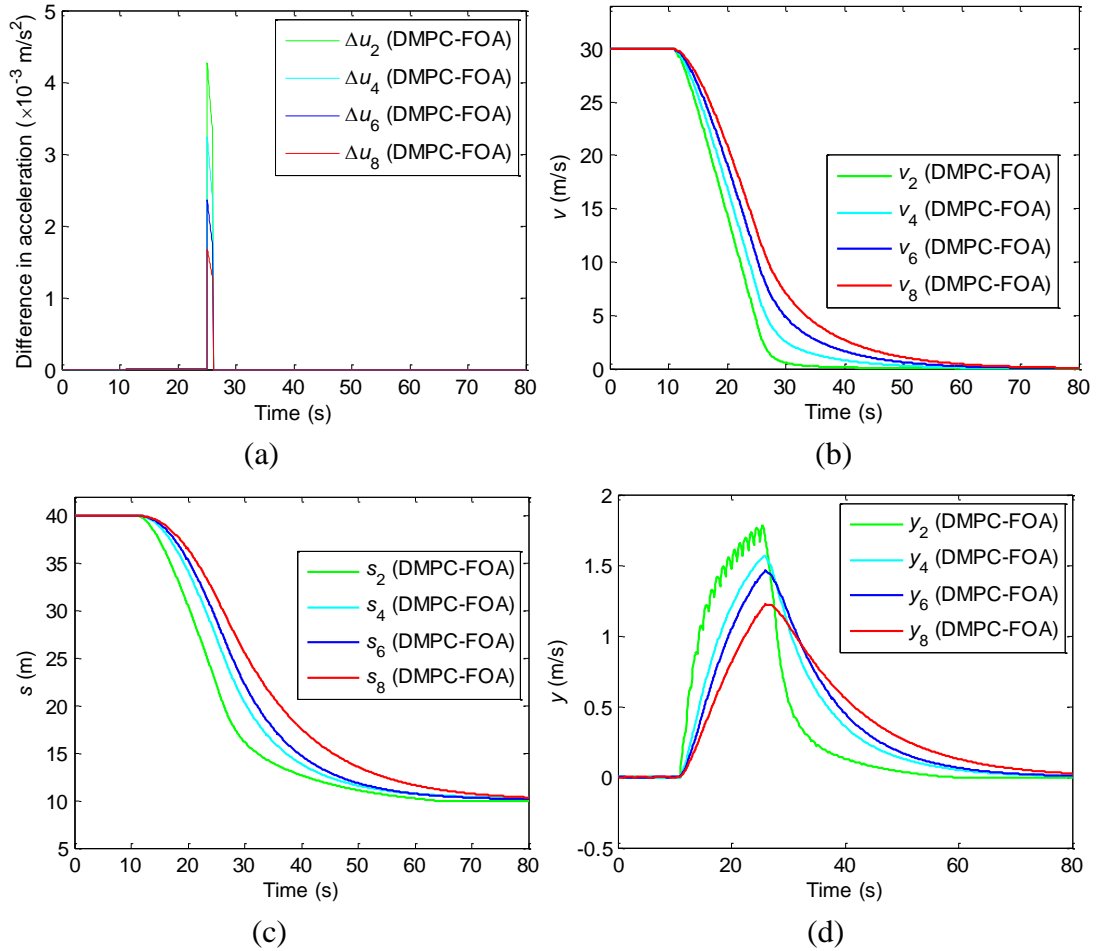


Figure 4.20. Optimal results computed by DMPC-FOA approach for scenario 2: (a) Difference in optimal control decisions between the DMPC approach and the idealized MPC strategy; (2) speed of each vehicle; (c) spacing of adjacent vehicle pairs; (d) difference of speed of adjacent vehicle pairs.

## 5. FINDINGS AND CONCLUSIONS

This study investigated the cooperative control mechanism for CAV platoon factoring communication and computational issues.

The proposed novel CACC strategy in section 2, namely CACC-OIFT, explicitly factors IFT dynamics and leverages it to enhance the platoon performance in an unreliable V2V communication context for a pure CAV platoon. The proposed CACC-OIFT consists of an adaptive PD controller and an IFT optimization model. Given the adaptive PD controller with a two-predecessor-following scheme, and the ambient traffic conditions and the platoon size just before the start of a time period, the IFT optimization model determines the optimal IFT that dynamically activates and deactivates the “send” functionality of the V2V communication devices of all vehicles in platoon, which maximizes the expected string stability. Since communication failures can cause IFT to degenerate dynamically, all possible degeneration scenarios for that IFT are considered in this expectation. The degeneration scenario probabilities are determined based on the communication failure probabilities for that time period which depend on the ambient traffic conditions. In the operational deployment context, based on the various degeneration scenarios for the optimal IFT at different time instants within the time period, the adaptive PD controller continuously determines the car-following behaviors of the vehicles in the platoon. A two-step algorithm is proposed to solve the IFT optimization problem by leveraging some key proven properties, such as the leading vehicle in the platoon should always activate its “send” functionality. Extensive numerical simulations are conducted in NS-3 to illustrate the effectiveness of CACC-OIFT.

To the best of our knowledge, section 2 is the first attempt to explicitly factor IFT dynamics and to leverage it to enhance the performance of CACC strategies. Further, it is the first study to perform a rigorous mathematical modeling of the problem to theoretically illustrate properties. The insights from numerical experiments suggest that CACC-OIFT can leverage IFT dynamics to proactively reduce V2V communication failures while ensuring realism in terms of factoring the ambient traffic conditions. Further, the proposed two-step algorithm and its ability to be parallelized ensure computational tractability for operational deployment for platoons of considerable size (15 vehicles in this study). Also, the study insights provide key pointers for future CACC designs, in that communication failures and IFT dynamics should be considered to enable realism and enhance control performance. In summary, CACC-OIFT can generate a more reliable IFT for a CAV platoon, damp traffic oscillation propagation, and stabilize the traffic flow more efficiently for the entire platoon. Thereby, CACC-OIFT is string stable and outperforms strategies proposed in the current literature, CACC-DIFT and CACC-FIFT, considerably.

To further enhance the riding comfort and string stability, section 3 introduces the CACC-SOIFT framework for CAV platoons in the dynamic IFT environment arising from V2V communication failures. The CACC-SOIFT is developed based on the bi-level optimization of the IFT and the controller parameters, as well as the use of a Kalman predictor to trade off idealized string stability, communication failures, and the smoothness of vehicle acceleration. Insights from numerical experiments suggest that CACC-SOIFT can effectively attenuate traffic oscillations and enhance riding comfort.

Section 4 first proposes an idealized MPC-based cooperative control strategy for CAV platooning. Its optimal control decisions can coordinate the behaviors of all following CAVs in the platoon to maneuver them effectively and safely. However, as in existing literature, it is based on the idealized, but unrealistic, assumption that the embedded optimal control problem can be solved instantaneously. To relax this idealized assumption, two deployable strategies, i.e., the DMPC approach and the DMPC-FOA approach, are proposed to address the control delay issue of the idealized MPC strategy and to accurately characterize its optimal control decisions. The DMPC approach addresses the control delay issue by reserving sufficient time before each sampling time instant to solve the embedded optimal control problem. However, the estimated control decisions of the DMPC approach can deviate significantly from those of the idealized MPC strategy due to errors in predicting the leading vehicle's position and speed. By contrast, the DMPC-FOA approach addresses the control delay issue effectively while accurately characterizing the optimal control decisions of the idealized MPC strategy by leveraging the proposed analytical sensitivity analysis method for the embedded optimal control problem. The application of the DMPC-FOA approach for a CAV platoon whose lead vehicle's trajectory is obtained from field data illustrates that it can dampen traffic oscillations efficiently, and can enable smooth deceleration and acceleration behaviors for all following vehicles. In addition, it can provide control decisions very similar to those of the idealized MPC strategy even under extreme situations where the leading vehicle's speed and position are predicted very poorly at each sampling time instant.

It is important to note that the DMPC-FOA approach concept can also be leveraged to address the issue of control delay for other MPC-based cooperative control strategies (e.g., Wang et al., 2014a) arising from the computational time required to solve the embedded optimal control problem. It can be applied for real-time control of large CAV platoons on the condition that the time reserved for computing (i.e.,  $\tau_2$ ) is less than the roll period ( $\Delta t$ ).

It should be noted that while the proposed DMPC-FOA approach can fundamentally address the control delay issue induced by the computational time for the optimal control problem, there is the need to relax some assumptions in this study to make the control approach more robust and reliable to deal with real-world situations.

## 6. RECOMMENDATIONS

This study points out the following future directions:

The future directions of control mechanism related to communication issues are described as follows. In the V2V communications context, our future work includes: (i) considering the role of receiver failure; (ii) factoring retransmission mechanism in modeling process; and (iii) investigating the application of other communication protocols (e.g., 5G). In the context of controller design, this research motivates the following tasks: (i) factoring communication delay, actuator delay, nonlinear vehicle dynamics and external disturbances to design a more realistic controller; (ii) modeling heterogeneous vehicle platoons, and deriving the heterogeneous string stability condition; (iii) analyzing stability of a hybrid dynamic system during the switching process; (iv) analyzing the switching process to guarantee smooth transition between controller sets; and (v) include developing safety-augmented controllers, factoring the heterogeneous string stability and communication delay into controller design, and considering non-stationary random disturbances into the Kalman predictor. Related to the optimization problem, possible future directions include: (i) including more performance matrices or constraints (e.g., comfort, fuel consumption) into the objective function; and (ii) developing a more efficient algorithm to reduce computational time.

The future directions related to computational issues can be summarized as follows. First, the proposed DMPC-FOA approach is a centralized controller for a CAV platoon. It relies on a single vehicle to compute the optimal control decision. The application of the DMPC-FOA approach for real-time control of the CAV platoon can be constrained by the reserved time  $\tau_2$ , which is determined by the computational time of the DMPC-FOA approach. To enable controlling a large-size CAV platoon with a large prediction horizon, discretization technique (see e.g., Wei et al., 2017) and a new solution algorithm (e.g., distributed dynamic programming algorithm) will be developed to reduce the computational time for the optimal control problem. Second, this study does not consider the impacts of uncertainties on system dynamics (e.g., false execution of optimal control, dynamic resistance of the pavement) and initial vehicle conditions (e.g., dynamic communication delay, dynamic sensor measurement errors). However, it is worth mentioning that the MPC approach has some level of robustness against the disturbance of vehicles' state (see Zhou et al., 2017). Further, the analytical sensitivity analysis method for optimal control problem proposed in this study is able to quantify the impacts of changes in both control decisions and initial vehicle conditions on dynamics of the CAV platoon and platoon performance. In future work, robust cooperative control strategies will be developed by leveraging the analytical sensitivity analysis method to enable safe and efficient control of the CAV platoon under different levels of uncertainty. Third, the application of the DMPC-FOA approach depends on two necessary conditions. First, the optimal control decisions are estimated within  $\tau_2$  time. Second, the V2V communications are reliable such that the information can be delivered successfully between the leading vehicle and each of the following vehicles. For the cases that one of the two necessary conditions is not satisfied, the ACC or cooperative sensing-based CACC models should be applied immediately to control the car-following behavior of all CAVs. In future, a switching control which leverages the DMPC-FOA approach and the ACC models (or cooperative sensing-based CACC models) will be developed to control the CAV platoon under different traffic flow and communication environments.

## **7. SYNOPSIS OF PERFORMANCE INDICATORS**

### **7.1 Part I**

The research from this advanced research project was disseminated to 54 people from industry, government, and academia. The research was presented at several conferences, including 23rd International Symposium on Transportation and Traffic Theory, ISTTT 23, 24-26 July 2019 in Lausanne, Switzerland, the Transportation Research Board 2020 Annual Meeting in Washington, DC, and the 2018 INFORMS Annual Meeting in Phoenix, Arizona. This project supported 4 students at the doctoral level. The outputs, outcomes, and impacts are described in the following sections.

### **7.2 Part II**

Research Performance Indicators: 1 conference article and 5 peer-reviewed journal article were produced from this project. At the time of writing, there are no new technologies, procedures/policies, and standards/design practices that were produced by this research project. There was collaboration with other agencies as 1 institution provided matching funds.

The outputs, outcomes, and impacts are described in Section 7 below.

## **8. OUTPUTS, OUTCOMES, AND IMPACTS**

### **8.1 List of research outputs (publications, conference papers, and presentations)**

- Wang, J., Gong, S., Peeta, S., & Lu, L. (2019). A real-time deployable model predictive control-based cooperative platooning approach for connected and autonomous vehicles. *Transportation Research Part B: Methodological*, 128, 271-301.  
<https://www.sciencedirect.com/science/article/pii/S0191261518310427>
- Wang, C., Gong, S., Zhou, A., Li, T., & Peeta, S. (2020). Cooperative adaptive cruise control for connected autonomous vehicles by factoring communication-related constraints. *Transportation Research Part C: Emerging Technologies*, 113, 124-145.  
<https://www.sciencedirect.com/science/article/pii/S0968090X18317133>
- Wang, C., Gong, S., Zhou, A., Li, T., & Peeta, S. (2019). Cooperative adaptive cruise control for connected autonomous vehicles by factoring communication-related constraints. *Transportation Research Procedia*, 38, 242-262.  
<https://www.sciencedirect.com/science/article/pii/S2352146519300237>
- Zhou, A., Gong, S., Wang, C., & Peeta, S. (2020). Smooth-Switching Control-Based Cooperative Adaptive Cruise Control by Considering Dynamic Information Flow Topology. *Transportation Research Record*, 2674(4), 444-458.  
<https://journals.sagepub.com/doi/full/10.1177/0361198120910734>
- Wang, J., Gong, S., Peeta, S., Lu, L. (2020). A real-time deployable model predictive control-based cooperative platooning approach for connected and autonomous vehicles. 99th Annual Meeting of Transportation Research Board (TRB), Washington, D.C, USA.
- Li, Y., Tang, C., Li, K., He, X., Peerta, S., Wang, Y. (2019). Consensus-Based Cooperative Control for Multi-Platoon Under the Connected Vehicles Environment. *IEEE Transactions on Intelligent Transportation Systems*, Vol. 20, Nr. 6, 2220-2229.  
<https://ieeexplore.ieee.org/document/8458142>

## **8.2 Outcomes**

This research project facilitates the understanding and awareness of the implementation of CAV platoon control in the real-world conditions. Specifically, the communication and computation-related issues are explicitly addressed in the research, such that the proposed control strategy can perform and function as expected.

This project also the improvement of CACC technologies and their application in the real world from several perspectives. First, insights from this project can be leveraged in transferring theoretical CACC control strategies into practices where communication-related constraints exist. Second, this project alleviates the computational burden in the implementation of CACC control in real-time, such that the desired platoon control performance can be achieved to improve traffic flow. Further, the study carried out rigorous mathematical modeling of the relevant computational and communication-related problems to illustrate theoretical concepts in the real-world context.

## **8.3 Impacts**

Connected and autonomous vehicles (CAVs) offer users the potential for reduced value of time, enhanced quality of travel experience, and seamless situational awareness and connectivity. This project investigates cooperative platoon control of CAVs by leveraging their capabilities. From the perspective of transportation operation, the research outcomes shed lights on the future development CAV platoon control to benefit the traffic flow when confronting computational and communication-related constraints. From the perspective of human quality-of-life and environment, the platoon control methods proposed in this project help improve traffic efficiency and reduce traffic oscillation. Therefore, broad impacts include reduction of travel time, lowering fuel consumption, and decreasing traffic emissions.

## **8.4 Tech Transfer**

In the execution of the project titled cooperative control mechanism for platoon formation of connected and autonomous vehicles, the research team undertook a number of technology transfer activities. First, the research team published four articles in technical journals with a wide readership, high reputation, and high impact factor. The team also gave two presentations at the TRB annual meeting, a conference with over 14,000 attendees. Further, a number of tech transfer activities were undertaken as part of this project, such as communication with other universities through webinars and forums. The list below summarizes the tech transfer activities undertaken by the research team through the course of this project:

In 2019:

1. Technical paper in Transportation Research Part B: Methodological, 128, 271-301: A real-time deployable model predictive control-based cooperative platooning approach for connected and autonomous vehicles, by Wang, J., Gong, S., Peeta, S., & Lu, L.
2. Technical paper in Transportation Research Procedia, 38, 242-262: Cooperative adaptive cruise control for connected autonomous vehicles by factoring communication-related constraints, by Wang, C., Gong, S., Zhou, A., Li, T., & Peeta, S.
3. Conference presentation at 98th Annual Meeting of the Transportation Research Board, Washington, D.C., USA: Cooperative Adaptive Cruise Control for Connected Autonomous

Vehicles by Factoring Communication-Related Constraints, Wang, C., Gong, S. and Peeta, S. (2019).

In 2020:

1. Technical paper in Transportation Research Record, 2674(4), 444-458, Smooth-Switching Control-Based Cooperative Adaptive Cruise Control by Considering Dynamic Information Flow Topology., by Zhou, A., Gong, S., Wang, C., & Peeta, S.
2. Conference presentation at the 99th Annual Meeting of Transportation Research Board (TRB), Washington, D.C, USA: A Real-time Deployable Model Predictive Control-based Cooperative Platooning Approach for Connected and Autonomous Vehicles, Wang, J., Gong, S., Peeta, S., Lu, L.
3. Technical paper in Transportation Research Part C: Emerging Technologies, 113, 124-145, Cooperative adaptive cruise control for connected autonomous vehicles by factoring communication-related constraints, by Wang, C., Gong, S., Zhou, A., Li, T., & Peeta, S. (2020).
4. Technical paper in IEEE Transactions On Intelligent Transportation Systems, Vol. 20, Nr. 6, Consensus-Based Cooperative Control for Multi-Platoon Under the Connected Vehicles Environment, by Li, Y., Tang, C., Li, K., He, X., Peeta, S., Wang, Y.

In 2021:

1. Presentation at the 2021 Master Forum of Transportation Engineering, Southeastern University, Nanjing, China: Information Flow Topologies and Propagation Modeling for Traffic Management and Control under Connected Vehicle Environments, Peeta, S.

## 9. REFERENCES

- Augustin, D., Maurer, H., 2001. Second order sufficient conditions and sensitivity analysis for the optimal control of a container crane under state constraints. *Optimization*, 49 (4), pp. 351-368.
- Camacho, E. F., Alba, C. B., 2013. *Model predictive control*. Springer Science & Business Media.
- Darbha, S., Rajagopal, K.R., 1999. Intelligent cruise control systems and traffic flow stability. *Transportation Research Part C: Emerging Technologies*, 7(6), pp. 329-352.
- Desjardins, C., Chaib-draa, B. 2011. Cooperative adaptive cruise control: a reinforcement learning approach. *IEEE Transactions on Intelligent Transportation Systems*, 12(4), pp. 1248–1260.
- Dorato, P., 1963. On sensitivity in optimal control systems. *IEEE Transactions on Automatic Control*, 8(3), pp. 256-257.
- Gaimon, C., 2002. *Optimal control theory: Applications to management science and economics*. JSTOR.
- Cheong, S., Safonov, M., 2008. Bumpless transfer for adaptive switching controls. *IFAC Proceedings*. Vol, 41(2), pp. 14415-14420.
- Gao, F., Hu, X., Li, S.E., Li, K., Sun, Q., 2018. Distributed adaptive sliding mode control of vehicular platoon with uncertain interaction topology. *IEEE Transactions on Industrial Electronics*, 65(8), pp. 6352-6361.
- Ge, J. I., Orosz, G., 2014. Dynamics of connected vehicle systems with delayed acceleration feedback. *Transportation Research Part C: Emerging Technologies*, 46, pp. 46-64.
- Gong, S., Du, L., 2018. Cooperative platoon control for a mixed traffic flow including human drive vehicles and connected and autonomous vehicles. *Transportation Research Part B: Methodological*, 116, pp. 25-61.
- Gong, S., Shen, J., Du, L., 2016. Constrained optimization and distributed computation based car following control of a connected and autonomous vehicle platoon. *Transportation Research Part B: Methodological*, 94, pp. 314-334.
- Gong, S., Zhou, A., Peeta, S., 2019. Cooperative adaptive cruise control for a platoon of connected and autonomous vehicles considering dynamic information flow topology. *Transportation Research Record*. <https://doi.org/10.1177/0361198119847473>.
- Guo, G., Yue, W., 2012. Autonomous platoon control allowing range-limited sensors. *IEEE Transactions on Vehicular Technology*, 61(7), pp. 2901-2912.
- Hafeez, K.A., Zhao, L., Ma, B., Mark, J.W., 2013. Performance analysis and enhancement of the DSRC for VANET's safety applications. *IEEE Transactions on Vehicular Technology*, 62(7), pp. 3069-3083.
- Hasebe, K., Nakayama, A., Sugiyama, Y., 2003. Dynamical model of a cooperative driving system for freeway traffic. *Physical Review E*, 68(2). No.026102.
- Hoberock, L., 1977. A survey of longitudinal acceleration comfort studies in ground transportation vehicles. *Journal of Dynamical Systems, Measurement, and Control*, 99(2), pp. 76-84.
- Horowitz, R., and Varaiya, P., 2000. Control design of an automated highway system. *Proceedings of the IEEE*, 88(7), pp. 913-925.
- Jia, D., Lu, K., Wang, J., Zhang, X., Shen, X., 2015. A survey on platoon-based vehicular cyber-physical systems. *IEEE Communications Surveys & Tutorials*, 18(1), pp. 263-284.
- Jia, D., Ngoduy, D., 2016. Platoon based cooperative driving model with consideration of realistic inter-vehicle communication. *Transportation Research Part C: Emerging Technologies*, 68, pp. 245-264.
- Keller, H.B., 1976. *Numerical solution of two point boundary value problems* (Vol. 24). Philadelphia: Society for Industrial and Applied Mathematics.
- Kesting, A., Treiber, M., Schonhof, M., Helbing, D., 2008. Adaptive cruise control design for active congestion avoidance. *Transportation Research Part C: Emerging Technology*, 16(6), pp. 668–683.
- Kim, S., 2012. *Design of the adaptive cruise control systems: an optimal control approach* (Doctoral dissertation, UC Berkeley).
- Kim, Y.H., Peeta, S., He, X., 2017. Modeling the information flow propagation wave under vehicle-to-vehicle communications. *Transportation Research Part C: Emerging Technologies*, 85, pp. 377-395.
- Kirk, D.E., 2012. *Optimal control theory: an introduction*. Courier Corporation, New York, USA.

- Li, S. E., Zheng, Y., Li, K., Wang, J., 2015. An overview of vehicular platoon control under the four-component framework. 2015 IEEE Intelligent Vehicles Symposium (IV), Seoul, South Korea, pp. 286-291.
- Li, X., Peng, F., Ouyang, Y., 2010. Measurement and estimation of traffic oscillation properties. *Transportation Research Part B: Methodological*, 44(1), pp. 1-14.
- Li, X., Wang, X., Ouyang, Y., 2012. Prediction and field validation of traffic oscillation propagation under nonlinear car-following laws. *Transportation Research Part B: Methodological*, 46(3), pp. 409-423.
- Li, Y., Sun, D., Liu, W., Zhang, M., Zhao, M., Liao, X., Tang, L., 2011. Modeling and simulation for microscopic traffic flow based on multiple headway, velocity and acceleration difference. *Nonlinear Dynamics*, 66(1-2), pp. 15-28.
- Lu, G., Nie, Y.M., Liu, X. and Li, D., 2019. Trajectory-based traffic management inside an autonomous vehicle zone. *Transportation Research Part B: Methodological*, 120, pp. 76-98.
- Malanowski, K., 1984. Differential stability of solutions to convex, control constrained optimal control problems. *Applied Mathematics and Optimization*, 12(1), pp. 1-14.
- Malanowski, K., 1987. Stability and sensitivity of solutions to optimal control problems for systems with control appearing linearly. *Applied Mathematics and Optimization*, 16(1), pp. 73-91.
- Malanowski, K., 2011. Sensitivity analysis for state constrained optimal control problems. *Control & Cybernetics*, 40(4), pp. 1043-1058.
- Malanowski, K., Maurer, H., 1996. Sensitivity analysis for parametric control problems with control-state constraints. *Computational Optimization and Applications*, 5(3), pp. 253-283.
- Maurer, H., Pesch, H.J., 1994. Solution differentiability for nonlinear parametric control problems. *SIAM Journal on Control and Optimization*, 32(6), pp. 1542-1554.
- Maurer, H., Pesch, H.J., 1995. Solution differentiability for parametric nonlinear control problems with control-state constraints. *Journal of Optimization Theory and Applications*, 86(2), pp. 285-309.
- Mayne, D. Q., Rawlings, J. B., Rao, C. V., Scokaert, P. O., 2000. Constrained model predictive control: Stability and optimality. *Automatica*, 36(6), pp. 789-814.
- McAuliffe, B., Lammert, M., Lu, X. Y., Shladover, S., Surcel, M. D., Kailas, A., 2018. Influences on energy savings of heavy trucks using cooperative adaptive cruise control. SAE Technical Paper, No. 2018-01-1181.
- Moon, I. K., Yi, K., Caveney, D., Hedrick, J. K., 2005. A multi-target tracking algorithm for application to adaptive cruise control. *Journal of Mechanical Science and Technology*, 19(9), pp. 1742-1752.
- Nakayama, A., Sugiyama, Y., Hasebe, K. 2001. Effect of looking at the car that follows in an optimal velocity model of traffic flow. *Physical Review E*, 2001, 65(1).
- Naus, G.J., Vugts, R.P., Ploeg, J., van de Molengraft, M.J., Steinbuch, M., 2010. String-stable CACC design and experimental validation: A frequency-domain approach. *IEEE Transactions on Vehicular Technology*, 59(9), pp. 4268-4279.
- Nieuwenhuijze, M.R., van Keulen, T., Öncü, S., Bonsen, B., Nijmeijer, H., 2012. Cooperative driving with a heavy-duty truck in mixed traffic: Experimental results. *IEEE Transactions on Intelligent Transportation Systems*, 13(3), pp. 1026-1032.
- Palm, W.J., 2005. *System Dynamics*. McGraw-Hill Higher Education. Columbus, OH.
- Ploeg, J., E. Semsar-Kazerooni, G. Lijster, N. van de Wouw, and H. Nijmeijer., 2015. Graceful degeneration of cooperative adaptive cruise control. *IEEE Transaction on Intelligent Transportation Systems*, 16(1): pp. 488-497.
- Ploeg, J., Shukla, D.P., van de Wouw, N., Nijmeijer, H., 2014. Controller synthesis for string stability of vehicle platoons. *IEEE Transactions on Intelligent Transportation Systems*, 15(2), pp. 854-865.
- Qiu, H. J., Ho, I. W. H., Chi, K. T., 2012. A stochastic traffic modeling approach for 802.11 p VANET broadcasting performance evaluation. 23rd IEEE International Symposium on Personal Indoor and Mobile Radio Communications (PIMRC), Montreal, Canada, pp. 1077-1083.
- Qiu, H. J., Ho, I. W. H., Chi, K. T., Xie, Y., 2015. A methodology for studying 802.11 p VANET broadcasting performance with practical vehicle distribution. *IEEE Transactions on Vehicular Technology*, 64(10), pp.

4756-4769.

- Rajamani, R., Shladover, S.E. 2001. An experimental comparative study of autonomous and co-operative vehicle-follower control systems. *Transportation Research Part C: Emerging Technologies*, 2001, 9(1), pp. 15–31.
- Swaroop, D., Hedrick, J.K., 1996. String stability of interconnected systems. *IEEE Transactions on Automatic Control*, 41(3), pp. 349-357.
- Schakel, W. W. J., Arem, B. V., Netten, B. D., 2010. Effects of cooperative adaptive cruise control on traffic flow stability. 13th International IEEE Conference on Intelligent Transportation Systems (ITSC), Madeira Island, Portugal, pp. 759-764.
- Talebpour, A., Mahmassani, H.S., Bustamante, F.E., 2016. Modeling driver behavior in a connected environment: Integrated microscopic simulation of traffic and mobile wireless telecommunication systems. *Transportation Research Record: Journal of the Transportation Research Board*, (2560), pp.75-86.
- US Department of Transportation, “NGSIM - Next Generation Simulation”, 2007, [Online]. Available: <https://ops.fhwa.dot.gov/trafficanalysistools/ngsim.htm>. [Accessed: Apr. 12, 2018]
- VanderWerf, J., Shladover, S. E., Kourjanskaia, N., Miller, M., Krishnan, H., 2001. Modeling effects of driver control assistance systems on traffic. *Transportation Research Record*, 1748, pp. 167–174.
- Van Arem, B., van Driel, C., Visser, R., 2006. The impact of cooperative adaptive cruise control on traffic-flow characteristics. *IEEE Transactions on Intelligent Transportation Systems*, 7(4), pp. 429-436.
- Wei, Y., Avci, C., Liu, J., Belezamo, B., Aydın, N., Li, P.T. and Zhou, X., 2017. Dynamic programming-based multi-vehicle longitudinal trajectory optimization with simplified car following models. *Transportation research part B: methodological*, 106, pp. 102-129.
- Wang, C., Gong, S., Zhou, A., Li, T., Peeta, S., 2019. Cooperative adaptive cruise control for connected autonomous vehicles by factoring communication-related constraints. *Transportation Research Part C: Emerging Technologies*, <https://doi.org/10.1016/j.trc.2019.04.010>.
- Wang, J., Kim, Y. H., He, X., Peeta, S., 2018a. Analytical model for information flow propagation wave under an information relay control strategy in a congested vehicle-to-vehicle communication environment. *Transportation Research Part C: Emerging Technologies*, 94, pp. 1-18.
- Wang, J., Kim, Y. H., He, X., Peeta, S., 2017. Analytical model for information flow propagation wave under an information relay control strategy in a congested vehicle-to-vehicle communication environment. *Transportation Research Part C: Emerging Technologies*, 23, pp. 738-757.
- Wang, M., Daamen, W., Hoogendoorn, S. P., Arem, B. V., 2014a. Rolling horizon control framework for driver assistance systems. Part II: Cooperative sensing and cooperative control. *Transportation Research Part C: Emerging Technologies*, 40, pp. 290-311.
- Wang, M., Daamen, W., Hoogendoorn, S.P., van Arem, B., 2014b. Rolling horizon control framework for driver assistance systems. Part I: Mathematical formulation and non-cooperative systems. *Transportation Research Part C: Emerging Technologies*, 40, pp. 271-289.
- Wang, M., Daamen, W., Hoogendoorn, S.P., van Arem, B., 2016. Cooperative car-following control: Distributed algorithm and impact on moving jam features. *IEEE Transactions on Intelligent Transportation Systems*, 17(5), pp. 1459-1471.
- Wang, M., Hoogendoorn, S.P., Daamen, W., van Arem, B., Shyrokau, B., Happee, R., 2018b. Delay-compensating strategy to enhance string stability of adaptive cruise controlled vehicles. *Transportmetrica B: Transport Dynamics*, 6(3), pp. 211-229.
- Wang, Y., Li, X., Yao, H. 2019. Review of trajectory optimisation for connected automated vehicles. *IET Intelligent Transport Systems*, 13(4), pp. 580-586.
- Xiao, L., Wang, M., Schakel, W., van Arem, B., 2018. Unravelling effects of cooperative adaptive cruise control deactivation on traffic flow characteristics at merging bottlenecks. *Transportation Research Part C: Emerging Technologies*, 96, pp. 380-397.
- Zheng, Y., Li, S.E., Li, K., Borrelli, F., Hedrick, J.K., 2017. Distributed model predictive control for heterogeneous vehicle platoons under unidirectional topologies. *IEEE Transactions on Control Systems*

Technology, 25(3), pp. 899-910.

- Zheng, Y., Li, S.E., Li, K., and Ren. W., 2018. Platooning with connected vehicles with undirected topologies: robustness analysis and distributed h-infinity controller synthesis. *IEEE Transaction Intelligent Transportation System*, 19(3), pp.1353-1364.
- Zheng, Y., Li, S.E., Wang, J., Cao, D., Li, K. 2016. Stability and scalability of homogeneous vehicular platoon: study on the influence of information flow topologies. *IEEE Transactions on Intelligent Transportation Systems*, 17(1), pp. 14–26.
- Zhou, Y., Ahn, S., Chitturi, M., Noyce, D.A., 2017. Rolling horizon stochastic optimal control strategy for ACC and CACC under uncertainty. *Transportation Research Part C: Emerging Technologies*, 83, pp. 61-76.

## APPENDIX 1

### Cooperative Control Mechanism for Platoon Formation of Connected and Autonomous Vehicles

#### Published Related Work

- Wang, J., Gong, S., Peeta, S., & Lu, L. (2019). A real-time deployable model predictive control-based cooperative platooning approach for connected and autonomous vehicles. *Transportation Research Part B: Methodological*, 128, 271-301.

#### Abstract

Recently, model predictive control (MPC)-based platooning strategies have been developed for connected and autonomous vehicles (CAVs) to enhance traffic performance by enabling cooperation among vehicles in the platoon. However, they are not deployable in practice as they require the embedded optimal control problem to be solved instantaneously, with platoon size and prediction horizon duration compounding the intractability. Ignoring the computational requirements leads to control delays that can deteriorate platoon performance and cause collisions between vehicles. To address this critical gap, this study first proposes an idealized MPC-based cooperative control strategy for CAV platooning based on the strong assumption that the problem can be solved instantaneously. It also proposes a solution algorithm for the embedded optimal control problem to maximize platoon performance. It then develops two approaches to deploy the idealized strategy, labeled the deployable MPC (DMPC) and the DMPC with first-order approximation (DMPC-FOA). The DMPC approach reserves certain amount of time before each sampling time instant to estimate the optimal control decisions. Thereby, the estimated optimal control decisions can be executed by all the following vehicles at each sampling time instant to control their behavior. However, under the DMPC approach, the estimated optimal control decisions may deviate significantly from those of the idealized MPC strategy due to prediction error of the leading vehicle's state at the sampling time instant. The DMPC-FOA approach can significantly improve the estimation performance of the DMPC approach by capturing the impacts of the prediction error of the leading vehicle's state on the optimal control decisions. An analytical method is derived for the sensitivity analysis of the optimal control decisions. Further, stability analysis is performed for the idealized MPC strategy, and a sufficient condition is derived to ensure its asymptotic stability under certain conditions. Numerical experiments illustrate that the control decisions estimated by the DMPC-FOA approach are very close to those of the idealized MPC strategy under different traffic flow scenarios. Hence, DMPC-FOA can address the issue of control delay of the idealized MPC strategy effectively and can efficiently coordinate car-following behaviors of all CAVs in the platoon to dampen traffic oscillations. Thereby, it can be applied for real-time cooperative control of a CAV platoon.

- Wang, C., Gong, S., Zhou, A., Li, T., & Peeta, S. (2020). Cooperative adaptive cruise control for connected autonomous vehicles by factoring communication-related constraints. *Transportation Research Part C: Emerging Technologies*, 113, 124-145.

#### Abstract

Compared to existing human-driven vehicles (HDVs), connected and autonomous vehicles (CAVs) offer users the potential for reduced value of time, enhanced quality of travel experience, and seamless situational awareness and connectivity. Hence, CAV users can differ in their route choice behavior compared to HDV users, leading to mixed traffic flows that can significantly deviate from the single-class HDV traffic pattern. However, due to the lack of quantitative models, there is limited knowledge on the evolution of mixed traffic flows in a traffic network. To partly bridge this gap, this study proposes a multiclass traffic assignment model, where HDV users and CAV users follow different route choice principles, characterized by the cross-nested logit (CNL) model and user equilibrium (UE) model, respectively. The CNL model captures HDV users' uncertainty associated with limited knowledge of traffic conditions while overcoming the route overlap issue of logit-based stochastic user equilibrium. The UE model characterizes the CAV's capability for acquiring accurate information on traffic conditions. In addition, the multiclass model can capture the characteristics of mixed traffic flow such as the difference in value of time between HDVs and CAVs and the asymmetry in their driving interactions, thereby enhancing behavioral realism in the modeling. The study develops a new solution algorithm labeled RSRS-MSRA, in which a route-swapping based strategy is embedded with a self-regulated step size choice technique, to solve the proposed model efficiently. Sensitivity analysis of the proposed model is performed to gain insights into the effects of perturbations on the mixed traffic equilibrium, which facilitates the estimation of equilibrium traffic flow and identification of critical elements under expected or unexpected events. The study results can assist transportation decision-makers to design effective planning and operational strategies to leverage the advantages of CAVs and manage traffic congestion under mixed traffic flows.

- Wang, C., Gong, S., Zhou, A., Li, T., & Peeta, S. (2019). Cooperative adaptive cruise control for connected autonomous vehicles by factoring communication-related constraints. *Transportation Research Procedia*, 38, 242-262.

#### Abstract

Compared to existing human-driven vehicles (HDVs), connected and autonomous vehicles (CAVs) offer users the potential for reduced value of time, enhanced quality of travel experience, and seamless situational awareness and connectivity. Hence, CAV users can differ in their route choice behavior compared to HDV users, leading to mixed traffic flows that can significantly deviate from the single-class HDV traffic pattern. However, due to the lack of quantitative models, there is limited knowledge on the evolution of mixed traffic flows in a traffic network. To partly bridge this gap, this study proposes a multiclass traffic assignment model, where HDV users and CAV users follow different route choice principles, characterized by the cross-nested logit (CNL) model and user equilibrium (UE) model,

respectively. The CNL model captures HDV users' uncertainty associated with limited knowledge of traffic conditions while overcoming the route overlap issue of logit-based stochastic user equilibrium. The UE model characterizes the CAV's capability for acquiring accurate information on traffic conditions. In addition, the multiclass model can capture the characteristics of mixed traffic flow such as the difference in value of time between HDVs and CAVs and the asymmetry in their driving interactions, thereby enhancing behavioral realism in the modeling. The study develops a new solution algorithm labeled RSRS-MSRA, in which a route-swapping based strategy is embedded with a self-regulated step size choice technique, to solve the proposed model efficiently. Sensitivity analysis of the proposed model is performed to gain insights into the effects of perturbations on the mixed traffic equilibrium, which facilitates the estimation of equilibrium traffic flow and identification of critical elements under expected or unexpected events. The study results can assist transportation decision-makers to design effective planning and operational strategies to leverage the advantages of CAVs and manage traffic congestion under mixed traffic flows.

- Zhou, A., Gong, S., Wang, C., & Peeta, S. (2020). Smooth-Switching Control-Based Cooperative Adaptive Cruise Control by Considering Dynamic Information Flow Topology. *Transportation Research Record*, 2674(4), 444-458.

#### Abstract

Vehicle-to-vehicle communications can be unreliable because of interference and information congestion, which leads to the dynamic information flow topology (IFT) in a platoon of connected and autonomous vehicles. Some existing studies adaptively switch the controller of cooperative adaptive cruise control (CACC) to optimize string stability when IFT varies. However, the difference of transient response between controllers can induce uncomfortable jerks at switching instances, significantly affecting riding comfort and jeopardizing vehicle powertrain. To improve riding comfort while maintaining string stability, the authors introduce a smooth-switching control-based CACC scheme with IFT optimization (CACC-SOIFT) by implementing a bi-layer optimization model and a Kalman predictor. The first optimization layer balances the probability of communication failure and control performance optimally, generating a robust IFT to reduce controller switching. The second optimization layer adjusts the controller parameters to minimize tracking error and the undesired jerk. Further, a Kalman predictor is applied to predict vehicle acceleration if communication failures occur. It is also used to estimate the states of preceding vehicles to suppress the measurement noise and the acceleration disturbance. The effectiveness of the proposed CACC-SOIFT is validated through numerical experiments based on NGSIM field data. Results indicate that the CACC-SOIFT framework can guarantee string stability and riding comfort in the environment of dynamic IFT.

- Li, Y., Tang, C., Li, K., He, X., Peeta, S., Wang, Y. (2019). Consensus-Based Cooperative Control for Multi-Platoon Under the Connected Vehicles Environment. *IEEE Transactions on Intelligent Transportation Systems*, Vol. 20, Nr. 6, 2220-2229.

#### Abstract

This paper investigates formation control protocols for autonomous vehicular strings with vehicle-to-vehicle (V2V) communication connections. To this end, a four-layer framework is first proposed to illustrate the cooperative mechanism within and across strings. Then, cooperative control protocols are designed based on vehicle role, i.e., leader or follower, in vehicular multi-string. In particular, longitudinal controllers are designed for single string and multiple strings by incorporating inter-vehicle gap and velocity difference of the follower vehicle with respect to the preceding vehicle and the lead vehicle. In addition, lateral controllers are proposed for single string and multiple strings based on the artificial function method. The proposed protocols ensure that follower vehicles asymptotically track the leader within each string, while different vehicular strings can form a desired platoon pattern. The study further analyzes the stability and consensus of the proposed control protocols using the Routh–Hurwitz stable criterion and the Lyapunov technique. Numerical experiments are performed for two cooperative mechanisms—parallel and serial. Results from numerical experiments illustrate the effects of the proposed control protocols on road throughput and demonstrate their effectiveness for position and velocity consensuses.